2020

DESIGN, BUILD, AND ANALYSIS OF A COMPRESSED NATURAL GAS DIRECT INJECTION COMPRESSION IGNITION SINGLE CYLINDER RESEARCH ENGINE

Tyler Miller
Michigan Technological University, tylermil@mtu.edu

DESIGN, BUILD, AND ANALYSIS OF A COMPRESSED NATURAL GAS DIRECT INJECTION COMPRESSION IGNITION SINGLE CYLINDER RESEARCH ENGINE

By

Tyler J. Miller

A THESIS

Submitted in partial fulfillment of the requirements for the degree of

MASTER OF SCIENCE

In Mechanical Engineering

MICHIGAN TECHNOLOGICAL UNIVERSITY

2020

This thesis has been approved in partial fulfillment of the requirements for the Degree of MASTER OF SCIENCE in Mechanical Engineering.

Department of Mechanical Engineering-Engineering Mechanics

Thesis Co-Advisor:	*Dr. Jeffrey D. Naber*
Thesis Co-Advisor:	*Dr. Jeremy Worm*
Committee Member:	*Dr. Darrell Robinette*
Department Chair:	*Dr. William W. Predebon*

Table of Contents

List of figures

List of tables

Acknowledgements

This work was supported by The Alliance for Sustainable Energy, LLC, Management and Operating Contractor for the National Renewable Energy Laboratory (NREL), Subcontract No. NHQ-9-82305-06, a sub unit of the U.S. Department of Energy under Award No. DE-AC36-08GO28308. I would also like to thank Michigan Technological University for the last seven years of knowledge and growth as a student and a professional. I would like to thank the Advanced Power System Research Center staff for their assistance on the project. I would finally like to thank my friends and family for all their support throughout my time as a graduate student pushing me to pursue my passion of mechanical engineering.

List of abbreviations

ASTM	American Society for Testing and Materials
ATDC	After Top Dead Center
BMEP	Brake Mean Effective Pressure
BTDC	Before Top Dead Center
BTE	Brake Thermal Efficiency
CFD	Computational Fluid Dynamics
CI	Compression Ignition
CNG	Compressed Natural Gas
CO_2	Carbon Dioxide
CR	Compression Ratio
CVCC	Constant Volume Combustion Chamber
DI	Direct Injection
DOE	Design of Experiments
EATS	Engine Aftertreatment System
EMOP	Exhaust Max Open Position
EOC	End of Compression
EVC	Exhaust Valve Close
EVO	Exhaust Valve Open
FCA	Fuel Control Actuator
GVWR	Gross Vehicle Weight Ratings
HPDI	High Pressure Direct Injection
IAH	Intake Air Heater
IAT	Intake Air Temperature
IMOP	Intake Max Open Position
IVC	Intake Valve Close
IVO	Intake Valve Open
LNG	Liquified Natural Gas
LHV	Lower Heating Value
MAP	Manifold Absolute Pressure
MDPV	Medium-Duty Passenger Vehicles
NG	Natural Gas
NO_X	Oxides of Nitrogen
PFI	Port Fuel Injection
PM	Particulate Matter
RCM	Rapid Compression Machine
SCRE	Single Cylinder Research Engine
SI	Spark Ignited
SOI	Start of Injection
SPC	Slightly Premixed Combustion
TDC	Top Dead Center
TTL	Transistor-Transistor Logic
VVA	Variable Valve Actuation

Abstract

Both experimental and simulation efforts have been employed to further advance the design and build of a single cylinder research engine. The engine will aid in advancing technology and understanding the operation of compression-ignition (CI) engines using natural gas within the heavy-duty engine industry. The basis for the engine is a Cummins 15L ISX engine that has been modified, retrofitted, and instrumented to allow for late-cycle direct-injection of high-pressure compressed natural gas. Along with the engine build, a one-dimensional GT-Power simulation model has been created and used to analyze the engine operation and specify components including the engine compression ratio and charging system. The combustion model was calibrated to a kinetic combustion model at multiple speed load points in effort to understand the effect of compression ratio, temperature, and start of injection, on natural gas compression ignition.

1 Introduction

Chapter one outlines of the goals and objectives of the single cylinder research engine (SCRE) using late-cycle direct injection (DI) of compressed natural gas (CNG) to achieve compression ignition (CI) funded by the United States Department of Energy. The research completed is funded by the DOE in efforts to achieve Diesel like efficiency with a late cycle DI CI CNG engine. The objective of the DI CI of CNG engine is to provide a simplified fuel system for the engine with diesel like efficiencies. With a simplified fuel system and improved engine efficiencies compared to other NG engine technologies, the proposed CI DI monofuel engine could achieve the objective of a 1-year payback for high annual mileage class-8 trucks at high production volumes. Chapter one outlines the tasks completed within the thesis including the simulations conducted, the experimental build of the SCRE, and the results obtained within year one of the project. All the tasks completed are aimed at the major objective of demonstrating diesel like performance in both emissions and efficiency using a DI CI CNG SCRE. To better understand why the project is being conducted, first a background of the benefits of the fuel, and combustion system must be understood. The ability to achieve natural gas auto-ignition must also be reviewed and discussed to understand the entirety of the work completed for the achievement of the goals set for the SCRE build.

1.1 Background

1.1.1 Benefits of Natural Gas

The use of natural gas (NG) engines as a source of fuel has many benefits. The first benefit of NG fuel is the high content (>80%) of methane, the shortest hydrocarbon fuel (CH_4) The benefit of using a fuel made of majority methane is because methane has the lowest CO_2/MJ compared to any other hydrocarbon fuel. The second benefit of NG fueled engines is the low cost of the fuel. According to the United States Department of Energy Alternative Fuels Data Center, since the year 2000, CNG retail prices have been predominantly lower than both diesel and gasoline [1]. A third major benefit of burning CNG is the decrease in NOx (oxides of nitrogen) that are emitted from an engine.

Compared to Diesel USLD with a NOx output of 250 mg/km for road transport, CNG has been shown to only emit 50 mg/km [2]. These are three main contributors influencing the use of CNG as an alternative fuel within engines.

1.1.2 Natural Gas Combustion Systems

NG has been explored in many different combustion systems to date including stoichiometric SI engines where the incoming fuel is pre-mixed with the air prior to entering the combustion chamber and a spark plug is used for the ignition of the fuel air mixture. The benefits to using a pre-mixed SI are the simplicity of the fuel system where either a carburetor or port fuel injectors (PFI) can be located within the intake stream to control the load to the engine. Another engine system developed using natural gas is dual fuel engines where a homogeneous natural gas and air mixture is ignited when a small quantity of DI diesel fuel enters the cylinder. Nieman et al. investigated various methods of improving combustion efficiency in lean burn dual-fuel CNG/Diesel engines in a 2010 13L engine showing crevice losses of naturally fumigated CNG can be reduced by reducing the overall crevice volume [3]. Some negatives of CNG diesel pilot engines discussed by Nieman include the combustion losses from flame front quenching, crevice packing from diesel swirl motion and much larger crevice volumes and losses for diesel type pistons compared to SI CNG engines [3]. Other types of dual fuel engines are enabled by directly injecting both diesel and CNG. DI^2 co-direct injection engines consisting of dual fuel operation with both fuels have been explored as well.

Neely et al. studied the benefits of partially pre-mixed natural gas spray angle being ignited by a pilot of diesel fuel would ignite a previously direct-injected natural gas using a 3D-CFD model [4]. The benefits included an increase from 46.8 to 47.5% efficiency when modifying the nozzle angle at 1000RPM 12 bar BMEP [4]. Another benefit of the study showed DI^2 showed up to 50% decrease in combustion losses compared to a fumigated fully pre-mixed NG dual fuel engine [4].

Dual fuel engines have also been developed using high-pressure direct injection (HPDI) initially patented in 2008 by Westport Power Inc [5]. The system consists of two fuels

entering the combustion chamber through a common injector. One combustion scheme used in HPDI is the called late post injection (LPI) where diesel pilot is injected first, and natural gas as 10-25% of the fuel mass is injected the pilot injector has finished which showed promising results in decreasing particulate matter (PM) emissions [6]. The second regime exhibited by Westport surround the HPDI setup is slightly premixed combustion (SPC) where the diesel pilot is retarded slightly allowing for more mixing of the CNG prior to combustion [7]. SPC showed promising results at high load although it had negative implications on combustion stability and increasing pressure rise rates [7]. The current HPDI 2.0 injector has entered production in China with the joint venture of Weichai [8] There have also been pilot fueled CNG engines where the pilot fuel is injected entirely after the main source of CNG is injected during the compression stroke.

A few other strategies suggested and studied include pre-chamber designs. The pre-chamber designs can consist of a pre-chamber where the air-natural gas is filled into the pre-chamber and ignited with either a spark plug or a diesel pilot injection. The benefits of the pre-chamber spark ignited combustion modes include stable ignition, high efficiency, low NO_X emissions, while there are challenges in the system including bowl design, and pre-chamber design [9]. In comparison, the pre-chamber design that incorporates the diesel pilot instead of the spark plug typically requires longer service intervals. All the systems discussed so far include either a secondary fuel, or a spark plug to initiate the ignition of the NG. The main reason for using either diesel or a spark plug as a source of ignition for typical NG fueled engines is i.e. (spark, diesel pilot) is due to CNG's low cetane number, requiring higher temperatures to achieve auto-ignition as a mono-fuel.

While it is more difficult to ignite NG, exhibiting a Motoring Octane Number of around 122 according Genchi and Pipitone, it is possible to auto-ignite [10]. Naber et al. presented experimental studies revolved around NG auto-ignition varying NG type and density within a constant volume combustion chamber (CVCC) [11]. The studies performed by Naber et al. showed promising ignition delay (ID) values. Experimental

results show at an ambient density of 20.4 kg/m^3 mean NG required a bulk gas temperature of 1120K to achieve an ID of 2 ms [11].

The benefits of running a mono fueled DI CI CNG SCRE include the use of a single fuel system. Unlike dual fuel engines, a mono fuel engine only requires one fuel tank and fuel control system on a vehicle simplifying design and packaging. Another benefit of using CNG DI CI SCRE is running on a diesel like cycle where the intake air is not throttled, and minimal pumping losses are experienced. Diesel like engine performance is possible while providing higher efficiency as well as lower CO_2 emissions. The SCRE DI CI NG engine also provides the opportunity for ultra-low NOx output with a simplified engine aftertreatment system (EATS). A final added benefit of the SCRE DI CI NG system is the ability to run without knock limitations which are present in both NG SI engines, and dual-fuel pilot engines where NG enters the combustion chamber through the intake port as a homogenous mixture.

To achieve a mono-fuel natural gas auto-ignition combustion system within an internal combustion engine, multiple changes are required. The changes are revolved around increasing the end-of-compression (EOC) temperatures, modifying the fuel system to accept DI of CNG, enabling variable valve actuation (VVA) to allow for various effective compression ratios (CR), and possibly increasing the cetane value using cetane improvers for CNG.

1.2 Goals and Objectives

The goals this research is to setup a SCRE with the ability to run on a mono fueled CNG to achieve stable consistent CI combustion using a prototype DI high pressure NG fuel system. The SCRE engine size is aimed at medium-duty (MD) and heavy-duty (HD) applications for both on road and stationary power. The performance objective of the SCRE is to prove the ability to run the mono fuel engine at a high engine load of 24 bar brake mean effective pressure (BMEP) while maintaining the 0.016 g/bhp-hr NO_x tail pipe out emissions with the use of a selective catalytic reduction aftertreatment system while also reducing the CO_2 emissions. To test a mono-fueled NG CI DI SCRE many

tasks must be completed prior to running the engine. The goals of this research including the initial analysis of the engine, procurement of engine parts, and the SCRE build.

The thesis work can be separated into two portions, modeling and simulation, and engine setup and experimentation.

The first objective for the modeling and simulation includes developing a 1D GT-power model to assist in the design of engine components including the piston compression ratio and an intake air heater. The second objective of the 1D model was to assist in designing the intake and exhaust system for the SCRE. The third objective of the modeling and simulation was to calibrate the 1D model to prior data including 3D CFD combustion models provided by Westport Fuel Systems. The final objective of the 1D modeling included a CAM timing sweep to determine the benefits of increased valve overlap or negative valve overlap to increase temperatures at intake valve close (IVC).

1. Modeling and Simulation Tasks
    a. Determine Required Intake Conditions for SCRE CNG
    b. Boost Pressure and Mass Flow Analysis of SCRE
    c. Simulate Charging System to Assist in Intake/Exhaust Surge Tank Sizing
    d. Calibrate Three Pressure Analysis (TPA) Model
    e. Calibrate DI-Pulse Ignition Model
    f. Design of Experiments (DOE) Sweeping CR, Start of Injection (SOI), Intake Air Temperature (IAT) with calibrated DI-Pulse Model
    g. Cam Timing Sweep of SCRE Cam to determine effective CR range and potential benefits of valve overlap

The engine experimentation main objective was to develop and design an operational SCRE with Westport's modified injector to operate using DI CI CNG. There are many tasks required to achieve the objective of a functional DI CI CNG SCRE shown below.

1. Engine Setup and Experimentation Tasks
    a. Procure a 15L ISX engine 2.5L/cylinder

b. Design and Fabricate Engine Cart
c. Design and Fabricate Isolators and Mounts
d. Install SCRE on Cart
e. Fabricate Engine Interface Panel
f. Determine Proper Driveshaft and Flywheel
g. Design and Fabricate Intake and Exhaust Gas Recirculation (EGR) system
h. Design and Fabricate Exhaust System
i. Implement Stand-alone Engine ECU
j. Determine Compression Ratio Plan
k. Determine Intake Air Heater Plan
l. Machine Cylinder Head
m. Design and Manufacture System for Cylinder Deactivation
n. Cam Timing Development Plan
o. Install Sensors and Actuators
p. Design Boosted CNG Fuel System
q. Install Fuel System on Engine Cart
r. Research Cetane Boosters
s. Research Piston and Head Thermal Barrier Coatings
t. SCRE Shake-down

1.3 Thesis Outline

This section gives an introduction and background to the motivation behind the compressed natural gas (CNG) direct injection (DI) compression ignition (CI) single-cylinder research engine (SCRE) project. The background gives the insight into the benefits of NG fueled engines, current CNG engine combustion systems, the potential of DI CI, and the goals and objectives of the research to date. The research intention is to prove the ability to run a stable CNG DI CI SCRE with diesel like engine performance and assess the efficiency and emissions benefits. This is a three-year project funded by the United States Department of Energy (DOE). The project entails two teams working jointly on extensive experimental and simulation research to achieve CI of late cycle DI

NG. The teams working together on the project include members from Westport Fuel Systems Inc. and members of Michigan Technological University Advanced Power Systems Research Center.

Chapter 2 includes a literature review further exploring studies revolved around compression ignition engines, diesel fuels, NG fuel properties, auto-ignition, injector technology, and emissions benefits. This section will provide a thorough understanding of what has been completed previously relevant to the DI CI SCRE research.

Chapter 3 focuses on the zero-dimensional and one-dimensional modeling and simulation of the SCRE. The chapter will break down the tasks described in section 1.2 from the initial required intake conditions all the way to the cam timing sweep of the SCRE.

Chapter 4 includes the engine setup and experimentation portion of the research. It should be noted that the research objective for the first year of the project is to prove operation of the SCRE on mono fuel CNG, but this task has not yet been completed under this portion of the research.

Chapter 5 is a summary of the project goals, objectives, and lessons learned throughout the research project. This will include future work and paths forward on tasks not fully completed for both chapters 3 and 4.

Chapter 6 gives the references used within the paper throughout the thesis work, and chapter 7 includes the appendices of additional information referenced.

2 Literature Review

2.1 Introduction

This literature review will cover previous work completed on the combustion of natural gas (NG) within internal combustion engines. The use of alternative fuels has been a major topic for many years. Due to the abundance of NG, the industry has pushed towards exploring this as an alternative fuel within internal combustion engines. There are two typical types of engines currently including SI, and CI. The focus of this review will be on previous studies using NG within CI engines. The initial background covered will include compression ignition overview, diesel fuel overview, natural gas properties. Finally, the discussion of natural gas autoignition, injector technology, and natural gas engine benefits will be reviewed.

2.2 Compression Ignition Engine Overview

The CI engine has been in continuous development and improvement since the 1890's when Rudolf Diesel created the first "slow-burning" engine. The first engine that was developed and tested proved to be 26.2% efficient which was very significant compared to the modern steam engines at the time over 250 percent more efficient relatively [12]. Since the invention of the first CI engine, there has been many improvements which have pushed commercially available compression ignition HD brake thermal efficiency (BTE) to approximately 43 to 46% [13]. The work completed by Mohr et al. on the Super Truck 2 initiative proved that HD diesel engines could reach BTE of 49.9% on class 8 trucks [14]. The improvements of CI engines come from a variety of different improvements including manufacturing tolerances, turbocharger improvements, reduced friction, electronic fuel delivery and control, and many others.

The diesel engines commercially available today are typically 4-stroke engines having intake, compression, expansion, and exhaust piston strokes. CI engines combust the fuel not with a spark plug source, but with high temperature and pressure due to the high CR of the engine and the characteristics of the fuel otherwise known as cetane rating. CI

engines typically have a fuel injector located centrally within the combustion chamber. The fuel is injected when the piston is near top dead center (TDC) of the compression stroke. According to Heywood, the stages of combustion for DI CI diesel engines can be broken down into four parts, ID, premixed or rapid combustion, mixing-controlled combustion, and late combustion [15]. ID is defined as the time delay between the start of the fuel injection into the combustion chamber and the start of combustion from an apparent heat-release measured curve [15]. Premixed combustion is the phase where fuel air mixture within a flammability limit burns rapidly resulting in high heat-release rates [15]. Mixing controlled combustion occurs when the initial pre-mixed air-fuel has been consumed and the burn rate is controlled by the rate at which fuel air mixture becomes available governed by atomization, vaporization, mixing of fuel vapor with air, and pre-flame chemical reactions [15]. Late combustion occurs when a small fraction of the fuel had not been consumed or some of the fuel rich combustion soot products still contains enough energy to be burned [15]. The auto-ignition and combustion process in a diesel engine occurs where the fuel and air mixture are near a stoichiometric condition [15]. Although the combustion process is taking place at near stoichiometric conditions, the combustion process in its entirety is on the lean side of stoichiometric (more air than fuel).

2.3 Compression Ignition Fuels Overview

One important thing to consider regarding CI engines, is the fuel used. Most DI CI engines today use diesel fuel. The standard diesel fuel is a petroleum-based product that goes through specific refining process required for it to auto-ignite within a CI engine appropriately. As an entire population, our fuel consumption could possibly pose a threat to society as it is assumed there is only a limited amount of crude oil within the earth. Other fuels such as biodiesel, rapeseed methyl ester, Di-Methyl-Ether, and CNG/Diesel dual fuel options have been explored for compression ignition engines [16].

Diesel fuels are specified by a rating called cetane along with other American Society for Testing and Materials (ASTM) standards. The cetane rating according to the NREL

compendium of experimental cetane values gives a measure of the ignition delay from the time a fuel is injected to the time the combustion occurs [17].

A fuel with a high cetane number will have a short ID and will be more susceptible to ignition, while a lower cetane number will be more difficult to ignite and has a longer ID. Typical diesel fuels have a cetane number between 42-55 [18]. Diesel fuel is the fuel of choice for compression ignition engines because it is much easier to ignite in comparison to a fuel such as gasoline. The cetane number is determined through the test procedure ASTM Method D613 where two reference fuels are used to determine the autoignition of the tested fuel within a single cylinder variable compression ratio engine [20]. The cetane number is comparable in some respects to the octane rating of a spark ignited fuel. A high-octane fuel "hard to ignite" will have a low cetane value. So, in perspective, a low octane fuel would perform better within a DI CI engine. Figure 2.1 shows a comparison of the cetane vs. octane rating [21].

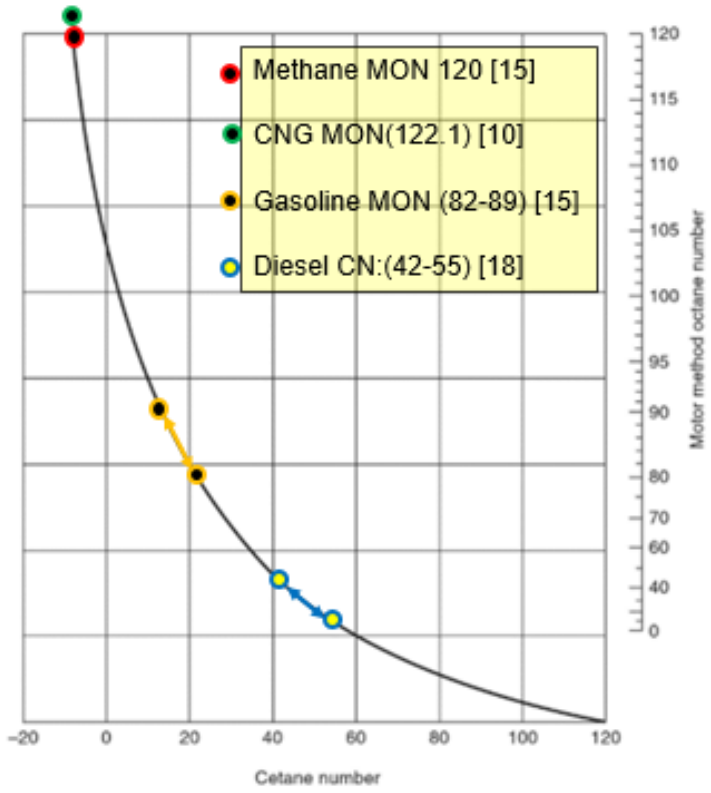

Figure 2.1: Cetane vs. Octane Correlation Obtained from Taylor [21]

Another property that is important to consider within a fuel is the lower heating value (LHV). The LHV gives the amount of energy available within a specified mass of fuel typically given in units of MJ/kg. According to Heywood, LHV of light diesel fuel is 43.2 MJ/kg, while NG is listed at 45 MJ/kg [15]. LHV must also be considered on a stoichiometric basis for true comparison, the stoichiometric mixture of light diesel and NG are both 14.5 giving LHV of stoichiometric mixtures of diesel and NG 2.79 and 2.9 respectively meaning the NG has more energy per mass as well on a stoichiometric basis [15]. The important thing to note from Table 2.1 is NG's low energy specific carbon (CO_2) emissions. With both diesel and gasoline being approximately 19 and 17.3 g (CO_2)/MJ more respectively, NG provides lower carbon dioxide emissions when achieving the same BTE.

Table 2.1: Energy Specific Carbon Emissions, Lower Heating Value, and Air to Fuel Ratio of Fuels

Fuel	Energy Specific Carbon Emissions [22]	Lower Heating Value [15]	Stoichiometric Air to Fuel Ratio [15]
Type	g (CO2)/MJ	(MJ/kg)	A/F
Diesel fuel	69.3	43.2	14.5
Gasoline (without ethanol)	67.6	44	14.6
Propane	59.8	46.4	15.67
Natural gas	50.3	45	14.5

2.4 Natural Gas Fuel Property Overview

Natural gas as a fuel within DI CI engines has been explored, but usually within a dual fuel engine application where NG is the main combustion product, but diesel fuel is used as the source of ignition. NG can come in many forms, but there are some typical ranges for NG readily available within the U.S. Liss et al., showed methane ranged from 75-98%, ethane 0.5-13%, and propane ranged from 0-2.6% [23]. Other forms of NG include liquified natural gas (LNG), which has a very high methane concentration as high 99.6% [23]. There are many extremes of NG as well, including "peak shaving" gas according to Liss which contains a high propane concentration [24]. The many different types of NG

were experimentally studied and modeled by Naber et al. to determine their autoignition properties [11]. The paper shows a table which shows the fuels tested within their experiment including methane, mean, high ethane, and peak shaving. One of the differences that is different between the NG fuels LHV which ranges from a high of 50 MJ/kg in pure methane to a low of 42 in the High Ethane NG fuel [11]. The higher LHV shows more energy per unit mass of fuel which means less fuel would be needed to produce the same amount of energy if the stoichiometry of the mixtures is similar.

The autoignition of natural gas is not trivial especially compared to diesel combustion. According to Naber et al., the autoignition of natural gas occurs in a temperature range from 1100-1200 K, but to produce a desired 2.0 ms pressure delay at an ambient density of 20.4 kg/m^3, 1100-1130K bulk gas temperature is required dependent upon the NG type [11]. The study by Naber et al. of the 4 different fuels produced ID between 0.5-0.7 ms which is reasonable according to the conclusions [11]. Typical diesel ID ranges from 0.3 to 10 ms based upon temperature according to Heywood [15]. According to Oliver et al., 2 ms is an upper threshold for current diesel ID [25]. The 2 ms ID of NG has been experimentally proven by Naber et al. using temperatures around 1100K. The experimental combustion vessel results paired closely with the Multi-dimensional modeling of Natural Gas combustion by Agarwal et al. [26]. The temperature regions for autoignition of the 3 different blends studied by Agarwal et al. ranged from 1150 K to 1300K. The detailed chemical kinetic model coupled with a multidimensional flow model by Agarwal et al. also showed that an additional 5% by volume of hydrogen peroxide added to the methane reduced the ID from 0.99 ms to 0.67 ms at 1250K [26]. Again, to revisit the ID obstacle posed by NG, NG has a low cetane number because it is primarily made up of methane. Methane has a high-octane number of 120 which correlates to a cetane number of around negative 5 which is very low compared to typical diesel fuels ranging from 42-55. From Figure 2.1, Table 2.2 has been generated with the data from experimental measurements as well as the correlated MON or CN value depicted by the asterisk. This shows the MON of Methane being 120 with a correlated CN of -5. The MON of CNG is 122.1 which correlates to a CN of approximately -10. The standards for

diesel fuel within the U.S. include either a minimum cetane index of 40 or an Aromaticity maximum of 35% by volume [27]. While the national standard has a minimum value of 40, the California Air Resources Board (CARB) in 2014 increased their minimum natural CN to 48 [28].

Table 2.2: MON and CN Correlation

Fuel Type	MON	CN
Methane	120	-5*
NG	122.1	-10*
Gasoline	82-89	10-22*
Diesel	5-50*	42-55

Looking further into the NG autoignition, Fraser et al. states that the range for a 2 ms autoignition to occur requires temperatures from 1250-1200K on a range of 0 to 10.6% ethane by volume added to pure methane [29]. Through the isentropic compression calculations, Fraser et al. states that compression ratios required for a Naturally Aspirated (NA) engine to reach temperatures of 1200K to 1250K would have to be between 26-29:1 [29]. Two important parameters noted by Fraser et al. is that the combustion vessel fails to generate the turbulence typically generated in an internal combustion engine, and the combustion vessel has a decreasing temperature when the NG is injected which is opposite of a typical internal combustion engine [29]. While the NG diesel is typically injected before or very close to TDC, often ignition does not occur until after TDC where volume is increasing. The study within the combustion vessel helps understand the properties within the chamber to have diesel like combustion where autoignition can occur but fails to emphasize the flow characteristics generated by a typical engine. Throughout the papers reviewed, it is possible for NG autoignition to occur, but the temperatures must be considerably higher than temperatures in a typical diesel engine.

Further studies by Araki et al show combustion of CNG with not a high compression ratio engine or a CVCC, but experiments completed with a rapid compression machine (RCM) [30]. The compression ratio used within the RCM was only 10 which is under half of what would be needed to combust NG according to Naber et al [11]. The combustion model used by Araki et al included a glow plug to assist in the ignition process, which was set to 1280 K [30]. Two fuels were used within their experimental CNG 12A which was mostly 99.1% methane, and CNG 13A which came from Japan city supplied gas a more readily available mixture consisting of 86.3% methane and 5.19% ethane. Throughout their studies they state that the CNG 12A autoignition takes place after the end of fuel injection when the injector has closed, but for CNG 13A, ignition sometimes occurred early in the injection period hence a shorter ID agreeing with the simulations by Fraser et al. [30]. In conclusion, Araki et al. stated that 12A fuel had a much longer ID classified as late ignition, while 13A sometimes had "early ignition" with a short ID, and continued combustion during fuel injection like a typical diesel engine [30]. The use of a glow plug is much different than the increased compression ratio by Naber et al. and Fraser et al., but is a viable option for ignition assist [11]. McTaggart-Cowan et al. showed that hot surface ignition (HSI) could be used to create a stable gas pilot flame with ignition delays around 1-2 ms with experimental CVCC data and CFD simulation [31]. Other forms of assistance with the ignition process includes fuel additives to increase cetane values for decreased ID.

A study by Goto et al. explored the development of a liquified petroleum gas LPG engine DI diesel engine with a CR of 17:1, better known as a propane engine [32]. The study explored the use of cetane enhancers for the compression ignition engine using additives like Di-t-butyl peroxide (DTBP), and 2-Ethylhexyl nitrate (2EHN) [32]. Although this is a different base fuel compared to CNG, the concept of adding fuel additives is still prevalent when discussing autoignition of CNG in a diesel like engine with autoignition. LPG, like CNG, also has an extremely low cetane number correlated from its octane value according to Goto et al, the autoignition of LPG alone is determined to be very difficult and almost impossible [32]. The use of DTBP at 5 wt.%, and 2EHN at 3.5 wt.%

allowed the engine to combust using autoignition within the 4-cycle diesel engine [32]. One of the main findings in the study was that the thermal efficiency of the LPG developed engine was near that of diesel engine when DTBP was greater than 5 wt.% [32]. The study done by Goto showed the use of a very low cetane fuel "LPG" is possible with cetane enhancers. It is possible that cetane enhancers such as DTBP, hydrogen peroxide, or 2EHN, should also be looked at for the use in a CNG DI CI engine.

2.5 Natural Gas Injector Technologies

Looking into the injection of a gaseous fuel, it is much different than that of a typical liquid diesel fuel. Diesel fuel injectors are typically very short duration with injection around TDC based upon the ID due to the temperature and pressure at the end of compression [25]. If ignition delay is too short combustion rates may increase resulting in extremely high levels of knock. At times diesel injection strategies are retarded substantially to reduce NO_x. The experimental setup by Oliver et al. used a Bosch CRP2 injector which did not require a fluid which allowed for the use of high-pressure gaseous CNG fuel [25]. The CNG fuel was increased in pressure from 69 to 414 bar to deliver the amount of fuel required in the short period of time for a boosted engine application. To provide constant flow and pressure a damping volume and heat exchanger were put in place after the 69 to 414 bar compressor and prior to the injector [25]. The fuel injectors used within the study were driven by high pressured air, and the fuel was able to inject at a pressure of 690 bar and higher. Oliver et al. states that the possibility of using Westport HPDI injectors would be a great alternative to the CRP2 retrofitted diesel injectors [25].

HPDI injectors have been used for the injection of natural gas within a diesel engine and are typically used in heavy duty applications [33]. The HPDI injectors have been in production for several years since 2008, but the HPDI 2.0 improves upon the original design [33]. The injectors are suitable for LNG and CNG fuels [33]. According to Mumford et al, the HPDI is proven to withstand variations in NG fuel quality as well as allowing for proper load control [34]. The HPDI 2.0 is said to improve upon the first generation by decreasing the size and venting the gas during operation as well as during

shutdown of the engine [34]. The venting of LNG has been a problem for injectors, and it is stated that it is more efficient to use direct injection of LNG with an LNG pump and HPDI rather than keeping a compressor on board a vehicle for the compression of CNG to high pressures [34]. The HPDI 2.0 is said to also improve upon the first generation by using higher pressures and multiple injection strategies within one combustion event within the engine cycle [34]. Continuous improvement of the 2.0 injectors has been ongoing according to Westport, as well as the use of NG as an alternative fuel for diesel compression ignition engines [34].

The improvements and ability to use NG within an engine has been made possible by multiple parties including the Westport's HPDI and HPDI 2.0, and modified Bosch diesel injectors by Oliver et al. at Stanford University. The use of NG within compression ignition engines seems to become more feasible as injector technology advances. The advances in technology including higher pressure systems for the injections near TDC with NG ignition temperatures needed (1200K), as well as venting access fuel are major contributors to enable NG as a fuel for compression ignition engines.

With diesel emissions getting more stringent specifically in respect to NOx, and PM, there is a push for cleaner engine out emissions. The use of NG as a fuel for CI engines will burn cleaner than diesel [26]. According to Chala et al., NG can reduce carbon emissions (CO_2) by 20-30% in comparison to typical fuels used including gasoline and diesel [35]. Looking further into CI engines operating with NG, Landi et al reported with 60% of diesel replaced with NG, PM was reduced by 40% [36]. The benefit of using NG in a dual fuel operation shows obvious benefit in PM emission reduction compared to diesel.

A comparison of NG and diesel busses by Nylund et al. showed much lower PM emissions (g/km) under the Braunschweig and Orange County cycles tested when comparing a SI NG engine to a diesel-powered bus [37]. Although the NG engine was SI compared to the diesel, it performed better on the PM emissions [37]. The NOx output comparison on these cycles showed a much lower concentration of NOx on the

Braunschwig cycle for the NG compared to diesel for MY 2002-2004 vehicles [37]. The NOx outputs were decreased from 7.7 g/km to 2 g/km by switching a lean burn NG with an oxidation catalyst [37]. Although NG CI will prove to have higher temperatures compared to SI NG engines the study by Nylund showed a decrease when switching to a lean burn CNG SI engine compared to a stoichiometric burn. One thing to consider is that the NG vehicles would also perform better if they were to be running on a diesel cycle rather than a spark ignited Otto cycle. The overall brake thermal efficiency (BTE) of diesel CI engines is currently higher than SI engines due to ability to run higher compression ratios as well as lower pumping losses. So, if NG is used and combusted within a CI cycle the efficiencies would also increase compared to the SI NG engines currently ran today.

In conclusion, on the use of NG as an alternative fuel, it is obvious the emissions can meet and exceed diesel emissions. Alternative fuels such as NG have been explored for many years. The use of NG in internal combustion engines specifically in CI has become more readily available due to technological advancements including injector technologies. Although the autoignition of NG is not trivial due to the high temperature requirements in cylinder at EOC, it is possible. Studies of the autoignition determining that temperatures around 1100-1200K are required to ensure combustion is feasible. The conversion of diesel CI engines to using NG has required many modifications to the engine including injector technology, injection strategies, and intake modifications. Multiple studies have compared NG SI to diesel CI on the same cycle, and it is shown that NG engines can provide lower GHG emissions. Using NG as a mono-fuel within a CI application will only increase the benefits further. As SI engines prove to have lower BTE compared to CI due to pumping losses and lower CR, the mono-fuel NG CI engine will surpass SI NG engines in efficiency and emissions standards. The emission output of NG engines has been shown to burn cleaner, but at a possible cost of fuel efficiency when using a SI engine conversion according to multiple studies. When comparing the best in class efficiency and power output to the expected CIDI operation, the CIDI NG engine is

expected to meet exceed both diesel and SI NG engines while maintaining the same power shown in Table 2.3 [38].

Table 2.3: Efficiency and Power Comparison [38].

Metric	Unit	Diesel BL (2018)	SI NG (2018)	RCCI [38]	CI DI NG	CIDI vs SI NG
Displacement	L	12-15	12	13	12-15	N/A
BMEP	bar	24	20	12	24	+20%
Brake Eff	%	46	37	42	48	+30%

Theoretically, if NG is to be used within a CI engine with typical higher BTE, the CI NG will outperform SI NG engines in efficiency and CI diesel engine emissions, specifically CO_2 emissions. The continuous improvement of NG engines will hopefully provide an optimal route for this fuel to be integrated into CI engines in the future.

3 Modeling and Simulation

This chapter presents the modeling and simulation completed throughout the initial build of the DI CI CNG SCRE. The specifications for the SCRE base OEM engine configuration are below in Table 3.1. Table 3.2 gives the parameters of the SCRE configuration. The engine consists of six in-line cylinders, one of which will be firing for the SCRE. The displacement is 2.5L/cylinder, with a stock CR of 17:1. The SCRE will have a range of CR dependent on selected piston geometry and head gasket thickness. The typical fuel for the engine is diesel which is driven by a mechanical over-head camshaft. The SCRE fuel system will be a HPDI Westport injector for CNG fuel only. The two intake, and two exhaust valves within the valvetrain are also gear driven by an over-head camshaft. The base engine is equipped with cooled EGR which has been removed to keep as much exhaust heat within the external EGR system. The base engine is also equipped with a variable geometry turbocharger which has also been removed from the engine. The boost pressure will be controlled with a regulated compressed air supply, so the turbo was not required.

Table 3.1: OEM Base Engine Configuration

Cylinders	6
Displacement (L)/Cylinder	2.5
OEM Compression Ratio	17:01
OEM Fuel	Diesel
Fuel Injection System	Overhead Camshaft DI
Valves	4
Valvetrain	Overhead Camshaft
EGR	Cooled
Boost System	Variable Geometry Turbocharger
Power Output (hp)	385-600

Table 3.2: SCRE Parameters

Cylinders Firing	1
Displacement (L)/Cylinder	2.5
SCRE Compression Ratio	17:1-27:1
Fuel	CNG
Fuel Injection System	HPDI CNG
Valves	4
Valvetrain	Overhead Camshaft
EGR	Non-Cooled
Boost System	Regulated Building Compressed Air
Power Output BMEP (bar)	24

The specific SCRE GT-Power model parameters are given in Table 3.3. The parameters include the displacement, bore, stroke of the engine which are not changed compared to the OEM spec. The initial model CR of 17 was used as a starting point. The connecting rod length is 261.5 mm. Other parameters included are the model cam profile data including intake valve max opening point (IMOP), intake valve open timing (IVO), intake valve close timing (IVC), exhaust valve max opening point (EMOP), exhaust valve open timing (EVO), and exhaust valve close timing (EVC) all in CAD with respect to TDC before (BTDC), or after (ATDC).

Table 3.3: SCRE GT-Power Model Parameters

Displacement	2.5 L
Bore	137 mm
Stroke	169 mm
Connecting Rod Length	261.5 mm
CR	17-27:1
IMOP	437° ATDC (firing)
IVO	347° ATDC (firing)
IVC	151° BTDC (firing)
EMOP	235° ATDC (firing)
EVO	131° ATDC (firing)
EVC	396° ATDC (firing)

The modeling for this project was used as a design aid in many aspects including the ability to understand the influence of intake and exhaust surge tank sizes, understanding the mass flow and heating requirements of the air charge, as well as determining the engine intake heating and compression-ratio regimes for reaching CNG auto-ignition temperatures (1100-1200K). There were multiple models developed. The first model developed was a 0-D model using Engineering Equation Solver (EES) software. This model was used as an initial aid to understand required intake air temperatures, pressures, and CR's to meet the required EOC temperatures. The second model developed was a one-dimensional model using Gamma Technologies GT-power software. The GT model was used to calibrate a predictive combustion model. The prediction combustion model was calibrated to as three-dimensional CFD combustion model provided by our supporting project partner Westport Fuel Systems Inc.

3.1 Required Intake Conditions for SCRE DI CI CNG

As mentioned consistently throughout the literature review, temperature at EOC is a major driving factor in the auto-ignition of CNG. To understand the required IAT to achieve a specific EOC temperature an isentropic compression process can be used to calculate. The EOC temperature is varied based upon the IAT, CR, and gamma the ratio of specific heats. Equation 3.1 gives the isentropic compression effect of pressure on temperature, where the EOC temperature is related to the intake air temperature

multiplied by the pressure ratio to the exponential one minus one over gamma. State 1 (P1) occurs at bottom dead center (BDC) of the engine stroke prior to compression. State 2 (P2) occurs at TDC of the compression stroke. Equation 3.2 relates the EOC pressure to the manifold absolute pressure (MAP) multiplied by the CR to the power of gamma. Equation 3.2 gives the relation of EOC pressure to the volume ratio or CR of the engine. Equation 3.3 shows the effect of specific heat ratio, specific heat at constant pressure over specific heat at constant volume on gamma used in both equations 3.1 and 3.2. For the simple 0D analysis initially used, Engineering Equation Solver (EES) software was used for initial calculations. The code used for initial 0D thermodynamic analysis of the 2.5L/cylinder engine can be found in appendix A1.

$$EOC_{Temp.} = IAT \times \left(\frac{P2}{P1}\right)^{\left(1-\frac{1}{\gamma}\right)} \quad 3.1$$

$$EOC_{Pres.} = MAP \times CR^{\gamma} \quad 3.2$$

$$\gamma = \frac{Cp}{Cv} \quad 3.3$$

To better understand the effect of CR, and IAT on EOC temperature, a sweep was completed using EES varying the CR from 17 to 27 in 5 even increments. EOC temperature was varied from 1100K to 1300K and the IAT was solved for using EES. For the DI CI SCRE, the specific heats of air within the cylinder were calculated based on a 350K increase from the IAT an approximate midpoint in the compression stroke. The gammas calculated using equation 3.1 averaged at 1.363 with one standard deviation of 0.004 showing consistent values for each all cases. Figure 3.1 shows the constant (ISO) EOC temperatures ranging from 1100K to 1300K for various IAT and CR's. The plot shows the required IAT at the various CR's to achieve EOC temperatures for the auto-ignition of NG. The important note from Figure 3.1 is that as CR is increased the required IAT decreases. The two stars on the plot show the required IAT to reach EOC temperatures of 1150K. For a CR of 19.5 an IAT of 117°C is required while if the CR is increased to 24.5 the IAT is only 81.5°C. The increasing of CR and IAT can both be

levers in adjusting the EOC temperature. As a baseline number, 1100K is a minimum EOC temperature ensure reasonable auto-ignition with delays approximately around of CNG (REF Needed). Figure 3.1 helps define the required IAT at any CR, allowing the user in defining the amount of heater power required when designing the IAT system.

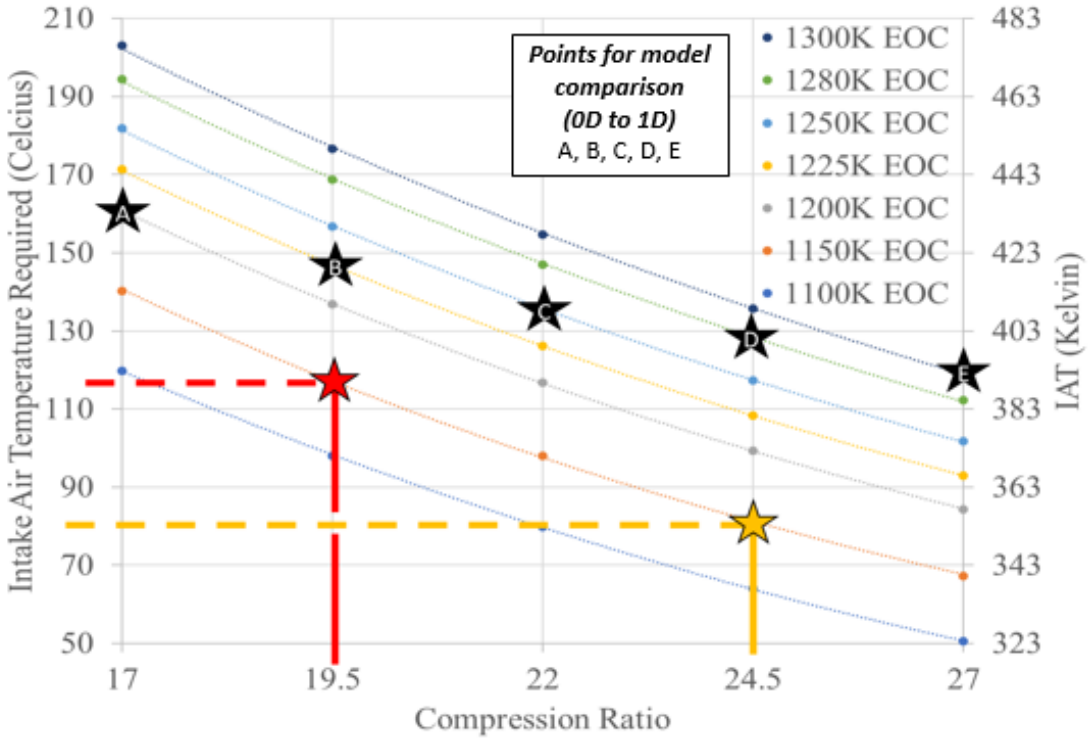

Figure 3.1: ISO EOC Temperature (IAT vs. Compression Ratio EES)

After modeling the engine using the simplified 0D thermodynamic analysis with EES as given above, a 1-D GT-Power Three-Pressure Analysis (TPA) 17:1 CR model was calibrated to a 17:1 CR CFD model provided by Westport. The 3D CFD modeling results provided by Westport consisted of pressure and apparent heat release rates of combustion data estimated from the chemical kinetics within their model. After the initial 17:1 CR model was calibrated, a sweep of CR, and IAT was completed using GT-Power. Figure 3.2 shows the same constant temperature plot as shown in Figure 3.1 with CR swept from 17-27:1 and IAT swept from 350K to 465K. The observed temperatures compared to the 0D calculations show very similar responses as expected. Five stars were placed on both the 0D and 1D ISO EOC temperature plots at various IAT and CR values. The values

from both the 0D calculations and 1D simulations are found in table 3.1 along with the respective error between the models. The 1D is expected to be slightly higher due to hot residual burned gasses being trapped during valve overlap. Overall, the difference in EOC temperatures for multiple CR and IAT is minimal between the 0D and 1D model reassuring the 1D model accuracy in assessing EOC temperatures at various IAT's and CR's.

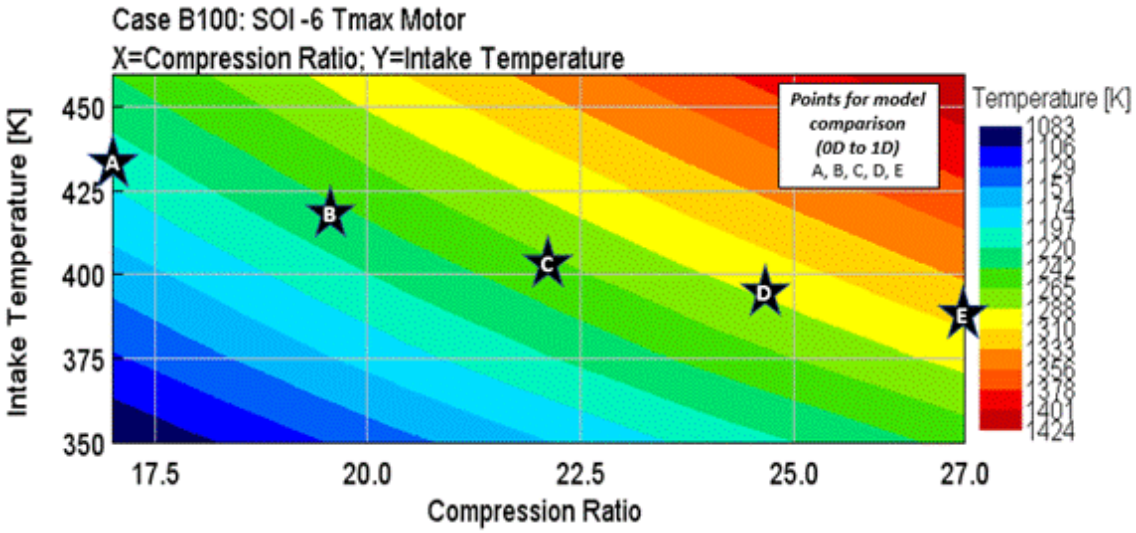

Figure 3.2: ISO EOC Temperature (IAT vs. CR GT-Power)

Table 3.4: 0D and 1D EOC ISO Comparison

Point	IAT (C°/K)	0D Model EOC Temp (EES) (K)	1D Model EOC Temp (GT-Power) (K)	Error (%)
A	161/434	1200	1209	0.7
B	147/420	1225	1231	0.5
C	136/409	1250	1254	0.3
D	128/401	1280	1290	0.8
E	119/392	1300	1310	0.8

The initial 0D analysis was performed to accomplish Task 1.a. under the modeling and simulation. Determining the required intake conditions for the SCRE including IAT required for achieving CI of CNG at various CR's. The model was used as a baseline to understand the thermodynamic equations involved with reaching EOC temperatures of

1100K. The 0D analysis was then compared to the first 1D GT-model created for reassurance that correlation between the thermodynamic 0D and the 1D model aligned. Task 1.a is a portion of the first objective within modeling and simulation aiding in the design of several components of for the SCRE including the intake heater and piston CR. To design the SCRE piston and heater, first the heating and CR requirements had to be understood on a thermodynamic level.

3.2 Boost Pressure and Mass Flow Analysis of SCRE

To size the boosted compressor system, the 0D thermodynamic analysis was completed on a range of CR and Target EOC pressures. A range of EOC were selected from 100 to 160 bar. The CR was then swept holding the EOC pressure constant and solving for the required MAP to reach the desired EOC pressures. The EOC TDC temperatures were also held constant at 1100K for each of the calculations. Figure 3.3 shows the required MAP at various CR to reach the desired EOC pressures. Like Figure 3.1, as the CR is increased, the required MAP decreases. The decrease in required MAP indicates a lower pressure is required to maintain the same EOC pressure. For example, at 24.5:1 CR, to reach 120 bar at EOC, only 150 kPa is required while 19.5:1 CR requires 210 kPa. As CR is increased the change in required MAP for each EOC pressure increase becomes less.

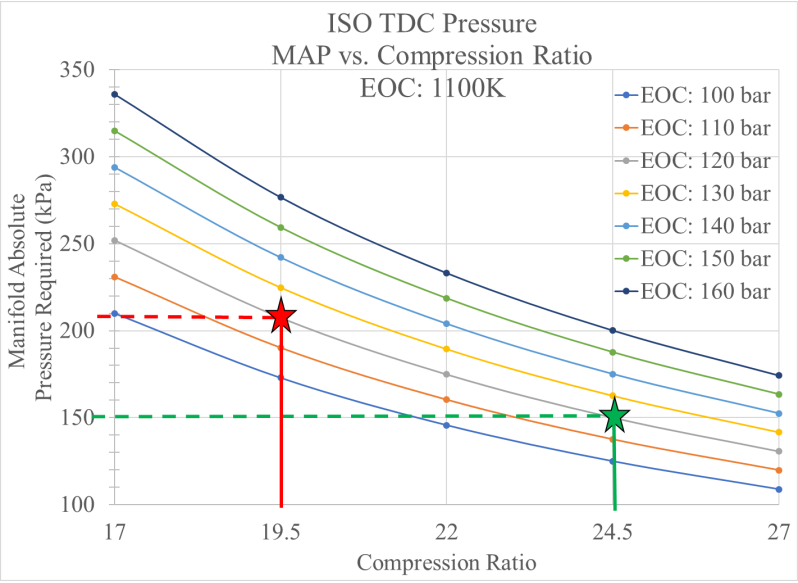

Figure 3.3: ISO EOC Pressure (MAP vs. CR)

The purpose of Figure 3.3 is to provide a basis of understanding at various geometric CR values what EOC pressures resulting. According to Kumar et al., with the OEM stock CR of 17.3 for a later version of the ISX, boost pressures range from approximately 3 bar at full load mode A100 down to approximately 1.25 bar for load case B25 [39]. So, based upon equation 3.2, at a MAP value of 4 bar absolute at a 17.3:1 CR with the specified gamma of 1.363 EOC pressure would be 195 bar which is not shown on the constant compression lines. This plot shows that as the CR increases the overall trend of MAP decreases to reach the same pressures at EOC. This figure aids in the understanding of the boost pressures required within the facility at various CR's to maintain and achieve results like the boost pressures and EOC pressures like the OEM turbocharger on the ISX engine. This study was required to achieve task 1.b the initial study of the required boost system within the facility to operate the SCRE. As mentioned in section 3, the turbocharger was removed, so understanding boost pressures and their resulting EOC pressures for each CR was required.

3.3 Simulate Charging System to Assist in Intake/Exhaust Surge Tank Sizing

The charge system on the SCRE GT-Power model was of key concern during the design process. Due to the planned deactivation of five of the six cylinders when converting the 15L I6 Cummins ISX to a 2.5L SCRE, the mass flow rate was expected to fluctuate significantly. When all six cylinders are pumping air, mass flow through the intake and exhaust manifolds are expected to remain more constant with smaller fluctuations during each intake/exhaust stroke. With only one-cylinder pumping air, the flow becomes less constant increasing the fluctuations in the intake and exhaust manifolds. A simulation study using GT-Power was completed to examine the sizing of the intake and exhaust surge tank sizes of the engine.

The purpose of the surge tank study was to determine the effect on trapped residuals, pressure fluctuations between the intake and exhaust for EGR, the effect on the overall mass flow within the intake stream of the engine, and the effects on the pumping loop.

The initial model that was setup did not include an EGR loop, only an intake and exhaust surge tank. Figure 3.4 shows the initial model of the SCRE engine including the location of the surge tanks and where important parameters were examined.

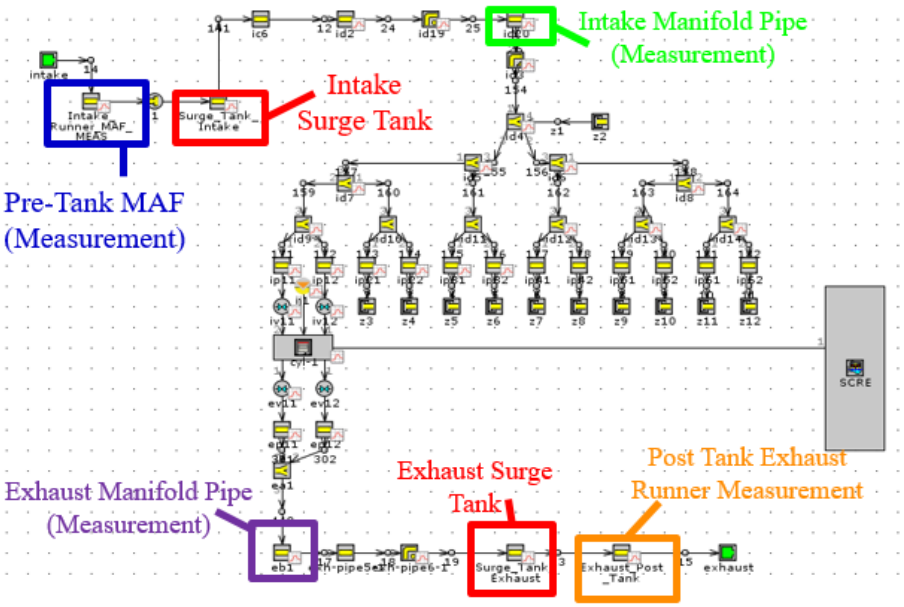

Figure 3.4: Initial 1D GT-Power Model

The model was simulated over several cases sweeping the surge tanks from 24 liters up to 212 liters based on tank dimensions that were readily available [40]. First (cases 1-4), the intake surge tank was swept while holding the exhaust tank to a four-inch pipe diameter. Secondly (cases 5-8), the exhaust tank was swept holding the intake tank to a four-inch pipe diameter, followed by a sweep of both surge tanks at the same time (cases 9-12). Finally, a baseline model was explored with no surge tank (case 13). Table 3.5 gives the dimensions of the parameters used for the initial surge tank sweep including intake and exhaust pressures.

Table 3.5: SCRE Surge Tank Model Sweep Parameters
MAP: 2.5bar Exhaust Pressure: 3.0bar absolute

Case #	Intake Surge Tank Volume (L)	Intake Surge Tank Diameter (in)	Intake Surge Tank Length (in)	Exhaust Surge Tank Volume (L)	Exhaust Surge Tank Diameter (in)	Exhaust Surge Tank Length (in)
01	024	14	10	002	4	10
02	045	14	18	002	4	10
03	125	22	20	002	4	10
04	212	22	34	002	4	10
05	002	4	10	024	14	10
06	002	4	10	045	14	18
07	002	4	10	125	22	20
08	002	4	10	212	22	34
09	024	14	10	024	14	10
10	045	14	18	045	14	18
11	125	22	20	125	22	20
12	212	22	34	212	22	34
13	002	4	10	002	4	10

Figure 3.5 shows as the intake surge tank was increased, an increase in burned residuals is realized. The first interesting result from the surge tank sweep was with respect to the trapped burned residuals. For the intake surge tank size increase while the exhaust was held constant, an increase in residuals was observed. While the burned residuals only increase 0.2% the trend should still be noted. When the exhaust surge tank size was increased, we see a decreasing trend of trapped burned residuals from 24L up to 125L. and then a slight increase in residuals when increasing the tank size from 125L up to 212L. During the exhaust and both surge tank sweeps, a similar trend is noticed with minimal change from 24L to 45L, but a drop when increasing from 45L to 125L. The no tank case showed 2.6% burned residual fraction. The first important finding from Figure 3.5 is that when a surge tank is added to the exhaust side of the engine either with or without an intake surge tank, there is a decrease in burned residuals. This is most likely due to the amount of volume within the exhaust portion held at a higher pressure than the intake. When the exhaust surge tank is removed from the system, and an intake surge tank of any size above a stock pipe is held at boost pressure the residuals increase indicating and the back flow into the intake port increases with intake surge tank size.

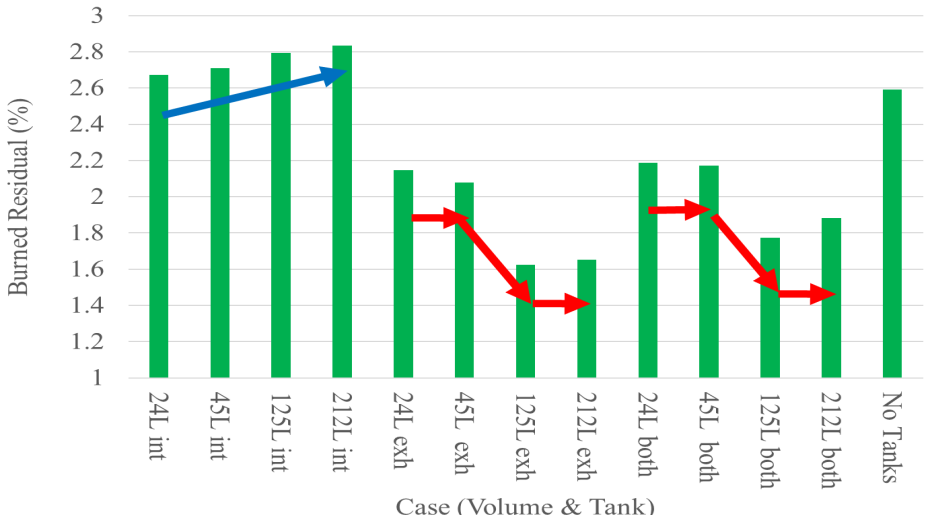

Figure 3.5: Trapped Residuals vs. Surge Tank Sweep

Figure 3.6 shows the total trapped mass against each of the cases tested. One interesting result is that the total trapped mass trend between the intake and both tank sweeps is similar. This trend shows that the intake surge tank has more of an effect than the exhaust on the total trapped mass within the cylinder. The trapped mass peaked at 45L for both the intake, and both tanks when swept. The more mass trapped within the engine indicates a higher VE which increases the overall efficiency. The exhaust surge tank sweep showed a slightly upward trend when increasing the surge tank size. With respect to trapped mass, the best surge tank choice would include a 45L intake surge tank.

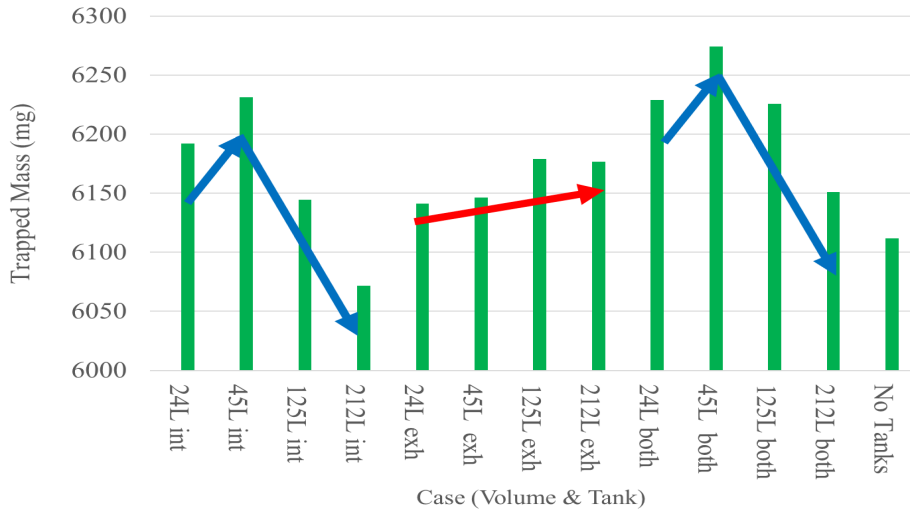

Figure 3.6: Total Trapped Mass vs. Surge Tank Sweep

Figure 3.7 gives the delta pressure throughout the engine cycle that was obtained by taking the difference between the intake and exhaust surge tank given by equation 3.4. The first takeaway from Figure 3.7 includes the large pressure drop at EVO for no exhaust surge tank. All cases that did not include a surge tank in the exhaust with 3 bar of back pressure show a rapid pressure drop near 1 bar at EVO. The second takeaway from Figure 3.7 is the effect of increasing both surge tanks simultaneously and their effect on the EGR loop. As both surge tanks are increased, the delta pressure flattens with the minimum change in delta pressure across the EGR loop coming from a 212L intake and exhaust surge tank. The last takeaway is the increasing of the exhaust surge tank volume results in a lower pressure delta in the EGR loop during the compression and expansion stroke. The optimum EGR loop would consist of a minimum delta pressure throughout between the two surge tanks throughout the engine cycle. With regards to the delta pressure metric, the 212L intake and exhaust surge tank option would be chosen.

$$P_{intake} - P_{Exhaust} = \Delta Pressure\ (EGR) \tag{3.4}$$

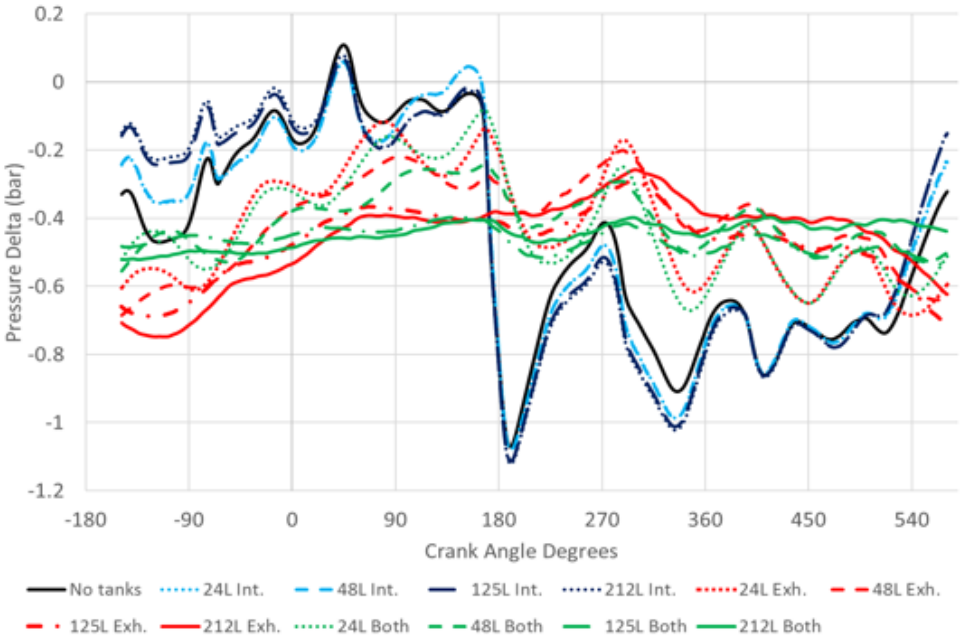

Figure 3.7: $\Delta Pressure\ (EGR)$ vs. Crank Angle (Surge Tank Sweep)

Figure 3.8 shows mass flow rate upstream of the intake surge tank. At 24L approximately 10 times the displacement of the cylinder volume, a 0.05 kg/s change from peak to peak is observed whereas the 212L surge tank shows negligible change in mass flow rate throughout the engine cycle. The surge tank volume acts as a damper for the air flow upstream of the tank. As the intake surge tank increases in size, the mass flow rate has a lower fluctuation throughout the engine cycle, and the ability to measure mass flow rate becomes easier. There is minimal difference between the 48L and 125L surge tank regarding mass flow measurement upstream of the surge tank.

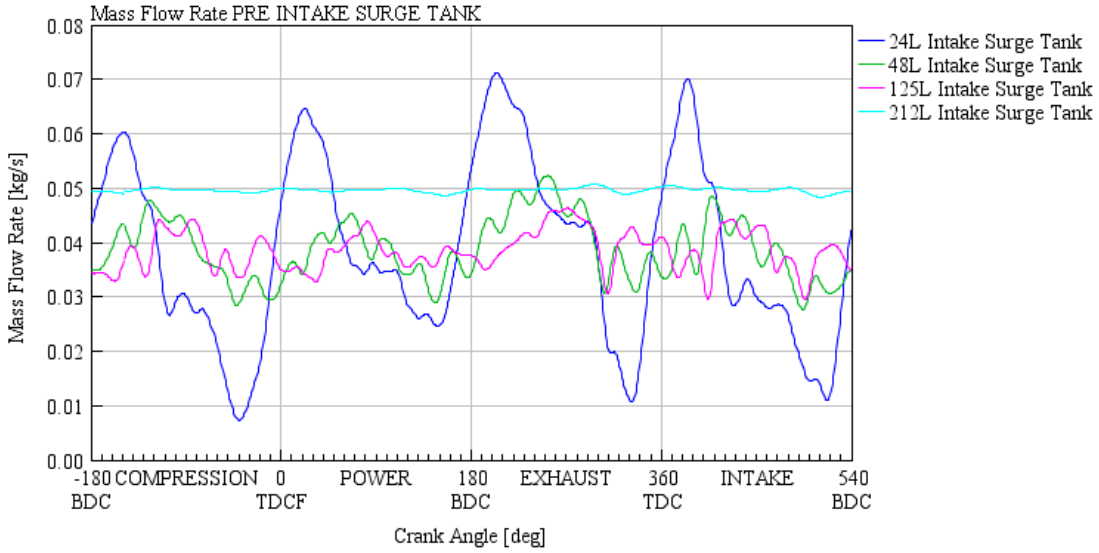

Figure 3.8: Pre-Surge Tank Mass Flow Rate

With respect to measuring engine mass flow, the lower fluctuations throughout the engine cycle, the easier the mass flow is to measure from any sensor as the samples per second requirement decreases. As Figure 3.8 shows, there is a large mass flow rate fluctuation measured upstream using the 24L tank and it decreases substantially when doubled to a 48L surge tank. The optimal tank size for measuring mass flow would be the 212L intake surge tank.

Each metric was measured for a specific reason. The trapped residuals per case was measured to understand the effect of the sizing on residuals with respect to baseline. There is not necessarily a best-case scenario with regards to trapped residuals with for

surge tank sizing, only trends that were observed. The total trapped mass was used to observe the engines ability to trap air within the cylinder. The more mass trapped the higher VE of the engine. The higher the trapped mass, the higher the VE of the engine which is optimal shown by an intake surge tank of 45L whether it was paired with an exhaust surge tank. The delta pressure throughout the EGR loop was used as a metric in the ability to control external EGR flow rates. The optimal solution would be to have a consistent delta pressure between the two tanks for the entire engine cycle. The optimal case includes 212L surge tanks on both the intake and exhaust. The last metric that was observed was regarding the test facilities ability to measure mass flow rate upstream of the engine. The optimal case being the largest intake surge tank 212L, with the 48L and 125L showing similar mass flowrates throughout the engine cycle.

Each metric points to a different combination of an optimal case of intake and/or exhaust surge tank. One other metric used to size the surge tanks was the ability to actually fit them onto the engine cart which will be discussed further in chapter 4.7. This surge tank study was used in achieving task 1.c determining the appropriate surge tank sizing. While the studies are great to show optimal tank sizing, manufacturing and cost were also constraints on the system. In turn, the surge tank size chosen for the both the intake and exhaust was 38L.

3.4 TPA Model

After the initial surge tank sweep was created a TPA model was calibrated to a 3D CFD model which includes a detailed kinetics model for combustion. A TPA is a method of analyzing data typically generated within the test cell to understand specific parameters such as heat transfer coefficients and trapped residuals. The TPA model requires cylinder pressure, fuel flow, intake, and exhaust pressure. With the SCRE no prior engine data had been obtained so the model was TPA model was calibrated to data provided by Westport from their 3D CFD model including combustion. According to McTaggart et al. Westport's 3D CFD model had been validated against both a SCRE and a multi-cylinder research engine using their HPDI injector [41]. The model used by Westport based in OpenFoam software uses their own in-house combustion code specifically developed for

the combustion of natural gas [41]. The intake pressures used for the TPA model were based upon constant regulated pressures assumed from the regulator to be used within the compressed air line in the test cell. The exhaust pressure used was generated based upon assumed constant pressure downstream from the exhaust surge tank that was to be set with an electronically controlled butterfly valve. The data that was shared by Westport fuel systems included three speed/load points.

The engine test conditions that the TPA model was calibrated to include A25, A50, and B100 shown in Table 3.6. The NG Mass gives the amount of NG injector per power stroke of the engine in mg/stroke, The T_{IVC} is the temperature in the combustion chamber at IVC. P_{IVC} is the pressure within the combustion chamber at IVC. The SOI was held constant at -10 °ATDC for each of the speed load cases. The bore, stroke, and CR were the same as given in Table 3.3. The fuel used within the TPA calibration was CNG with specific mass fractions of methane, propane, carbon dioxide and nitrogen shown in Table 3.7. The LHV of the fuel used for calibration was 47.50 MJ/kg.

Table 3.6: Engine Conditions for TPA Calibration

Mode	A25	A50	B100
EGR [%]	0	0	14
GRP [bar]	150	200	290
NG Mass [mg/str]	59	133	267
RPM	1200	1200	1500
T_{IVC} [K]	460	460	460
P_{IVC} [bar]	1.12	1.6	3.44
GSOI [°ATDC]	-10	-10	-10

Table 3.7: Fuel Composition CNG

Fuel composition		
Gas	Chemical Formula	Mass Fraction
Methane	CH_4	0.8300
Propane	C_3H_8	0.1293
Carbon dioxide	CO_2	0.0198
Nitrogen	N_2	0.0209
LHV (kJ/kg)		47.50
Stoichiometric AFR		16.22

Along with the CFD engine conditions and fuel composition, cylinder pressure, fuel flow rate, and apparent heat release data was provided from the CFD simulations for the TPA model calibration. Figure 3.9 shows the cylinder pressure vs. crank angle for the three test conditions low, medium, and high load. Case A25 is a low speed load with near atmospheric intake pressure and 0% Exhaust Gas Recirculation (EGR). Case A50 represents a 50% load case with 0% EGR, and case B100 is a peak load case at 1500 RPM with 14% external EGR.

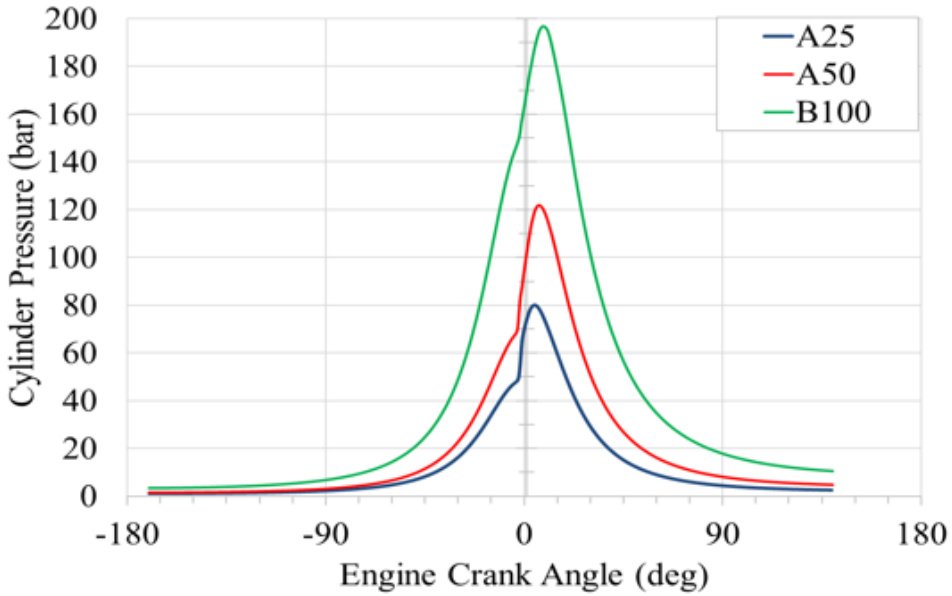

Figure 3.9: 3D CFD Combustion Model Cylinder Pressure vs. Crank Angle

The fuel flow rates vs. crank angle degrees were provided and are shown in Figure 3.10. The plot starts at -10° ATDC where the SOI is commanded, and the fuel flow rates start near -7.5° ATDC. The delay between the signal and fuel flow rates can be defined as the mechanical delay of the injector. Data from Figure 3.9, and Figure 3.10 were imported into GT-power to calibrate the TPA model.

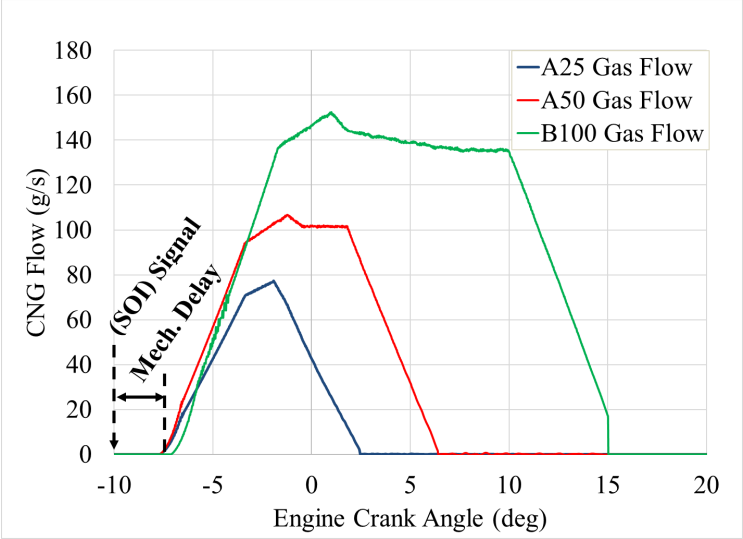

Figure 3.10: CNG Flow vs. Crank Angle

Figure 3.11 gives the apparent heat release (AHR) rate vs. crank angle for each of the load conditions. The AHR rate for the low speed load condition shows the highest initial peak AHR rate at 210 kJ/(m^3 -CAD). The units of AHR rate are conventionally given in kJ/CA° or J/CA°, but in this case the units were given in kJ/(m^3-CAD) where the AHR rate is normalized by the displaced volume within the cylinder. The initial burn of the low load case shows a large portion of pre-mixed combustion after the ID, followed by mixing controlled combustion, and a small portion of diffusion combustion, as the majority of the heat release is completed by 10° ATDC. Case A50 is the mid load case also showing a large amount of pre-mixed combustion with the AHR rate reaching 190 kJ/m^3 CAD, followed by a larger amount of mixing controlled combustion compared to A25 to reach the 50% load. The late combustion begins at 20° ATDC to near 90° ATDC as this rate is much lower than the initial mixing combustion from near TDC to 20° ATDC. Case B100 is the high load case showing the lowest peak AHR rate during the rapid combustion at the initial stages and the largest amount of mixing-rate controlled combustion from TDC to approximately 40° ATDC to reach the full load.

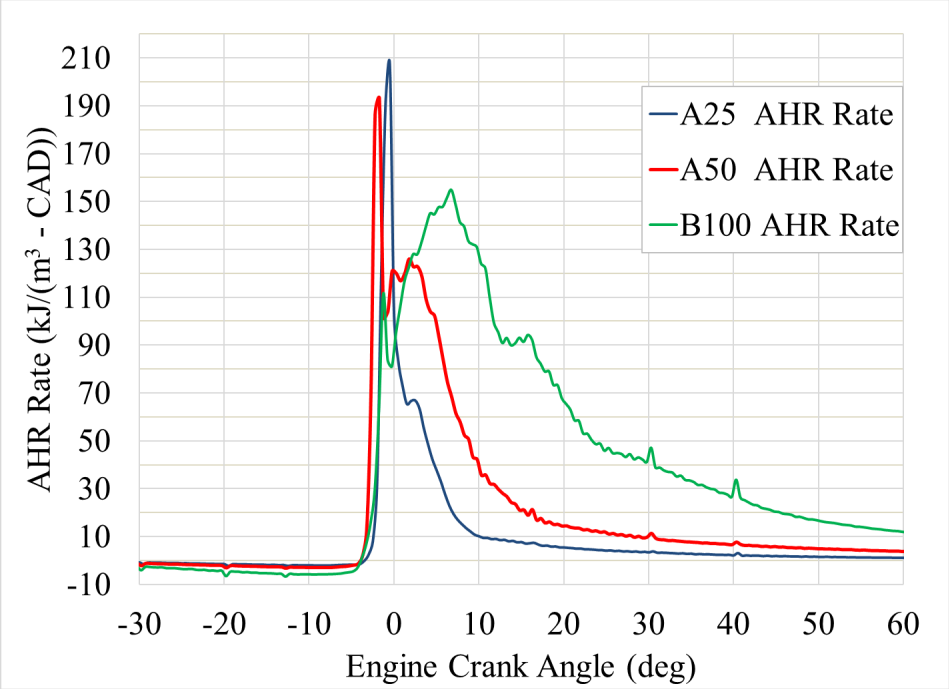

Figure 3.11: AHR Rate vs. Crank Angle

Figure 3.12 shows the TPA model compared to the simulated CFD data for pressure vs. crank angle. Although it is difficult to see, the simulated (TPA) and measured (CFD) overly precisely for each speed load case. Figure 3.13 shows the logP-logV diagram of all three load cases from the TPA model. Figure 3.13 also shows the start of combustion (SOC), IVO, IVC, EVO, and EVC on the logP-logV diagram.

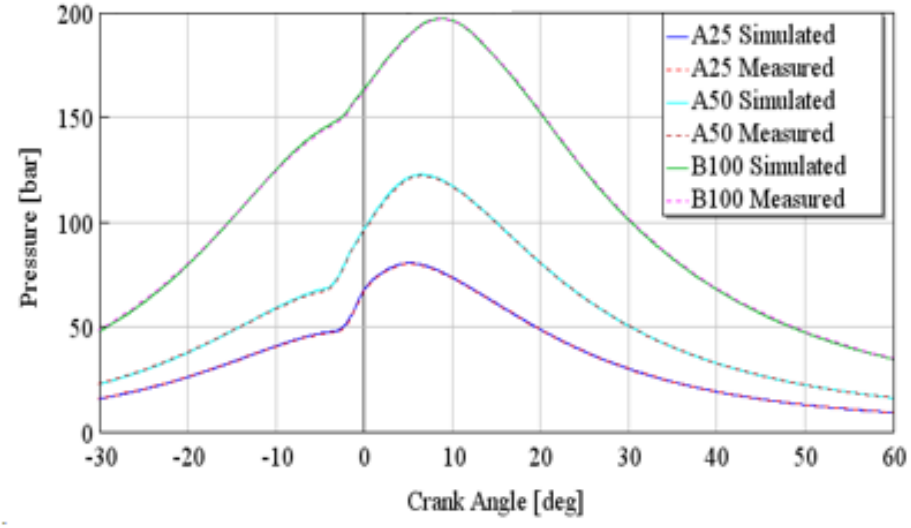

Figure 3.12: TPA vs. CFD (Cylinder Pressure vs. Crank Angle)

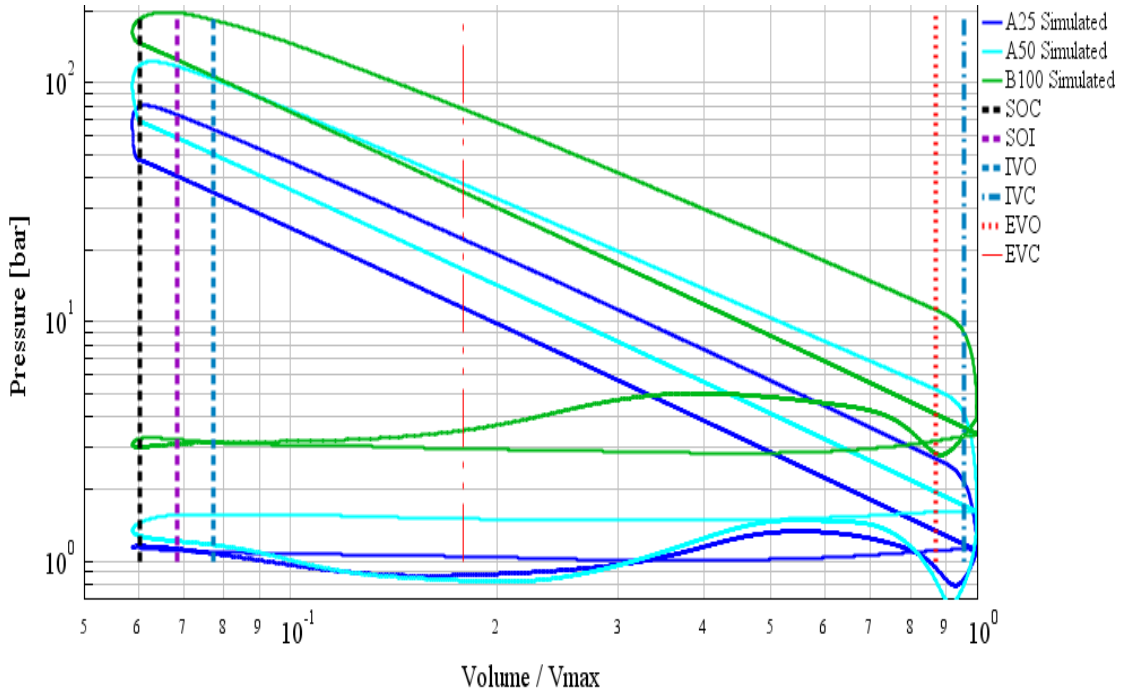

Figure 3.13: TPA Calibration (LogP-LogV)

From the TPA model calibration it is also important to understand the residuals trapped at each for each cycle. Because the CFD kinetics model only spanned from -170 to 140°ATDC the pumping loop and residuals is not well understood. Table 3.6 gives the breakdown of the CFD data provided and the simulated TPA data in comparison. The table also gives combustion metrics including 10% mass fraction burned (CA10), 50% mass fraction burned (CA50), burn duration (CA 10-90), Indicated Mean Effective Pressure Net ($IMEP_{NET}$), Indicated Specific Fuel Consumption (ISFC), and the tuned heat transfer multiplier (HT Multiplier) for each case. The trapped residuals show that 4.3% burned gas was trapped for mode A25, and 2.02% was trapped for mode A50. Mode B100 shows 17.05% trapped residuals when controlling the external EGR to 14%. The trapped residuals are the combination of both external EGR and internal trapped residuals due to valve overlap.

One important note is that the trend for the HT multiplier increases with load to maintain the proper cylinder pressure throughout the engine cycle. An important comparison for the TPA and CFD is the peak pressure and location of peak pressure. Each case presents less than a 0.6 bar and 0.2° error for peak pressure, and location of peak pressure,

respectively. The $IMEP_{NET}$ was calculated at 5.2, 10.9, and 19.2 bar for engine modes A25, A50, and B100, respectively. The TPA model was the first step in calibrating a combustion model for SCRE CI DI CNG engine as given in section **Error! Bookmark not defined.**.

Table 3.8: TPA Engine Mode Breakdown

Mode	A25 (CFD) "Measured"	A25 (TPA) "Simulated"	A50 (CFD) "Measured"	A50 (TPA) "Simulated"	B100 (CFD) "Measured"	B100 (TPA) "Simulated"
EQR	0.44		0.67		0.77	
EGR+ Residuals [%]	0	4.30	0	2.02	14	17.05
GRP [bar]	150	150	200	200	290	290
NG Mass [mg/str]	59	59	133	133	267	267
RPM	1200	1200	1200	1200	1500	1500
T_{IVC} [K]	460	454	460	454	460	461
P_{IVC} [bar]	1.12	1.12	1.61	1.62	3.44	3.42
GSOI	-10	-10	-10	-10	-10	-10
Peak Pressure [bar]	80.0	80.4	121.9	122.5	196.7	196.8
Location of Peak Pressure [°ATDC]	5.0	5.2	6.5	6.5	8.6	8.6
CA10 [°ATDC]	-1	-1.8	-1.5	-2.2	1.8	1.1
CA50 [°ATDC]	1.5	0.8	5	3.5	14.5	12.02
CA 10-90 [°deg]	14.0	15.6	41.3	39.7	53.2	49.8
$IMEP_{GROSS}$ [bar]	4.9	5.1	10.2	10.5	19.3	20.3
$ISFC_{GROSS}$ [g/kw-hr]	174	167	188	183	199	189
HT Multiplier	1		1.4		2.2	

3.5 Calibrate DI-Pulse Ignition Model

With a calibrated baseline TPA model the next step was setting up a calibrated DI-Pulse model. While the TPA model provided essential data for the pumping loop, and internal EGR, the DI-Pulse model allows the user to calibrate the model to a specified apparent heat release rate of each engine mode. The DI-Pulse allows for a predictive combustion model once calibrated correctly which allows for a better understanding of engine performance with respect to changes within the engine operating conditions including intake air temperature, boost pressure, CR, EGR, and SOI. The DI-Pulse model is used conventionally for diesel direct injection engine models. The conventional DI-pulse model had to be adjusted for the CNG fuel, specifically for the large difference in ID with respect to temperature for CNG fuel.

The goal of calibrating the DI-pulse model was to observe changes in CI-DI of NG engine performance with respect to changes in engine design, and operating parameters. The parameters that were varied within the model after calibration include valve timing, IAT, MAP, SOI, and CR. The parameters observed with respect to performance include heat transfer, combustion metrics including ignition delay, combustion phasing (CA50), burn duration (CA10-90°), and indicated efficiency. This process of calibrating the model to prior work conducted by Westport was an important task when designing the CR bowls and intake heater required for proper engine operation of the SCRE.

3.5.1 CNG DI-Pulse Ignition Delay Calibration

To calibrate the DI-Pulse model correctly. As mentioned prior, the DI-Pulse model is built specifically for diesel type fuels with high Cetane values (i.e. 40-60). With the fuel being switched to CNG the combustion model had to be varied to alter the ignition delay characteristics of CNG with respect to temperature. Equation 3.5 gives the Arrhenius expression for the ignition delay used within the GT-power DI-Pulse model.

$$\tau_{ign} = C_{ign} \times \rho^{-1.5} \exp\left(\frac{3500}{T}\right)[O_2]^{-0.5} \quad 3.5$$

Tau gives the ignition delay in ms where C_{ign} is the ignition delay multiplier, rho is the pulse gas density (fuel), T is the temperature in Kelvin, and O_2 is the oxygen concentration. Ignition occurs when the integral of equation 3.6 is equal to one.

$$\int_{\tau_0}^{\tau_{ign}} \frac{1}{\tau_{ign}} dt = 1 \quad 3.6$$

The 3500 is derived from a diesel type fuel activation energy and the universal gas constant. Equation 3.7 given by Naber et al., gives another Arrhenius expression for the ignition delay of NG.

$$\tau_{pd} = \{C^2 + [A * [\left(\frac{p}{p_0}\right)^{-r} \times \exp\left(\frac{E_a}{\tilde{R}T_c}\right)]^2\}^{\frac{1}{2}} \quad [11] \quad 3.7$$

Comparing equation 3.5 to equation 3.7 given by Naber et al. we can see that the value of 3500K within equation 3.5 can be related to the value $E_a/\tilde{R}$ (K) activation temperature in equation 3.7. E_a is the apparent activation energy in J/mol and $\tilde{R}$ is the universal gas constant 8.314 J/mol-K. The value of T or T_c is the bulk gas temperature in Kelvin within the cylinder or combustion chamber when the ignition delay occurs.

Naber et al. report various values of $E_a/\tilde{R}$ (K) ranging from a minimum of 11504K for methane to a maximum of 12630K for mean natural gas. The values reported were derived from measured fits to experimentally measured pressure delays for various fuels. One thing to note is that the value $E_a/\tilde{R}$ (K) values reported by Naber, are much higher than the baseline GT-power value of 3500K. This difference in activation temperature between equation 3.5 and 3.7 is due to the fuel properties from an assumed diesel fuel and the required activation temperature range of near 12000K for NG.

Equation 3.5 is used for the DI-pulse GT-power model, typically used for diesel fueled engines. Accepted diesel activation energies according Senachin et al. activation energy at mixture concentrations at stoichiometric, range from 25,000 to 77000 J/mol [43]. If activation energy is calculated from activation temperature (3500K) in equation 3.5, it

calculates to 29,099 J/mol. This value falls within the approximate range of overall reaction activation energy reported by Senachin et al [43].

Equation 3.7 is experimentally measured based upon methane and natural gas auto-ignition pressure delay measurement correlations. The values reported for activation energy based upon the reported activation temperature range, 11,540K to 12,630K calculate to 95,943 to 105006 J/mol for methane and natural gas mean, respectively. The values reported by Naber et al. are much higher than a typical diesel fuel which requires an adjustment in equation 3.5 for proper model calibration for auto-ignition of NG.

To properly calibrate an ignition model that varied with temperature, the activation temperature had to be varied from its original value of 3500K to a value closer to 12000K to be more representative of natural gas auto-ignition. While typically the only multiplier available when calibrating equation 3.5 within the DI-pulse model is the ignition delay multiplier (C_{ign}), a special template was used to vary the activation temperature of the model. The special template allowed for a multiplying factor of the base equation 3500K activation temperature. The multiplying factor was chosen as 3.4 to change the value from 3,500K to 11,900K an approximate mid-range value within the ranges reported by Naber et al.

First, multiple ignition delay values were overlaid on a temperature vs. ignition delay plot from multiple sources to understand the range of reported ignition delay values for natural gas auto-ignition processes. The first three lines shown in Figure 3.14 represent mean natural gas auto-ignition values based upon the measured fit equations reported by Naber et. al. The recorded ignition delays for from Sandia National Laboratory were recorded in a constant volume combustion chamber (CVCC). The density is varied across the first three lines showing a decrease in ignition delay when temperature is constant, and the density is increased. The fuel used for the ignition delay values for lines one through three within the CVCC is mean natural gas with an activation temperature of 12,630K. The fourth line shown in yellow comes from an experimental engine study by Oliver et al. The Waukesha CFR engine was tested at 1800 RPM approximately 5 bar

IMEPnet at CR of 17:1 with IAT ranging from 225°C to 275°C using neat methane as the fuel. The temperatures at TDC were calculated from the isentropic compression process for the comparison of the data shown. The values reported by Oliver et al. were in crank angle degrees (CAD), they were converted to ms based upon the conversion factor of 0.0925 ms/deg at 1800 RPM. The range of ignition delays is 1.43 ms to 2.04 ms for constant EOC pressure (65 bar) at 1800 RPM at TDC temperatures ranging from 1130K to 1282K.

The fifth and sixth lines shown in Figure 3.14 were generated by Westport fuel systems Inc. using a kinematics simulation to calculate ignition delay of low ethane and high ethane natural gas. The pressure at EOC for both simulations was 100bar. The ignition delay values from the kinematics simulation show a lower ignition delay based on the mechanics being solely tied to the chemical processes within the equations used and negating losses based upon fuel to air mixing rate. The last value shown in Figure 3.14 is a star 1.5 ms and 1180K TDC temperature. This value was also generated by Westport fuel systems using a 3D CFD model coupled with the chemical kinetics combustion model at 100bar EOC pressure.

The comparison of ignition delays seems to show similar results for multiple methods of obtaining the delay process including CVCC, engine experimentation, kinematic, and CFD simulations. A box has been drawn around the respective temperature range that is planned to be studied experimentally ranging from 2ms as this is a typical diesel ignition delay high limit, and temperatures from 1050K to 1350K. The temperature region is enclosed by what is most likely the lower limit that auto-ignition will be achievable, and the upper limit, which is constrained by the max cylinder temperature achievable within the engine. The purpose of the comparison between each of the analyzed sets of data, was to understand what has been completed prior and how well the data compares. This comparison shows good agreement which increases the confidence in modeling the ignition delay of the DI-Pulse model with respect to the data presented by Naber et al.

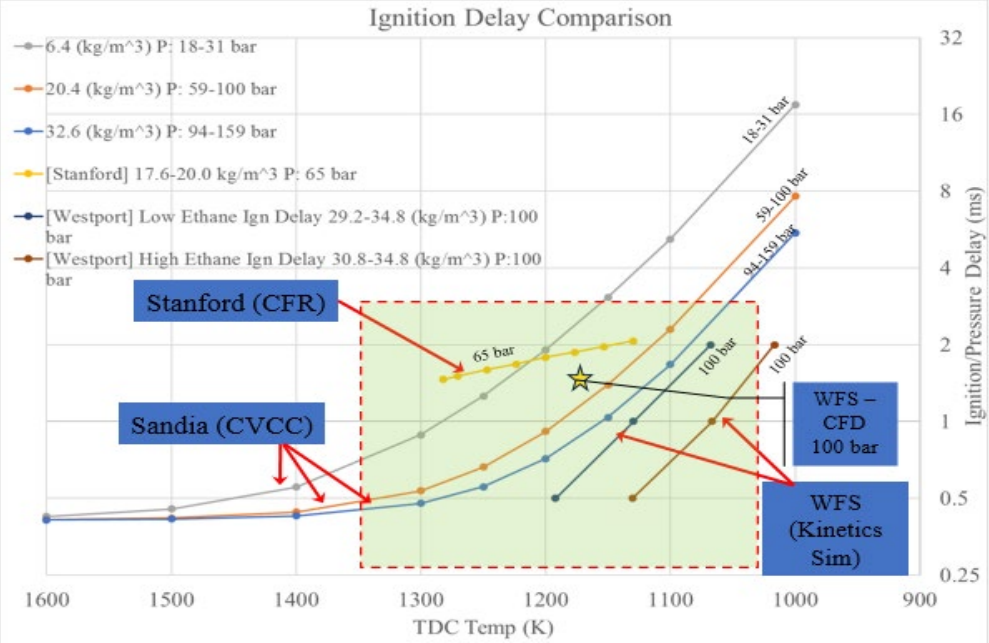

Figure 3.14: Ignition Delay Comparison

With an understanding of the various ignition delay values at various temperatures from multiple sources, the model was then simulated to ensure the activation temperature of 11,900K was appropriate. With the changing of the activation temperature multiplier from 1 to 3.4, the ignition delay multiplier also had to be adjusted to better fit the ignition delay values. Figure 3.15 shows the ignition delays obtained from the GT-power model. The model was setup using natural gas fuel composition given in Table 3.7 and engine parameters given in Table 3.2. First, the model was simulated at using MAP of 2 bar using an ignition delay multiplier of 1 shown as the red line presenting ignition delay values near .25 ms at 1800 RPM. The model then increased the ignition delay multiplier to values of 2 and 3 holding the activation temperature multiplier constant at 1 shown in the green and yellow lines in Figure 3.15 respectively. The trend with increasing the ignition delay multiplier is obvious, increasing only the nominal value, but there is no change with respect to temperature over the range of 1000-1200K for the three lines shown. The next portion of the sweep was to increase only the activation temperature multiplier to 1.8 while holding the ignition delay multiplier constant at 1 shown as the red boxes with the black + sign in Figure 3.15. The effect of increasing the activation temperature multiplier shows an obvious change in the slope of the ignition delay with

respect to temperature over the range of 1150K to 1050K. The slope was still not as steep as the values reported by Naber et al. because the activation temperature with a multiplier of 1.8 is only 6300K just over half of the target value of 11,900K. The change in the activation temperature not only influenced the slope, but also shifted the values upwards with a TDC temperature of 1150K the value had changed from its baseline value of 0.25 ms to 1.6 ms.

The model was then changed to have an activation temperature of 11,900K by using a multiplier of 3.4 (i.e. 11,900K=3.4*3500K). With the adjustment of the activation temperature to 11,900K, the ignition delay multiplier was first tested with ID multiplier of 1, but the ignition delay values were much too high. It was found that when using an AT multiplier of 3.4, an ID multiplier ranging from .001 to .004 was effective in achieving predictable ignition delay values when calibrating the model to the values obtained by Sandia in triangles. The AT multiplier was held constant at 3.4 and the ID multiplier was swept in .001 increments to from .001 to .004 shown as the circle values on Figure 3.15. The model was then decreased in pressure (decreasing density) to check the effects on ignition delay, these values are shown in diamonds on Figure 3.15. The increase in ignition delay with a decrease in density in Figure 3.15 is representative effects described by Naber et al. shown in Figure 3.14. This multiplier sweep allowed for a baseline calibration of the DI-pulse model using an updated AT multiplier of 3.4 and better understanding the range of ID multipliers required with a change in AT to achieve representative ID's using GT-power.

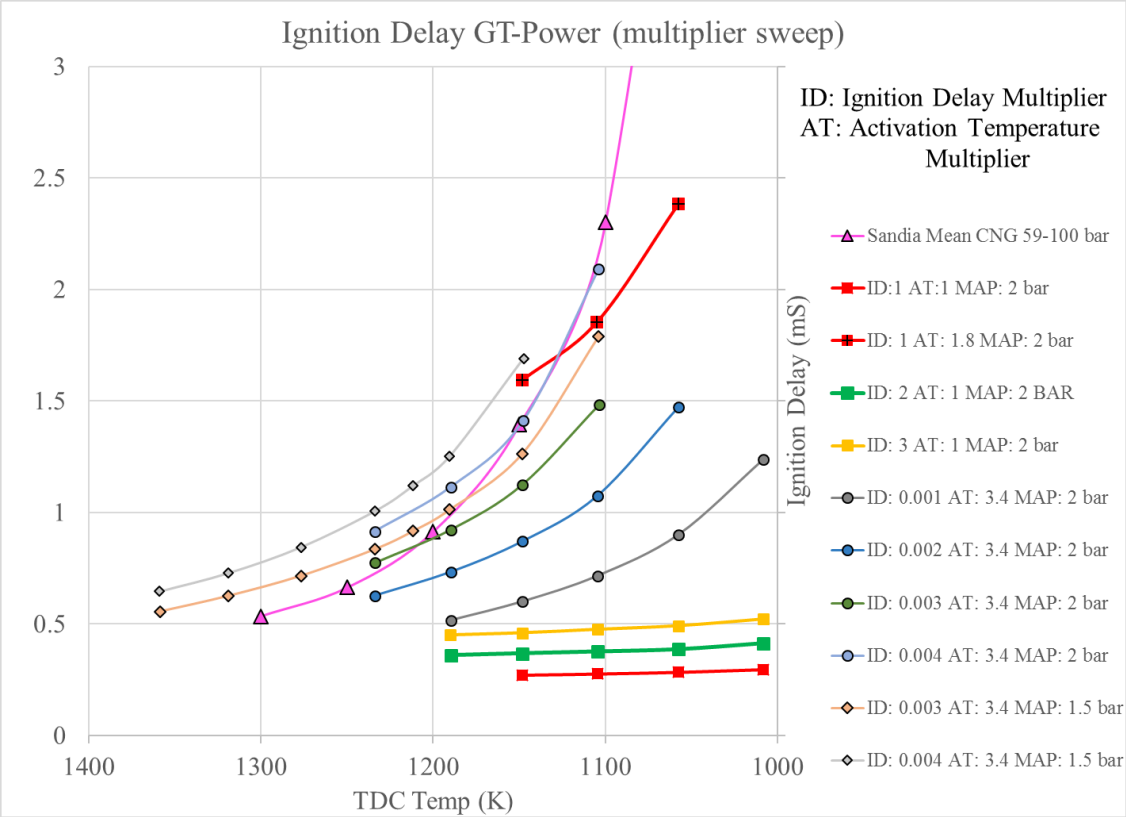

Figure 3.15: Ignition Delay GT-Power Multiplier Sweep

3.5.2 Integrated Design Optimizer DI-pulse Calibration

With the change in activation temperature to a CNG relevant value (11,900K), it was possible to fully calibrate the DI-pulse model to the CFD results given by Westport. The DI-pulse model contains four multiplier parameters excluding the additional parameter for AT of 3.4 including entrainment multiplier, pre-mixed combustion multiplier, diffusion combustion multiplier, and ignition delay multiplier. All four values can be optimized when calibrating the model. The entrainment portion relates the injector spray and air mixing into the fuel. With a direct injection engine, the ignition occurs near a stoichiometric mixture while overall the cylinder constituents are typically lean. The model uses the liquid fuel density, velocity at the spray tip, spray tip length and other variables to determine the air entrainment and the slowing down of the fuel pulse. The entrainment equation is derived from a conservation of momentum and is calibrated using the entrainment rate multiplier (C_{ent}). Premixed combustion is the portion of the fuel that

burns after the initial pulse ignites just post ignition delay. This portion of the fuel burned typically has a high heat release rate, and it is kinetically limited. The overall premixed combustion process is varied by the premixed combustion rate multiplier (C_{PM}). Diffusion combustion is the portion of the combustion after the premixed combustion has finalized and is controlled by the mixing of air and fuel, and the amount of fuel being added to the already burning mixture. The rate of diffusion combustion is varied by increasing or decreasing the diffusion combustion rate multiplier (C_{df}). The values for the four multipliers C_{ign}, C_{ent}, C_{pm}, C_{df} were calibrated to three speed load points given in Table 3.6, the same speed/loads as the TPA. To simplify the user portion of the calibration, an Integrated Design Optimizer (IDO) was used to minimize the error between the measured AHR rate calculated from the TPA, and the predicted AHR rate generated from the DI-pulse model. All values from the TPA were transferred to the DI-pulse model except the individual heat transfer coefficients and the EGR trapped residuals determined from the TPA when running the DI-pulse closed volume IDO.

The IDO allowed for hundreds of cases of the multipliers to be used to minimize the error between the predictive combustion model and the measured CFD combustion results provided by Westport. While typically you would use experimental engine results to calibrate the DI-pulse model there are currently no results available for calibration, so the CFD combustion data was chosen for 1D DI-pulse predictive calibration. Table 3.9 shows the setup for each of the cases including the minimum and maximum values for optimizer limits for each combustion multiplier. The activation temperature multiplier (C_{AT}) was held constant at 3.4 for each case, while still allowing C_{ign} to vary between .0005 and .003 for fine adjustment of the ID. Along with the min and max for each multiplier, the optimum calibration values for each engine mode case (A25, A50, B100) are given in Table 3.9.

Table 3.9: Integrated Design Optimizer Case Setup

Mode A25 IDO Setup				Mode A50 IDO Setup				Mode B100 IDO Setup				All Modes	
Multiplier	Min	Max	Optimal	Multiplier	Min	Max	Optimal	Multiplier	Min	Max	Optimal	Average Optimal	Standard Deviation
C_{ent}	0.25	1.25	0.678	C_{ent}	0.25	1.25	0.594	C_{ent}	0.25	1.25	1.091	0.788	0.2172
C_{pm}	0.5	2.5	1.103	C_{pm}	0.5	2.5	0.796	C_{pm}	0.5	2.5	0.651	0.850	0.1884
C_{df}	0.5	2.5	1.332	C_{df}	0.5	2.5	1.177	C_{df}	0.5	2.5	0.75	1.086	0.2461
C_{ign}	0.0005	0.002	0.0016	C_{ign}	0.0005	0.003	0.0005	C_{ign}	0.0005	0.003	0.0014	0.001	0.0005
C_{AT}	3.4	3.4	3.4	C_{AT}	3.4	3.4	3.4	C_{AT}	3.4	3.4	3.4	3.400	0.0000

Each speed load case was setup to run under the specified minimum and maximum until the multipliers converged and minimum change in AHR rate root mean squared (RMS) was observed. The AHR rate RMS is calculated from the error between the predictive DI-pulse combustion model and the measured CFD combustion data. Figure 3.16 shows the AHR rate RMS vs. Case number for the IDO for engine mode A25. As the cases lengthened for engine mode A25, the RMS value seems to change very little past case 300. The optimal RMS was recorded at 0.00363 for engine mode A25 from using multipliers given in Table 3.9 (Mode A25). Figure 3.17 shows the individual multiplier values for mode A25 vs. case number along with a dashed line at the optimal value for each multiplier. Each of the values is varied continuously with the objective of minimizing the AHR rate RMS. The AHR rate RMS vs. case number for engine modes A50 and B100 and their respective individual multipliers vs. case number are found in Appendix A.3. The optimal multiplier values for case A50 and B100 are given in Table 3.9. Average multiplier values for a three-case spanned calibration are given in Table 3.9 along with the standard deviation. The difference between each of the individual calibrations was deemed different enough from average to not move forward with using average multiplier values for further calibrations. It was decided that further investigations at each engine mode would use the individual optimal calibrations rather than an average value.

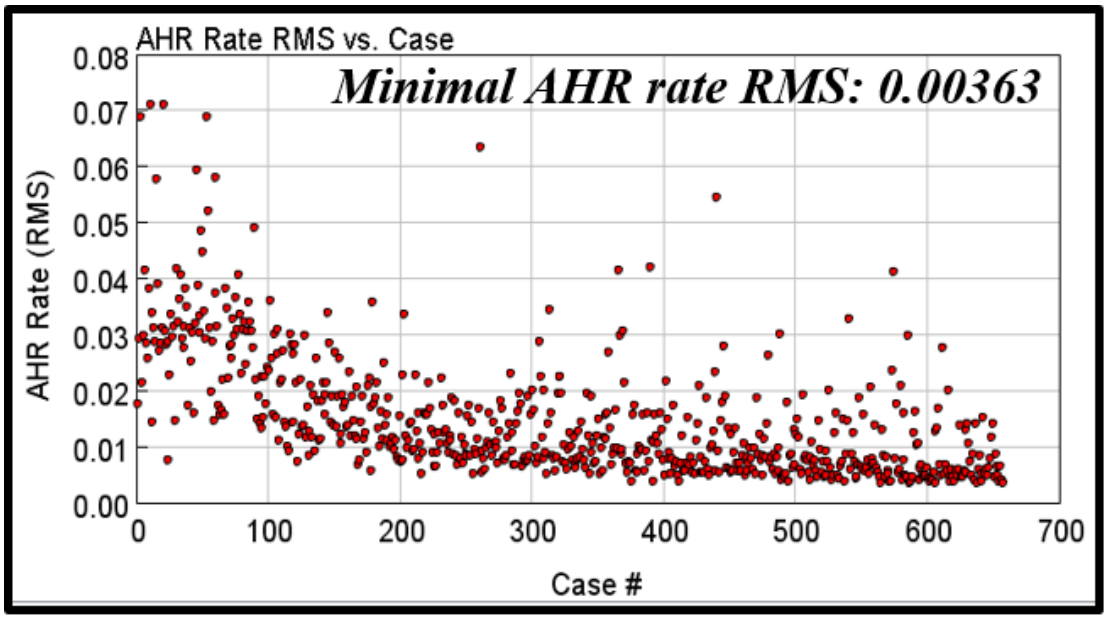

Figure 3.16: AHR Rate RMS vs. Case (A25 IDO)

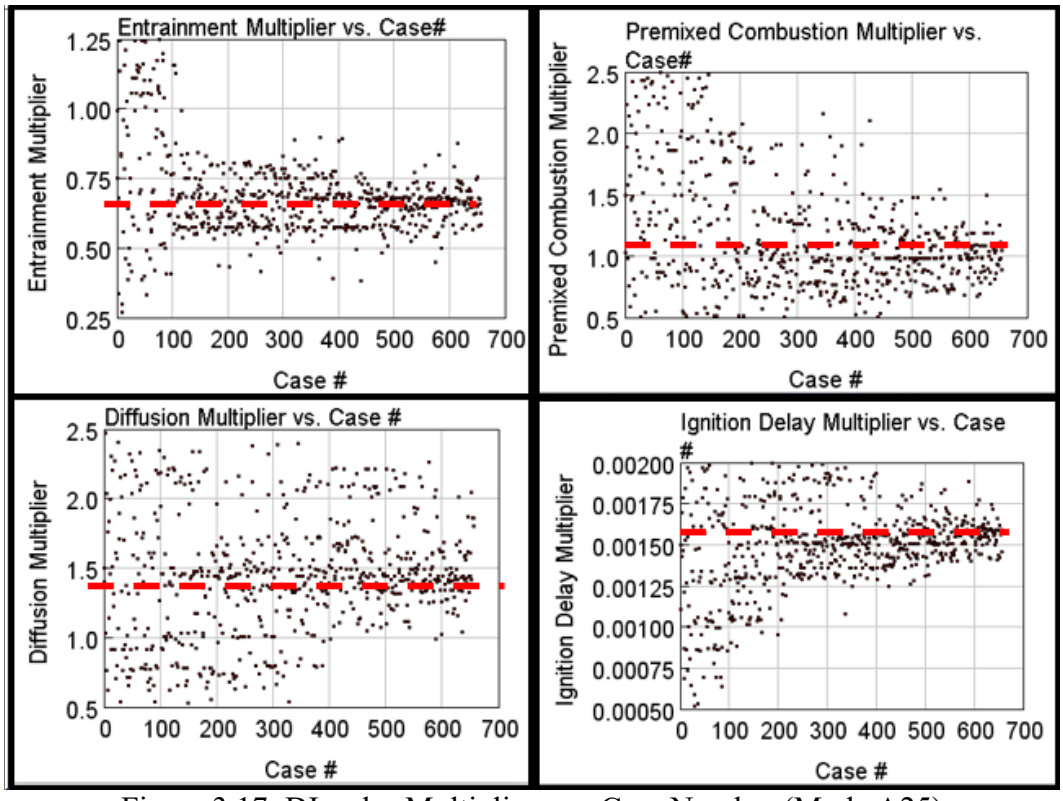

Figure 3.17: DI-pulse Multipliers vs. Case Number (Mode A25)

After the IDO was completed, the measured vs. predictive (DI-pulse) was analyzed. Figure 3.18 gives the comparison of measured vs. DI-Pulse AHR rate for each engine mode. The comparison between the measured and DI-pulse for A25 is shown in the solid lines with almost an exact overlay between the two AHR rates. Mode A50 is shown in the small, dashed lines with a slight error occurring during the diffusion combustion region of the AHR rate and an almost exact correlation during the premixed combustion. Mode B100 comparison given by the long dashes between measured and DI-pulse shows very similar results with a slight error occurring during the transition from pre-mixed combustion to diffusion combustion. Overall, the AHR rate comparison visually represents proper calibration of the four combustion multipliers after the IDO process was completed.

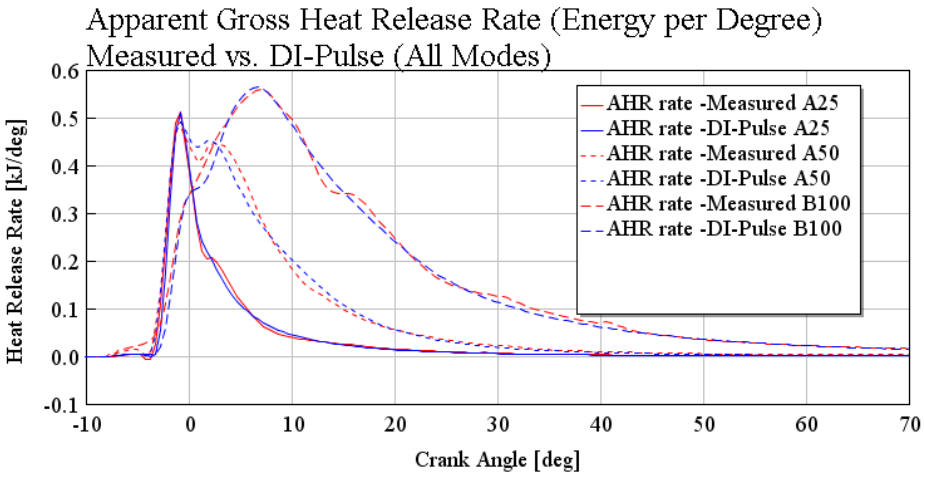

Figure 3.18: AHR Rate Measured vs. DI-Pulse (All Modes)

Further analysis and comparison of the predictive DI-pulse and measured data was also completed on all three engine modes. Table 3.10 gives error values given by GT-power to assist in quantifying the error between the measured (CFD data provided by Westport) and predictive model. The first value given in the error section is the IMEP error during combustion (from the start of combustion to CA90) in bar. All engine modes show less than 0.1 bar and under 1% error during the combustion process indicating a properly calibrated model. The LHV multiplier is also an indicator of a properly calibrated model. The values should be close to 1.00 indicating no fuel energy had to be removed or added

to meet the specified measured heat release curve. Each of the engine mode calibrations observed less than or equal to 0.003 delta compared to the optimum value of 1.000 for the LHV multiplier. The pressure RMS taken from the TPA and DI-pulse shows a very small value for each engine mode ensuring the model was calibrated correctly. The ignition delay for each case was also presented showing values near 0.7 ms which is well under the maximum allowable of 2.0 ms as suggested by Oliver et. al [25].

Table 3.10: IDO DI-Pulse vs. Measured/TPA

	A25 DI-Pulse	A50 DI-Pulse	B100 DI-Pulse
Ignition Delay [°deg/ms]	5.3/0.74	5.3/0.74	6.2/0.69
IMEP Error During Combustion Meas. Vs. DI-Pulse [bar]	-0.006	0.099	0.093
IMEP Percent Error During Combustion Meas. Vs. DI-Pulse [%]	-0.11	0.88	0.44
LHV Multiplier	1.002	1.002	0.997
Pressure Error RMS (TPA. Vs. DI-Pulse)	0.008	0.009	0.009

Again, the DI-Pulse IDO calibration was required to obtain engine mode specific multipliers for the DI-CI NG SCRE. Without a properly calibrated DI-Pulse model, further analysis on combustion predictions at varied IAT, MAP, CR, SOI, and cam timing would be insufficient and most likely not accurate. This calibration process was critical in further design and development when understanding the optimal choice for CR and IAT requirements moving forward with the SCRE design and build.

3.6 DOE Sweeping CR, SOI, IAT with a calibrated DI-Pulse Model

With a properly calibrated predictive DI-pulse combustion model, it was possible to further analyze the effects of other controlled parameters on each engine mode. The independent variables selected for further analysis included CR, SOI, and IAT. Each engine mode was set up to constrain the air charge and fuel mass to be consistent across the entire sweep. Other parameters that were kept constant included using the optimal

parameters from the IDO for each individual engine mode. The reason for sweeping the CR was to increase overall EOC temperatures while minimizing the required IAT. The sweep of IAT was required to determine the effects of IAT on each of the CR values chosen for the sweep including combustion metrics like ID, CA50, and burn duration.

3.6.1 Effect of IAT and CR on Engine Performance

The first analysis to be considered consists of constant SOI while varying both the IAT and CR. With keeping the charge constant, the effects of both CR and IAT on peak cylinder pressure are shown in Figure 3.19. As CR is increased the peak pressure at TDC prior to combustion also increases. With an increase in temperature, the peak motoring pressure also increases, but at a lower rate compared to CR. For example, at a CR of 25 and IAT of 350K the peak pressure motoring is 268 bar while at 450K IAT the peak motoring pressure has increased 32 bar. With an increase from 20 to 22:1 CR the same change in peak motoring pressure (32 bar) is observed. The same trend is observed at each engine mode from the nature of the isentropic compression process. The results from mode A25 and A50 for the same plots are given in Appendix A.4.

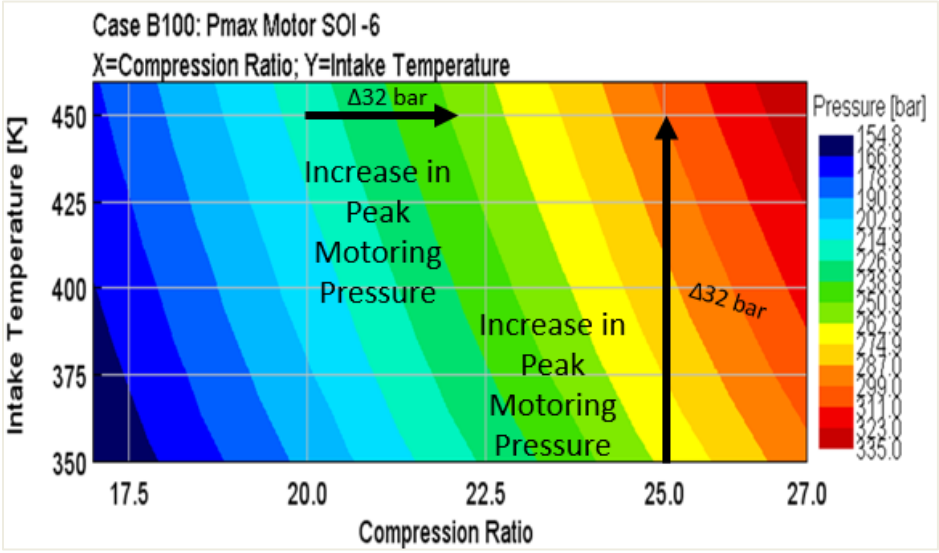

Figure 3.19: Peak Pressure Motoring IAT vs. CR (Mode B100)

The second important engine characteristic analyzed was the peak motoring temperature against CR and IAT. While the 0D analysis showed an initial calculation method for IAT

at TDC, the 1D model was utilized to confirm these values. Figure 3.20 gives the peak motoring temperature as a color contour against CR and IAT for mode A50. An increase in both CR and IAT results in an increase in peak temperature motoring. Another observation from Figure 3.20 is the minimum temperature required for ignition of CNG at approximately 1055K peak motoring temperature. Temperatures below this value resulted in incomplete combustion where the NG mixture did not ignite.

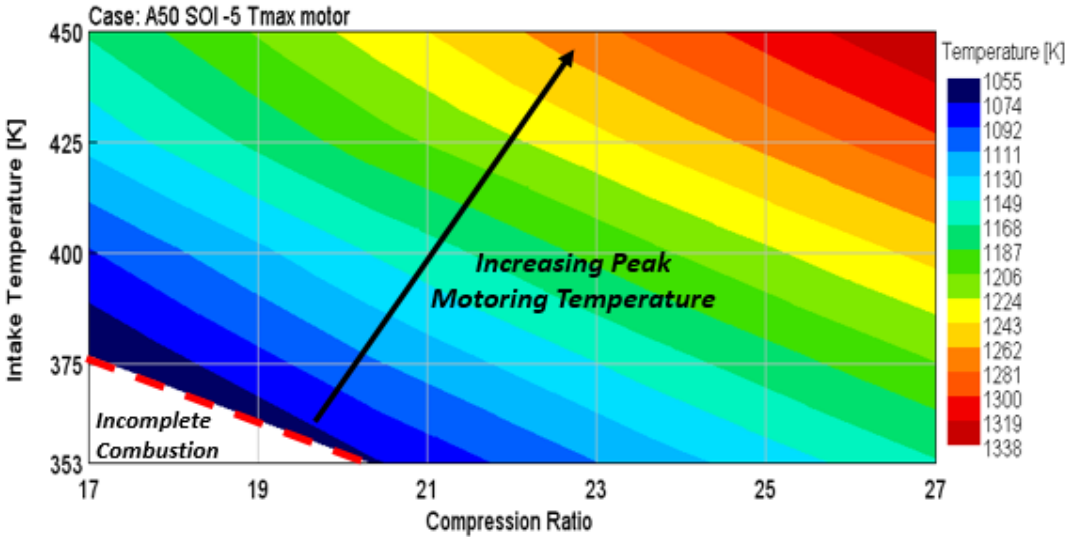

Figure 3.20: Peak Temperature Motoring IAT vs. CR (Mode A50)

It is also important to look at engine mode A25 peak cylinder temperatures motoring for the same CR and IAT sweep. The trend comparing mode A25 is almost exact, at the same temperatures, and CR across the range of the sweep although both the fuel and air quantities are changed, but the incomplete combustion occurs at higher temperatures for mode A25 compared to A50. The reason for not being able to maintain combustion at lower temperatures is due to the overall lambda and the amount of excess oxygen within the cylinder. Mode A25 has much more excess oxygen with a higher lambda than mode A50 resulting in a higher required IAT and or CR to maintain proper combustion.

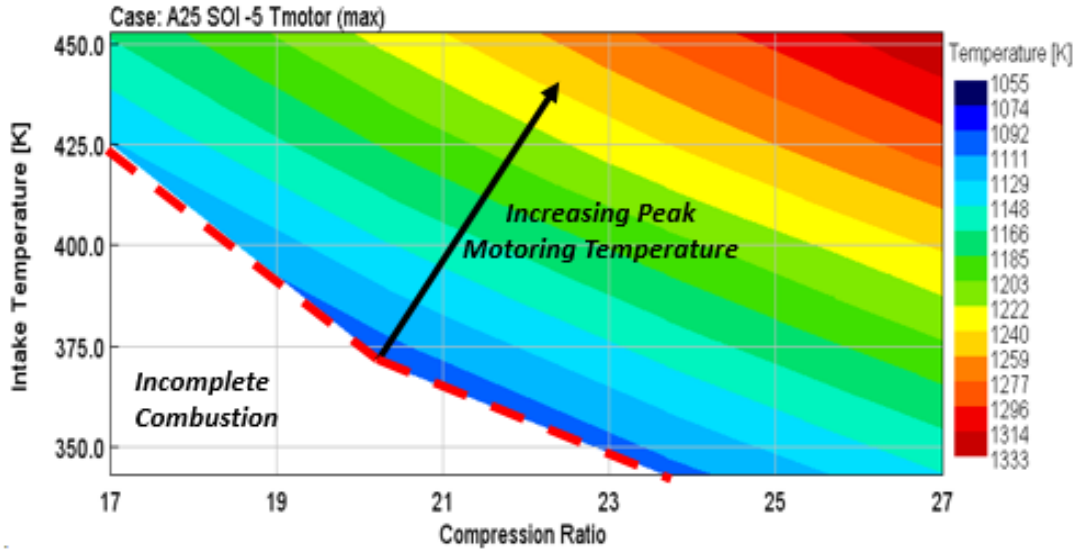

Figure 3.21: Peak Temperature Motoring IAT vs. CR (Mode A25)

After the peak temperature motoring was analyzed, the effect of CR and IAT on ignition delay was analyzed for the DOE. Figure 3.22 shows the ignition delay contour against CR vs. IAT for mode A50. Because the ignition delay model was calibrated with the correct AT, the trend for ignition delay shows very similar results to the peak temperature motoring. As the peak motoring temperature is increased the ignition delay decreases. Increasing either CR or IAT results in a shorter ignition delay due to higher temperatures at EOC. The longest ignition delay simulated for mode A50 was at a CR of 17 and IAT of 375K (102°C) at 1.33 ms. Another important observation from Figure 3.22 is the spacing of the contour with the increase of CR and IAT indicating the lower temperatures have larger impact on the change in ignition delay times. This is also noticed from the decreasing slopes shown in Figure 3.14 and Figure 3.15 as TDC temperatures increase. Comparing Figure 3.20 and Figure 3.22, at a CR of 25 and IAT of 425K the TDC temperature motoring is approximately 1275K, and the ignition delay is 0.427 ms. Increasing the IAT above 425K (152°C) results in little to no change in ignition delay according to Figure 3.22. Figure 3.23 gives the ignition delay contour against CR vs. IAT showing the higher temperature required to maintain combustion due to the excess oxygen. The lambda for case A25 was maintained at 2.12 while lambda for mode A50

was maintained at 1.31. The decrease in oxygen concentration decreasing lambda, results in combustion occurring at lower temperatures.

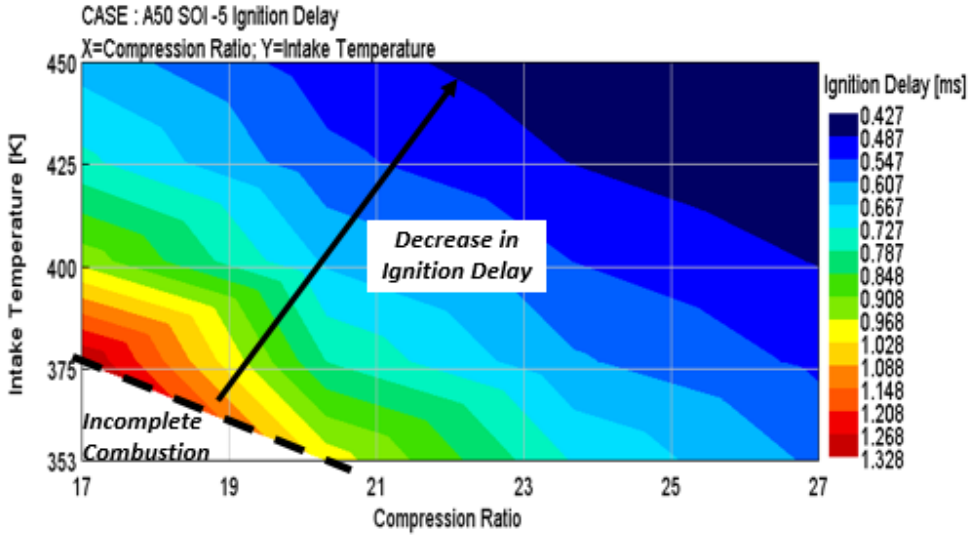

Figure 3.22: Ignition Delay CR vs. IAT Mode A50

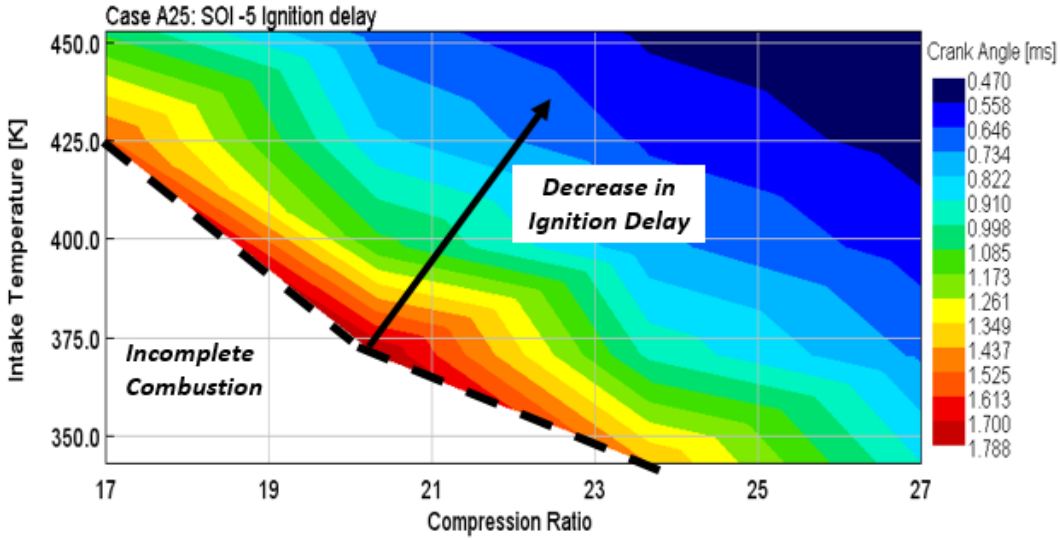

Figure 3.23: Ignition Delay CR vs. IAT Mode A25

Next, looking further into the effects of IAT temperature and CR on the combustion process. Figure 3.24 shows the effect of increasing only CR on the AHR rate. With increasing only, the CR while leaving the IAT constant an increase in peak temperatures prior to combustion (motoring) is observed. The increase in temperature at TDC decreases the ID. With a decrease in ignition delay, maintaining the same fuel flow rate, a

shift of combustion from premixed to diffusion combustion is observed decreasing the peak heat release rate as well, observed in Figure 3.24. An important observation from Figure 3.24 is the lowest CR 17 shows an extremely high AHR rate compared to the other higher three CR. Because the ignition delay is so late half the fuel has been injected into the cylinder prior to combustion allowing for an extremely high premixed combustion process. This can be mitigated by either increasing CR or IAT.

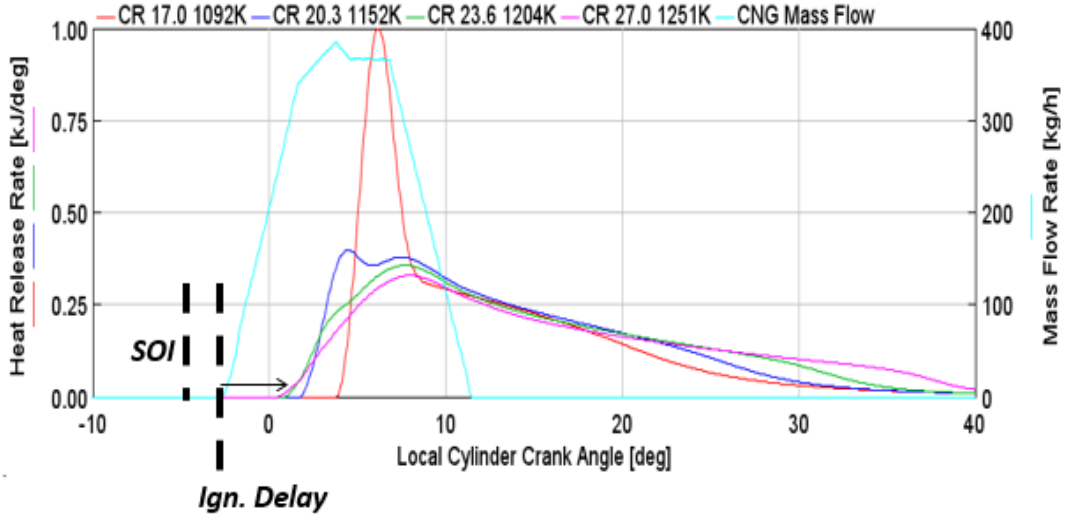

Figure 3.24: Effect of CR only on AHR Rate Mode A50 IAT 401K (128°C)

Figure 3.25 shows the cylinder pressure vs. crank angle for the same AHR rate data set shown in Figure 3.24. The effect of the ID on the combustion process is evident from the increase in rate of pressure rise from when comparing CR 17 to CR 27. The importance of this figure is the change in pressure rise when using the same IAT and varying CR. It also points out that at a lower CR to mitigate the high rate of pressure rise due to increased ID, a higher IAT is required.

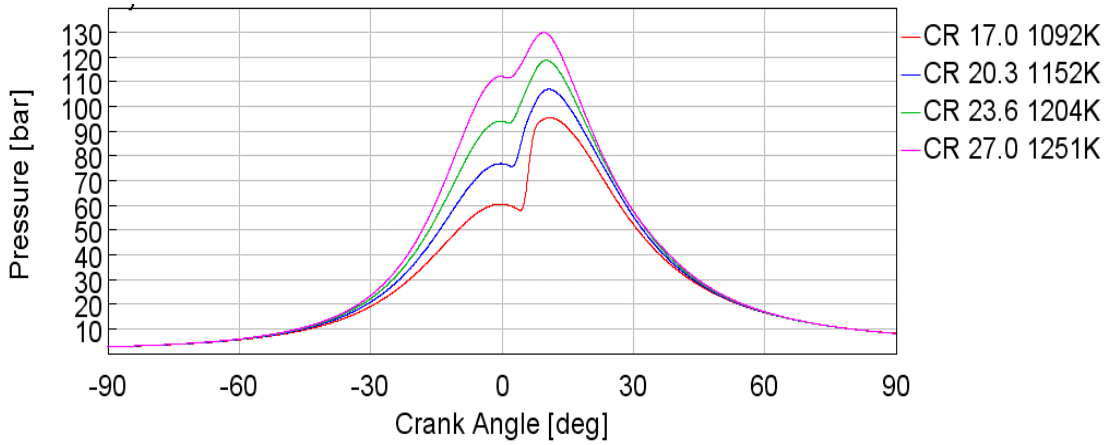

Figure 3.25: Cylinder Pressure vs. Crank Angle Deg. Mode A50 IAT: 401K (128°C)

With increasing CR, we see an increase in EOC temperatures, as well as when increasing the IAT. Figure 3.26 shows the AHR rate vs. CA° for constant CR of 20.3, while increasing only IAT. The same trend in a retarded ignition is shown as in Figure 3.24, due to lower EOC temperatures. Again, due to the longer ignition delay a higher portion of the fuel is combusted during the premixed combustion as represented by IAT at 353K EOC temperature of 1070K while the shortest ignition delay is simulated at IAT 450K EOC temperature of 1197K.

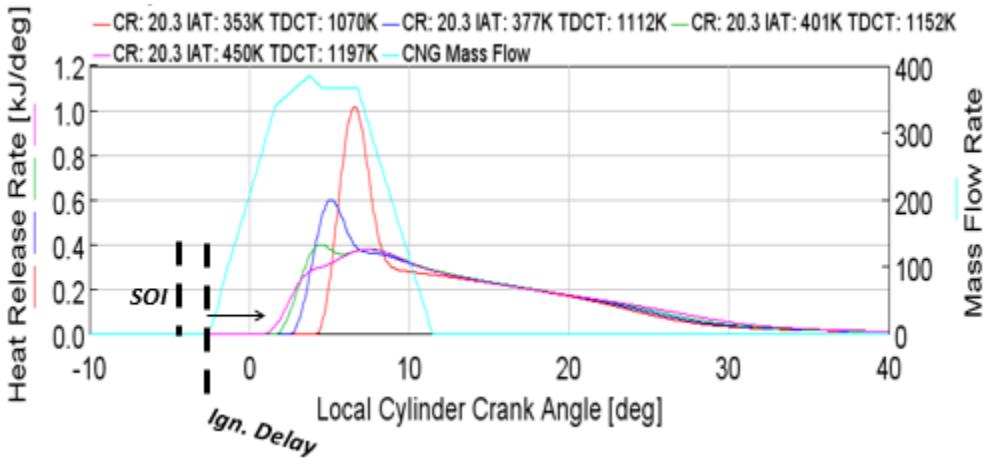

Figure 3.26: Effect of IAT only on AHR Rate (Mode A50) IAT CR 20.3 (128°C)

Figure 3.27 shows the effect of CR and IAT on CA50 for mode A25. As mentioned, mode A25 is 25% load with the shortest injection duration, with a high portion of the combustion taking place in the pre-mixed combustion portion. When running a mostly premixed combustion due to 25% load, the CA50 for engine mode A25 follows the same trend as the ignition delay. If ignition delay is decreased, the CA50 is advanced following the trend in Figure 3.23. If ignition delay is increased, CA50 is retarded showing the two are closely connected for this mode.

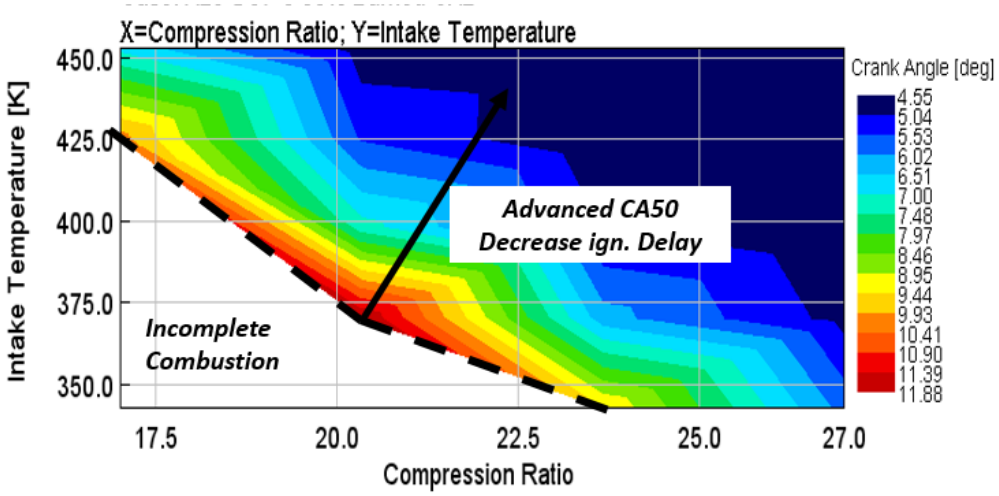

Figure 3.27: Effect of IAT and CR on CA50 Mode A25

Figure 3.28 shows the effect of IAT and CR on CA50 for the 50% load condition A50. This plot shows that only the low EOC Temperature region near the incomplete combustion tracks with ignition delay. The rest of the sweep falls within a 0.5° window for CA50 from 6.95 to 7.4°ATDC. This is due to a longer injection duration and a higher portion of the combustion process is moved toward diffusion combustion compared to mode A25.

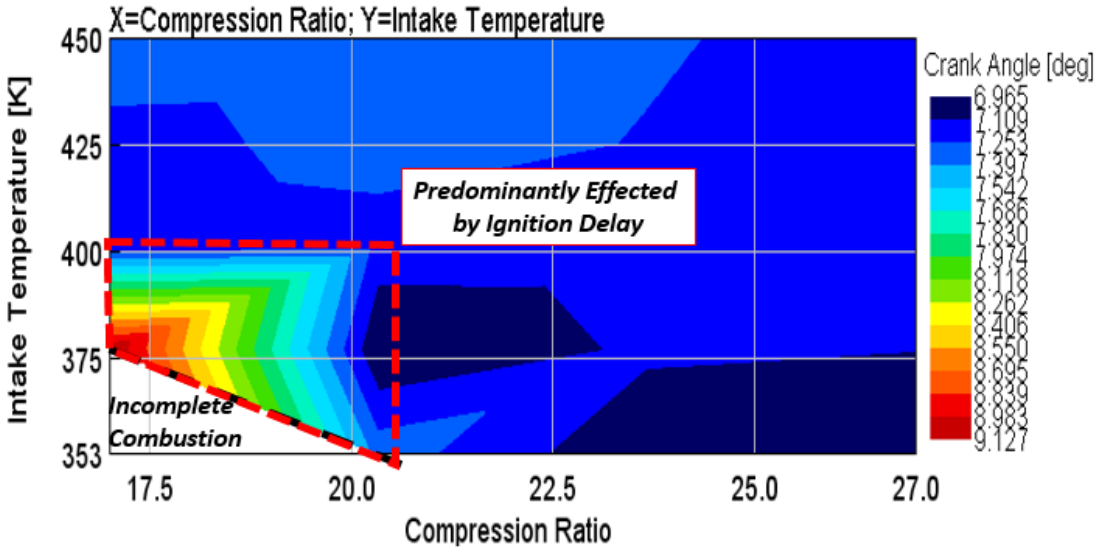

Figure 3.28: Effect of IAT and CR on CA50 Mode A50

Figure 3.29 shows the CA50 contour on a CR vs. IAT for an SOI of -6° ATDC for mode B100. The trend seems to be predominantly affected by CR indicating that the volume within the cylinder plays an effect on the overall CA50 although the relative change of CA50 from min to maximum is only 0.77 crank angle degrees. This case shows the CA50 is not dependent on IAT, except for lower CR's (i.e. 17:1).

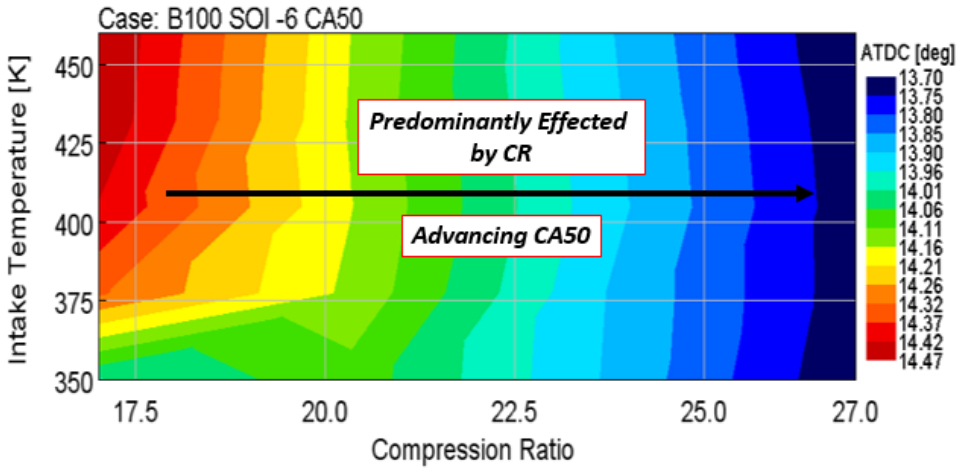

Figure 3.29: Effect of IAT and CR on CA50 Mode B100

Figure 3.30 shows the effect of CR and IAT on the color contour burn duration (CA10°-CA90°) for mode A25. With an increase in EOC temperatures, the burn duration increases as the portion of pre-mixed combustion decreases. For a low-load case with a low EQR and a short injection duration, we see the burn duration is highly affected by both CR and IAT ranging from values of 1.9 CA° to 7.9 CA°. This is important when operating any CR piston during engine operation because very short burn durations can be detrimental to due to the high knock probability.

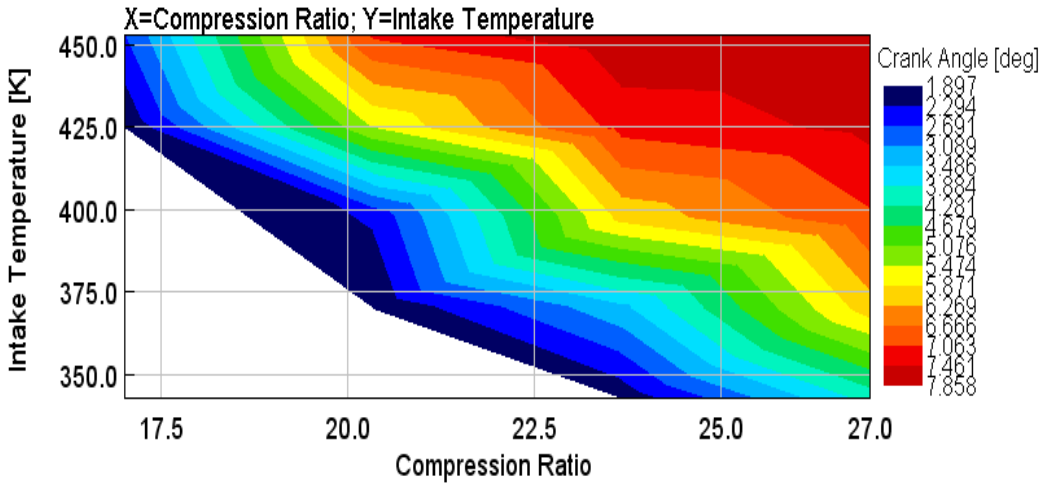

Figure 3.30: Effect of IAT and CR on Burn Duration Mode A25

Figure 3.31 shows the effect of CR and IAT on the color contour burn duration (CA10°-CA90°) for mode A50. This plot shows different trends compared to mode A25 due to more fuel being injected later in the engine cycle indicating more of the combustion process has moved toward diffusion (mixing controlled) combustion. Still, at a low EOC temperature at a low CR and low IAT near the limits of ignition, short burn durations are experienced. At a CR of 17:1 and IAT of 375K, burn duration is 7.4CA°. With an increase in IAT up to 450K, the burn duration is having increased to double of that at 375K. Another observation from Figure 3.31 is that as the CR is increased pass 22.5:1 for

mode A50, there is a very little change in burn duration only varying 3CA° at all IAT simulated.

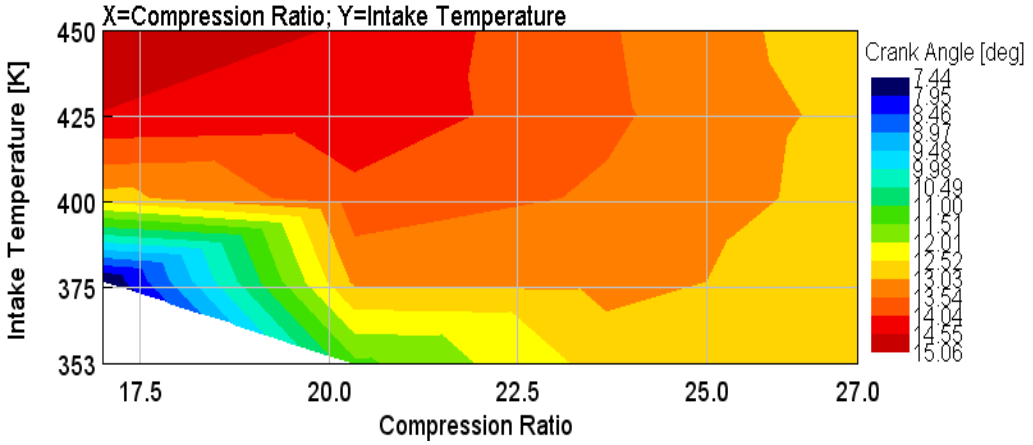

Figure 3.31: Effect of IAT and CR on Burn Duration Mode A50

Figure 3.32 shows the effect of CR and IAT on the color contour burn duration (CA10°-CA90°) for mode B100 SOI -6° ATDC. The first observation is that there is little change to the burn duration with respect to temperature for all CR's simulated. The second observation is that as the CR is increased the burn duration is decreased with the longest burn duration being 37.8 CA° at 17:1 400K IAT, and the shortest being 32.0 CA° at 27:1 and 450K.

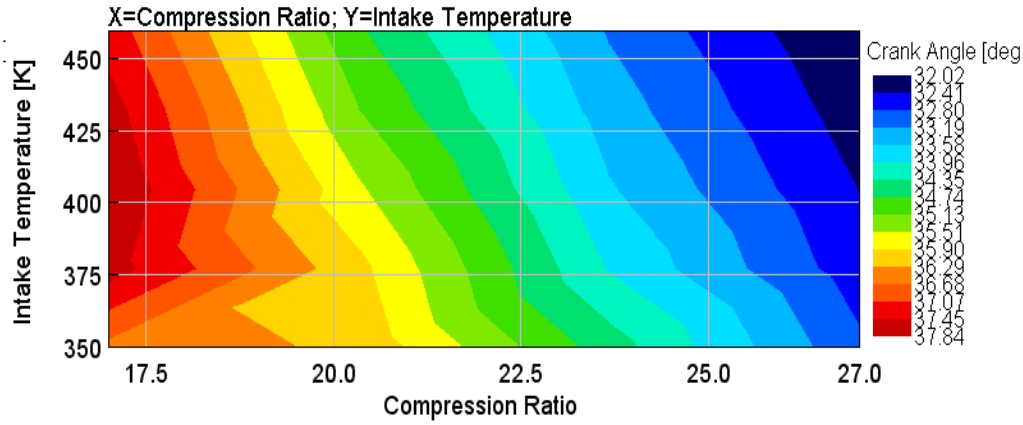

Figure 3.32:Effect of IAT and CR on Burn Duration Mode B100

With the combustion process changes with respect to CR and IAT, other important factors include heat transfer, IMEP, and indicated efficiency for the same sweep. Figure 3.33 shows the contour of heat transfer as a percent of the total fuel on the CR vs. IAT axis. The trends follow the peak motoring temperature curve indicating a higher temperature at TDC prior to firing at the same charge and AFR results in the highest heat transfer at the highest CR and IAT while the lowest is at the lowest IAT and CR. The same trend is present for modes A25 and B100 shown in Appendix A.4.

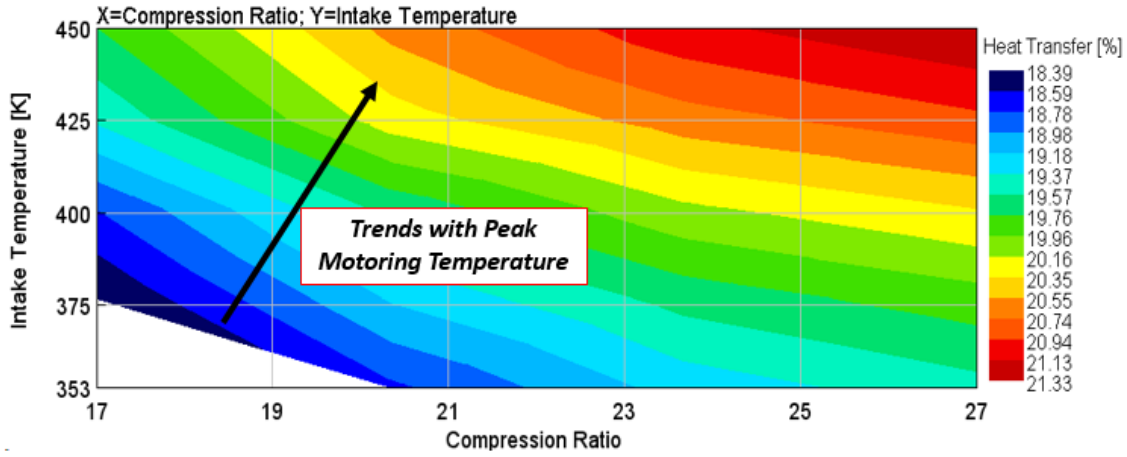

Figure 3.33: Heat Transfer % CR vs. IAT Mode A50

The $IMEP_{GROSS}$ also analyzed on a CR vs. IAT contour for each engine mode. With the plan to run the experimental SCRE on facilities boosted pressure, the $IMEP_{GROSS}$ is an important analysis as the pumping loop will not be controlled by a typical engine driven turbine, but rather an external source. $IMEP_{GROSS}$ calculates only the effective pressure from the compression, and expansion process of the engine rather than including the external driven pumping loop. Figure 3.34 shows the $IMEP_{GROSS}$ on a CR vs. IAT axis. This plot shows that the highest $IMEP_{GROSS}$ comes from the highest CR and the lowest IAT. The reasoning for the increase in $IMEP_{GROSS}$ with a decrease in IAT is due to the decrease in HT. As the HT is increased due to higher temperatures, the $IMEP_{GROSS}$ is expected to decrease. As the plot shows, the $IMEP_{GROSS}$ is the highest at the highest CR, so the goal would be to increase the CR and decrease the required IAT.

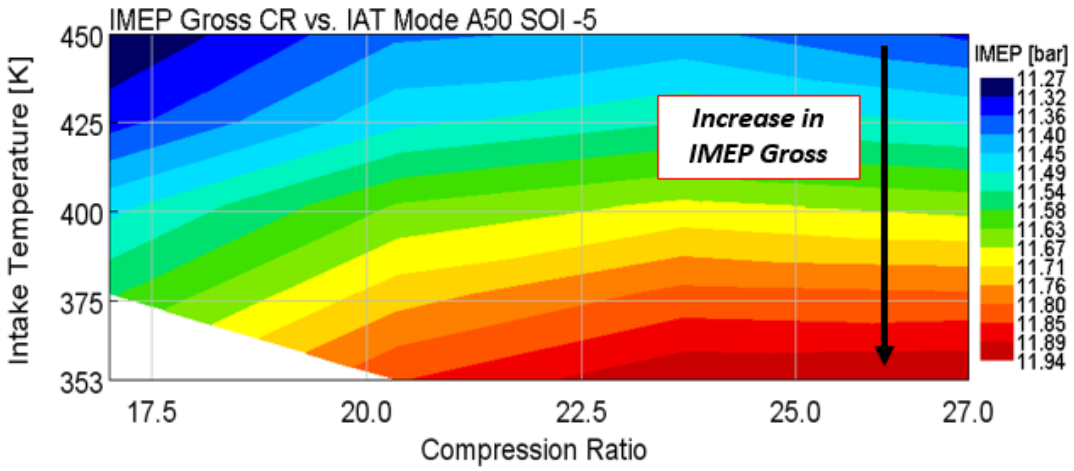

Figure 3.34: IMEP Gross CR vs. IAT Mode A50 SOI -5°ATDC

Looking further into operating ranges of the engine, the peak cylinder pressure is one key metric that must not be exceeded. For understanding the CR limitation on the peak cylinder pressure mode B100 was analyzed, as these should exhibit the highest pressure the engine will see. The peak load was shown to produce pressures up to 179 bar at a CR of 17:1 (OEM). With increasing CR and maintaining the same air charge, the peak cylinder pressure increases. Two lines are shown on the Figure 3.35 at 220 bar and 250 bar. The 220 bar is achievable, and above 250 bar was determined to be detrimental to the engine. This set the peak CR at this specified SOI at a maximum of 25:1 with more realistic CR near 22:1 when operating in mode B100. Peak pressures when operating an engine at CR higher than 25:1 would most likely a later injection strategy to decrease peak pressures.

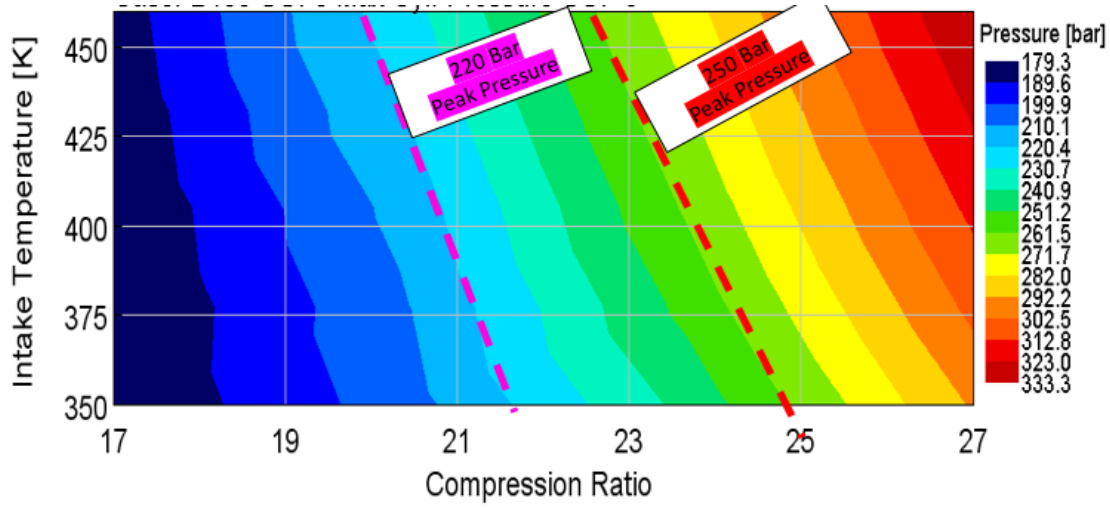

Figure 3.35: Mode B100 Peak Cylinder Pressure CR. vs. IAT.

3.7 Cam Timing Sweep of SCRE

The last study completed using GT-Power 1D modeling software was a sweep of the cam timing within the engine. The goal of the sweep was to determine the benefits of increased valve overlap on internal trapped residuals. With more of the burnt combustion gasses trapped from the prior cycle, the preceding cycle was expected to have higher temperatures at IVC than a low valve overlap situation. The goal of having higher temperatures at IVC is to reduce the amount of heat added from the intake heater, using more of the heat from the exhaust on the previous cycle.

Figure 3.36 shows the OEM valve lift for the exhaust (red) and intake (blue) in solid lines. The OEM camshaft valve configuration has 20° of valve overlap. The intake valve lift was advanced by 2° increments up to a total of 10° advanced while the exhaust valve lift was retarded by 2° increments up to a total of 10° retard. With full advance of the intake and retard of the exhaust, 40° of valve overlap is shown in Figure 3.36 with the dashed blue and red lines, respectively.

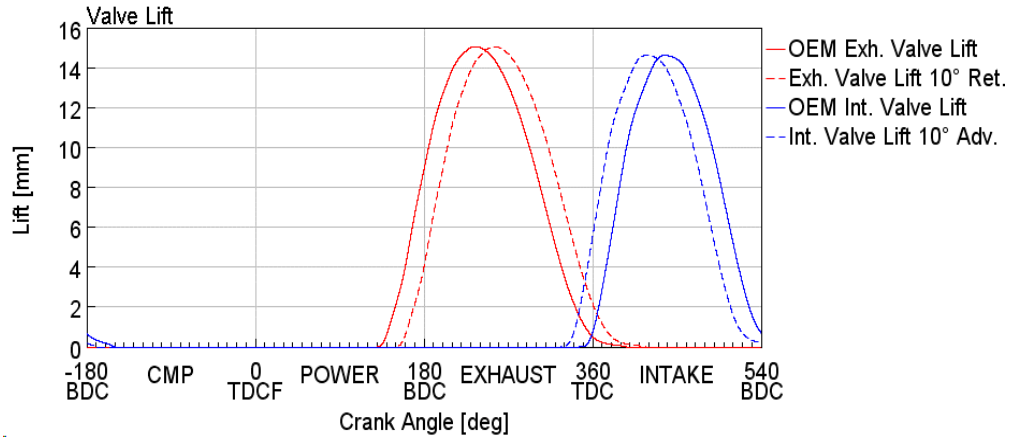

Figure 3.36: ISX SCRE Cam Lift Data

Figure 3.37 shows the list of cases chosen that were re-simulated by Westport for GT-power model validation. Case B (CR 17:1 IAT: 397K) was chosen for the cam timing sweep. This case was chosen because it is the lowest CR which requires the highest IAT to meet a 1.0 ms ignition delay and would benefit the most from higher valve overlap due to increased temperatures at IVC with respect to meeting ignition delay EOC temperatures.

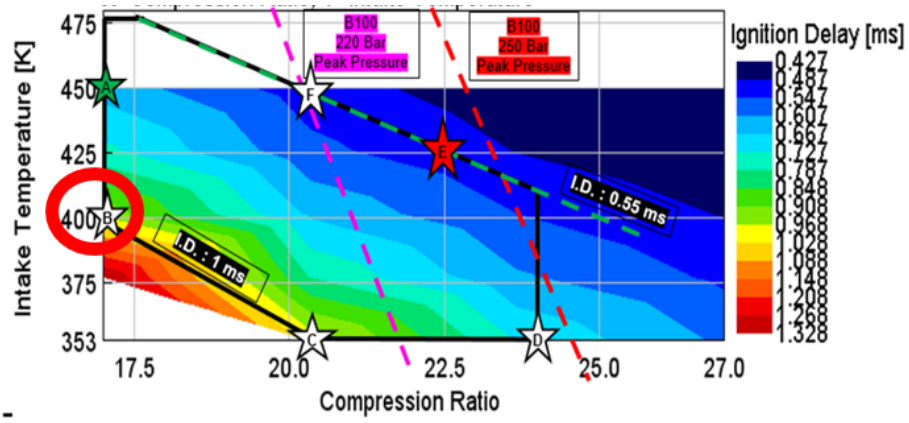

Figure 3.37: Mode and Case Chosen for Cam Timing Sweep

Figure 3.38 shows the total EGR plus residuals trapped for the cam timing sweep completed on an intake cam ret. vs exhaust cam ret. axis. The total residuals are minimum at the minimum valve overlap OEM condition at 7.32% and maximum of 18.86% at the max overlap case of 10° retard from the exhaust and 10° advance for the intake. The dashed line at 4° degrees advance for the intake is due to the current

limitations on the engine due to piston to valve interference which will be discussed in chapter 4.13. Higher valve overlap can be achieved if the valve recessions in the piston are increased in depth. The increase in internal EGR if the cam lobes were adjusted could prove to be an issue due to too much of the exhaust gasses being trapped. To mitigate this, the pressures difference between the intake and exhaust would have to be increased during certain operating conditions.

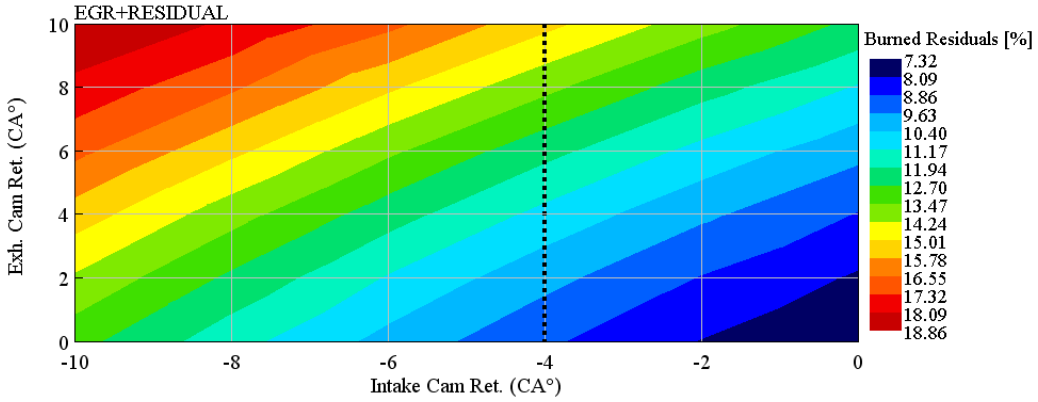

Figure 3.38: Trapped EGR+ Residuals Cam Timing Sweep

Figure 3.39 shows the temperature at IVC on an intake cam vs. exhaust cam timing axis. It should be noted the target temperature in the intake stream was 397K for each of the cases and this was not changed, only the cam timing. The temperature at IVC is minimum for the OEM condition at 430K and maximum at max overlap of 472K due to the higher internal trapped residuals. Even with the current engine limitations a 30K difference from the OEM camshaft could be realized with a new camshaft grind with intake cam advanced 4° and exhaust cam ret. 10°.

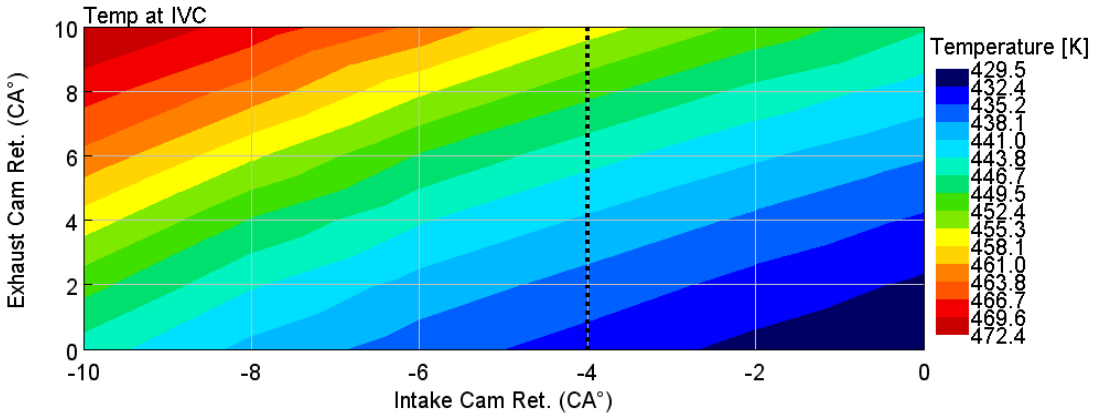

Figure 3.39: Mode A50 CR 17:1 Cam Timing Sweep Temperature at IVC

With higher temperatures at IVC due to increased valve overlap, the temperatures at EOC are also expected to be higher. Figure 3.40 shows the peak motoring temperature for the entire cam timing sweep with the minimum at 1110K which is just above borderline temperature conditions for ignition delay of natural gas (1100K), and a maximum of 1185K with increased valve overlap. The engine limitation optimum would show an increase of 50K at EOC (motoring) due to increased valve overlap using 4° advanced on the intake cam and 10° retard on the exhaust compared to the OEM camshaft overlap. This is important with NG being highly sensitive to temperature below 1100K.

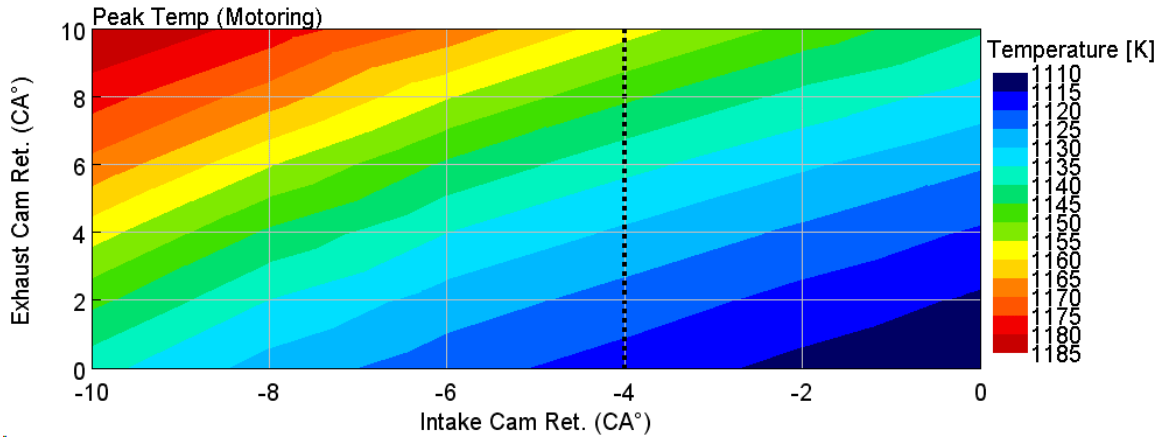

Figure 3.40: Mode A50 CR 17:1 Cam Timing Sweep Peak Motoring Temperatures

With an increase in peak temperatures at TDC due to higher trapped residuals, ignition delays were also expected to decrease. Figure 3.41 shows the ID in ms on a cam timing intake vs. exhaust axis. The minimum ignition delay of 0.61 ms occurs at the highest

valve overlap due to higher temperatures from residuals. The maximum ID simulated was at the OEM valve overlap condition showing approximately 0.90 ms ID. While 0.29 ms ID may not seem like a large change, this could be even more beneficial at low load conditions such as mode A25 where densities are decreased, and conditions are leaner. This is also important because the higher temperatures trapped from residuals could drive down the cost and power required for an intake air heater on within the of a production intent NG DI CI engine.

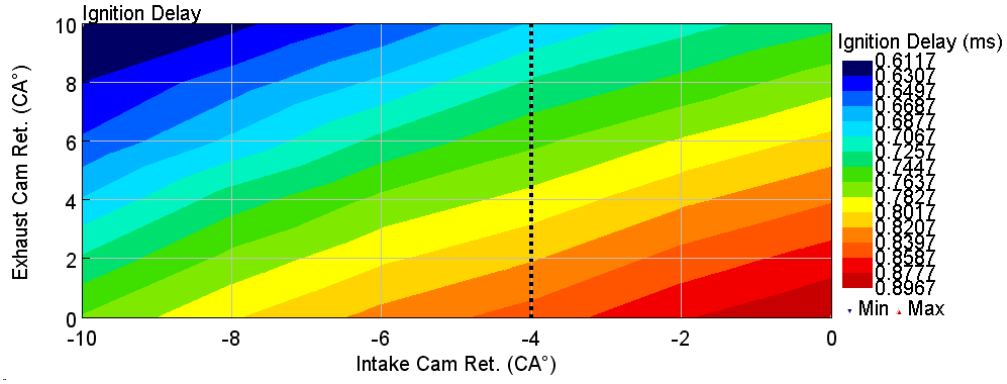

Figure 3.41: Mode A50 CR 17:1 Cam Timing Sweep Ignition Delay

Figure 3:42 shows the ISFC vs. both the intake and exhaust cam phasing. This showed that the optimal case for minimal specific fuel consumption was at the max allowable advance on the intake (4 CA°) and max retard on the exhaust (10 CA°). This reduced the fuel consumption from 191.2 g/kW-hr to 188.6 g/kW-hr. This indicates that with the OEM piston further efficiencies could be achieved by increasing the valve overlap.

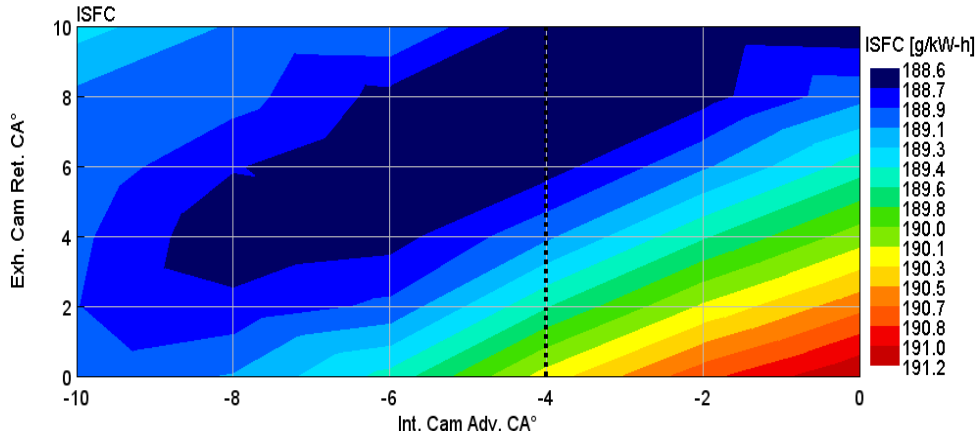

Figure 3.42: Mode A50 CR 17:1 Cam Timing Sweep ISFC

Another method proposed and studied was negative valve overlap, where the intake was advanced (10CA°), and the exhaust was also advanced 10 CA° in 2° increments. Figure 3.43 shows T_{IVC} vs. the intake and cam retard. This plot shows temperatures increased when advancing the intake and decrease when retarding the exhaust. The maximum temperature was observed at the baseline exhaust cam timing and full advance of the intake cam at 10 CA°. This method was determined to be insufficient in adding extra heat to the combustion chamber at IVC, especially considering with the current valve reliefs in the piston only allowing for 4 CA° advance on the intake cam.

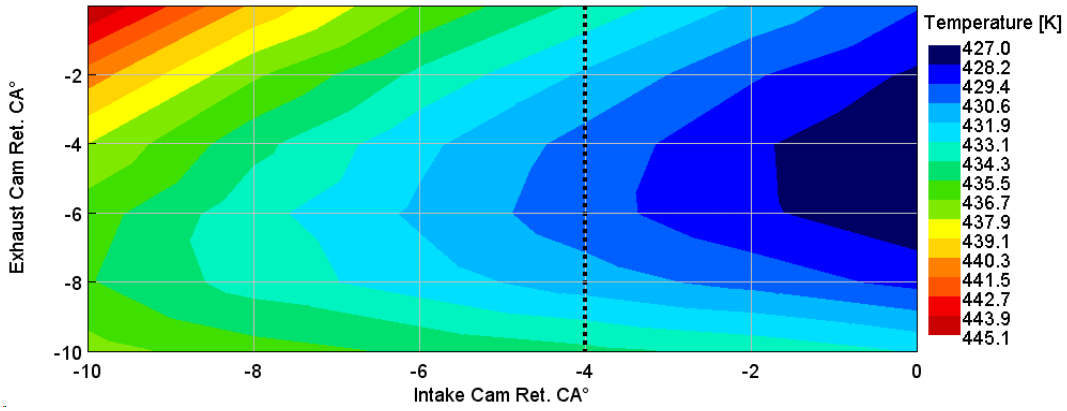

Figure 3.43: Negative Valve Overlap Simulation (T_{IVC}) Intake vs. Cam Ret.

4 Experimental Engine Setup

To achieve cylinder temperatures around 1100-1130K to enable the auto-ignition of natural gas, different concepts can be considered to achieve such high temperatures. Enablers that are known to increase EOC temperature include increased CR, intake air heating, exhaust gas recirculation (EGR) bypass, and thermal barriers. All or some of the enablers could be used to achieve EOC temperatures near 1100-1130K. As mentioned in section 1.2, the objective of the experimental engine setup was to develop and design an operational SCRE with Westport's modified injector to operate using DI CI CNG. The tasks required to achieve an operational SCRE will be discussed within this chapter.

4.1 Procure a 15L ISX engine 2.5L/cylinder

The engine chosen for SCRE operation was a 15L Cummins ISX model:CM871. The inline 6-cylinder features two camshafts, one for intake and exhaust valve actuation, the other for injector actuation. The 2.5L/cylinder engine offered a proven basis for single cylinder experimentation as previous work had been completed by University of British Columbia on a similar setup [6]. The project intent for the SCRE NG DI CI engine was targeted toward MD and HD engine applications. Medium duty passenger vehicles (MDPV) are classified by the EPA with gross vehicle weight ratings (GVWR) from 8,500-10,000 lbs. HD engines fall under multiple categories from light heavy-duty diesel engines (class 2b) to heavy heavy-duty diesel engines (class 8b) with GVWR ranging from 8,500-60,000 lbs across the spectrum. The ISX15 falls under the class 8 truck rating [44]. Table 4.1 gives the information on the engine procured for the SCRE project.

Table 4.1: Procured Engine Information

Procured Engine Information	
Engine:	ISX 435ST
Year:	2008
Truck:	International
CPL:	2732
Rated Power(kW/hp):	324/435
Mileage:	399,747
Serial:	792405
Peak RPM:	2100
Peak Torque (at 1200RPM Nm):	2237
Idle Speed (RPM):	600-800
Dry Weight (lbs/kg):	3021/1370
Oil Capacity (U.S. gallons/liters):	14/53

The specific engine purchased for SCRE operation shown in Figure 4.1 was originally used in a 2008 International truck that had been run on road for nearly 400,000 miles. The procured engine specifications including rated power, mileage, and serial number are found in Table 4.1. The ISX rated power is based upon the calibrations within the engine control module (ECM). This ECM happens to allow the engine to achieve 435 hp, while the total range of the ISX15 in certified in 2007 ranged from 385 hp to 650hp [45]. The total mass of the engine without oil (dry) is 1370 kg with a 53L oil capacity [45].

Figure 4.1: Cummins ISX Purchased for SCRE

The initial procurement was focused on purchasing a running engine with relatively low mileage for minimal impact on the budget. The ISX model chosen was also recommended by Westport due to their prior knowledge of dimensions within the head required for fitment of their injector design.

4.2 Design and Fabricate Engine Cart

The engine cart was designed and built around the specific setup used previously within the APS labs facilities, allowing engines to be moved in and out daily throughout multiple shifts. The difference between the previous carts and the cart specifically for the Cummins ISX was the overall length of the cart. The overall cart dimensions are in Table 4.2. The width between previous carts and the Cummins ISX SCRE cart did not change, but the length increased from 60 inches to 80 inches to allow for engine mounting and the electrical enclosure.

Table 4.2: Cart Dimensions

Engine Cart Dimensions	
Overall Length (inches):	80
Overall Width (inches):	30

4.3 Design and Fabricate Isolators and Mounts

The engine mounts were designed to support the engine from both the front and the rear of the engine. The front mount shown in Figure 0.3 utilized three bolt holes in the engine block for securing the mount to the block. The mounting setup consists of the engine mount, a damper for each side fo the engine between the mount and the barrel, ACME thread and an ACME nut, clamping nuts/bolts and the leveling feet. The barrel is used for a large surface area requirement for the damper as well as for mounting to the ACME adjusting thread. The ACME thread and nut assembly is used to level the engine. The clamping nuts are used to secure the ACME thread as a secondary measure to lock the vertical position of the engine mount once adjusted. The leveling feet connect the adjustable ACME thread to the engine cart using the slot within the engine cart. The slots

in the cart allow for the proper positioning when connecting the engine to the dynamometer. Figure 4.2 shows the engine mounts on the rear utilizing the flywheel housing bolt holes for mounting. The same setup for the adjustment and damping as the front of the engine is located between each of the rear mounts and the cart shown in Figure 4.3.

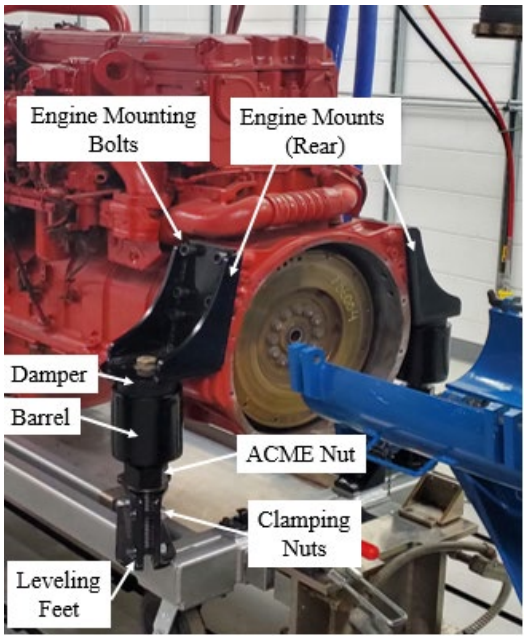

Figure 4.2: Engine Installation & Mounts (Rear)

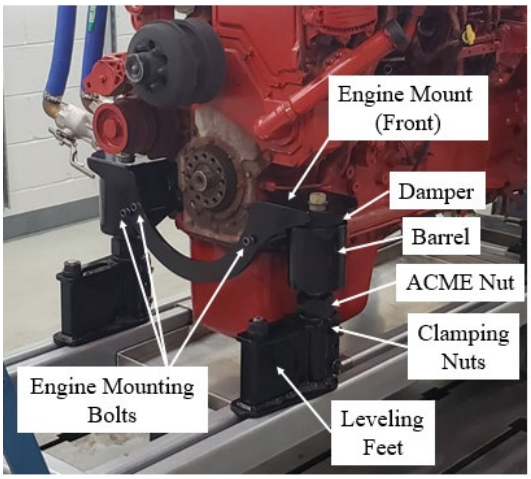

Figure 4.3: Engine Installation & Mounts (Front)

4.4 Install SCRE on Cart

Installing the SCRE on the engine cart was not achievable through the typical engine hoists located within the APS facilities. Instead, the forklift with a boom attachment was used to hoist the engine above the finalized cart with the engine mounts mounted onto the engine. All other parts from the leveling feet up to the damper were attached to the cart. The engine and mounting feet assemblies were maneuvered into alignment and the engine mounts were connected to the mounting feet with the bolts passing through the damper into the barrel. Once the engine was on the cart the vertical and horizontal alignment was completed by adjusting the ACME nuts on each of the four mounting feet.

4.5 Fabricate Engine Interface Panel

The engine interface panel allows for the ISX SCRE cart to be connected to the various inputs and outputs needed to control and run the engine. The interface panel enables connection to multiple different systems required to run the engine properly. The systems the control panel and all connections for can be found in Table 4.3.

Table 4.3: Engine Interface Panel Connection List

Engine Interface Panel		
Engine System	Connection	Purpose
Diesel System	Diesel Pressure In	Controlled Diesel Pressure
	Diesel Out	Return to Tank
	Diesel Temperature	Monitored Temp
	Diesel Control	PWM signal Out
CNG System	CNG In	248 bar CNG from Building
	CNG Out	Vented CNG to Atmosphere
Compressed Air	Pressure Gauge	Calibrate Engine Pressure Gauges
	Air Pressure In	7.6 bar Compressed Air
	Regulated Air Pressure	Control of CNG Booster
Coolant	Coolant In	Cold Coolant Supply
	Coolant Out	Hot Coolant to Heat Exchanger
Combustion Data	Cylinder Pressure	Monitor and Log Cylinder Pressure
	Cylinder Crank Angle	Monitor and Log Crank angle
	Heat Flux	Monitor and Log Heat Flux
System Communication and Engine Monitoring	Thermocouple Out	Monitor Engine Temperatures
	Veristand Control	Control of Various System Parameters
	Veristand Analog Output	Monitor Engine Outputs
	Main Power	Power Sensors and Controllers
	Hour Meter	Monitor Run-Time
	ECM Communication	Control Engine Parameters

Figure 4.4 shows side 1 of the interface panel which contains the connections for the coolant supply and return, as well as the quick connects used for the diesel and CNG fuel. The engine coolant system uses the conventional test-cell cam-lock quick disconnects to allow engine coolant in (cold) and out (hot) to flow from the engine.

The diesel system has connections for high pressure controlled by the diesel standalone cart as well as return plumbing. Side 1 of the interface panel also has a connection for the control signal to the diesel cart as well as a thermocouple connection for monitoring diesel temperature. The interface panel also has connections for CNG in/out of the SCRE

cart. The CNG-IN quick connect is rated to 345 bar and uses the CNG male quick connect established within the heavy-duty test cell. The CNG out is a low-pressure vent system which connects to the building exhaust to vent CNG as pressures within the diesel fuel system decrease.

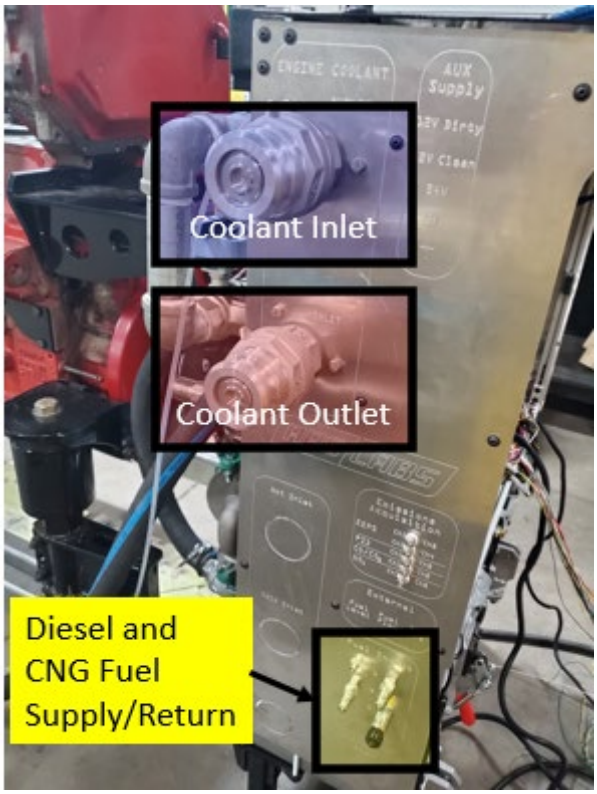

Figure 4.4: Engine Interface Panel (Side 1)

Figure 4.5 shows side 2 of the interface panel which includes the connections for control from Veristand and the ECM as well as power required to operate various sensors and actuators. Side 2 of the interface panel encompasses two connections for building compressed air and regulated compressed air. The regulated compressed air connection will be used to control the booster, while the building compressed air can be used to calibrate the various gauges on engine cart. The engine cart also houses a regulator and pressure gauge to quickly calibrate any sensor with building shop air up to 7.6 bar (110 PSI.).

The communications and monitoring of various sensors and actuators are also completed through the interface panel side 2 on the SCRE cart. All temperatures monitored through Veristand are connected through the interface panel. The main power to the cart including 5V, 12V clean, 12V dirty, and 24V power are fed to the cart through the interface panel electrical connections. The Analog Output connections are wired to the electrical signals output of the interface panel, enabling the measuring and logging of many transducers. The system communication portion also allows for control of various sensors such as the coolant valve, engine speed, and CNG solenoid valve. The interface panel also has an hour meter which will count when the oil pressure is above the low-oil pressure threshold which will occur as soon as the engine begins motoring. The interface panel encompasses a KVASER USB to CAN Bus interface connector enabling the control of fuel pressure, fuel timing, and other engine control functions.

The interface panel side 2 also allows for the connection of various BNC outputs to be monitored in CAS and logged at high speed. The interface panel enables the connection to the test cell's combustion analysis system (CAS Redline) recording cylinder pressure and crank angle resolved engine position.

Figure 4.5: Engine Interface Panel (Side 2)

4.6 Driveshaft and Flywheel

4.6.1 Driveshaft Adaptation

The engine flywheel dimensions were obtained, and an engine adapter plate was manufactured to fit the drive shaft bolt pattern while also mating to the flywheel bolt pattern. The ISX adapter plate machined to a 0.75-inch-thickness. The outer diameter was designed to have minimal clearance with the flywheel to ensure the flywheel adapter was centered on the flywheel. The drive shaft is centered on the flywheel adapter with a slight clearance fit of the internal bore at a dimension of 3.76 inches. Figure 4.6 shows the CAD drawing of the ISX Flywheel Adapter plate. Figure 4.7 shows the driveshaft flywheel setup with the AC dynamometer. The engine was leveled to 0° while allowing a 2° decline on the drive shaft from the engine to the AC dyno.

This driveshaft and flywheel assembly is required to test the SCRE using the AC dynamometer. Without connection to the dyno, no load could be added to the engine. This was essential for testing of the engine.

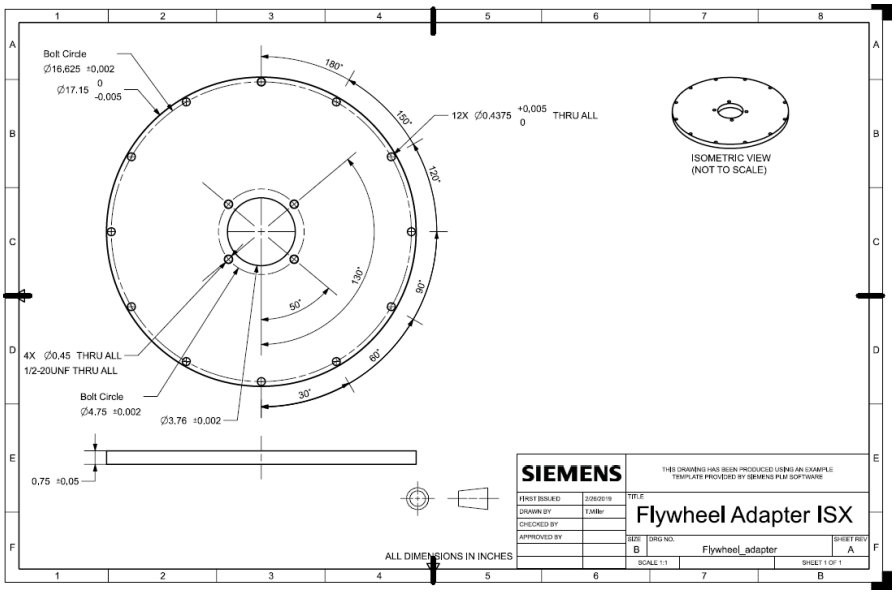

Figure 4.6: ISX Flywheel Adapter

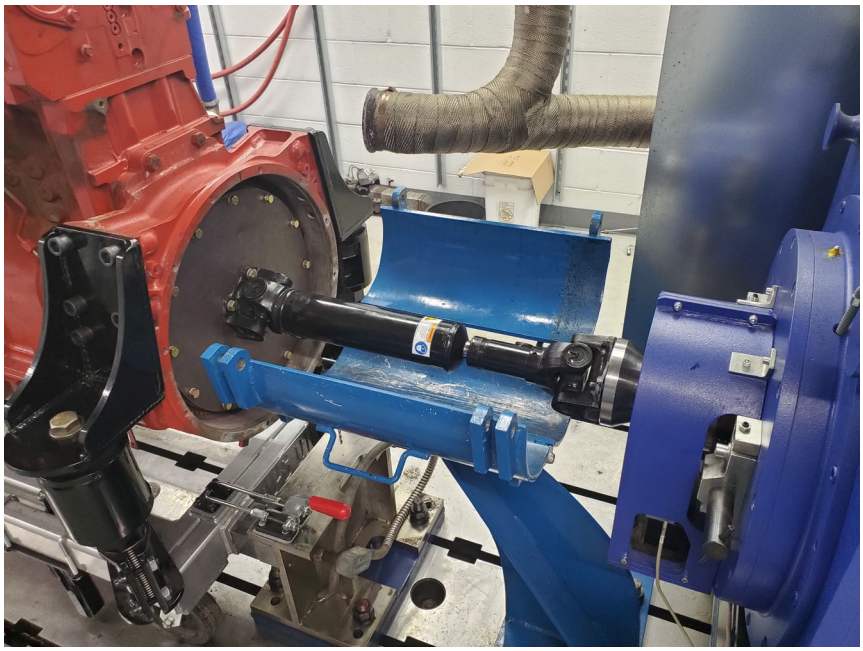

Figure 4.7: ISX Driveshaft Setup

4.6.2 Driveshaft Testing

Selecting the proper driveshaft was necessary when operating a SCRE. Without knowing all the specifications on the engine inertia, testing was required to determine the natural frequency of the system. When operating the SCRE it was important to understand the natural frequency to determine if a dual-mass flywheel was required for operation, or if the current driveshafts used at the APS facility for diesel engine testing would be adequate.

With the engine and driveshaft aligned the ISX SCRE was motored using the AC dynamometer. There were two driveshafts that were tested to determine first, the engine inertia, as well as the natural frequency of each system. The driveshafts that were tested included two driveshafts procured from Machine Service Inc. for prior projects. The first driveshaft tested was a solid driveshaft with no internal dampers within the system. The stiffness of the solid driveshaft was specified by the manufacturer at 64,700 Nm/rad. The engine was motored multiple times from 0-2000 RPM at constant acceleration of 100 RPM/second. and 200RPM/second. Figure 4.6 shows the ramp of the engine speed from

0 RPM to 2000 RPM at a constant 100 RPM/second acceleration, a hold a 2000 RPM and a deceleration coast down of the engine.

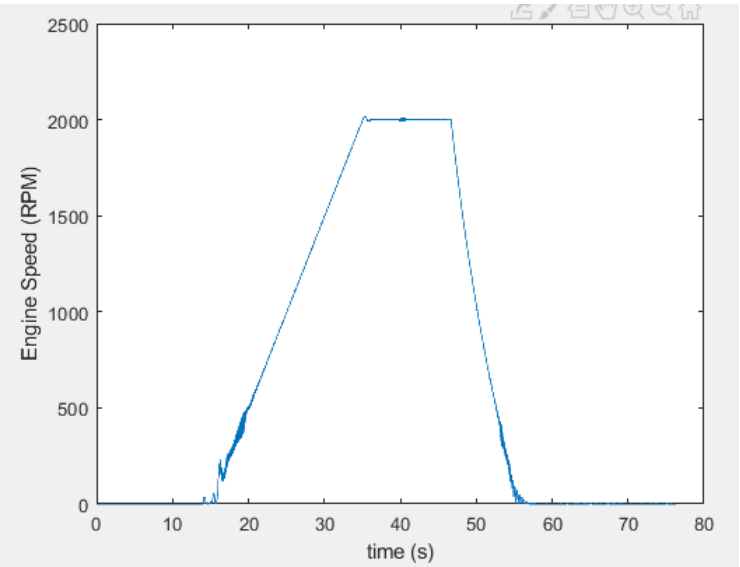

Figure 4.8: Engine Speed Ramp (100 RPM/Second)

While monitoring the engine speed during engine acceleration and deceleration, the inline torque monitor was also measured at a sample rate of 400 Hz. With the torque monitored, it was possible to observe the natural frequency of the system.

The first method of calculating the inertia of the engine was through the torque measurements during the ramp tests completed. According to newton's second law, torque is equal to inertia multiplied by angular acceleration. A calculation was completed taking first, the required torque to motor the engine at constant speeds of 1000 RPM and 1500 RPM. The measured torques observed for 1000 RPM and 1500RPM were -272 and -312 NM respectively during the constant speed motoring tests. The negative torque is due to the torque being applied to the engine rather than the engine applying the torque to the dynamometer.

The measured torque for three different ramps is shown in Figure 4.9. Two of the tests shown are at 100 RPM/second acceleration (10.47 rad/s^2) and one of the tests was completed at 200 RPM/second acceleration (20.94 rad/s^2). With the obtained data, it was

possible attempt the calculation of inertia by taking an average value of torque around the 1000 and 1500 RPM points during the sweep (+/- 70 ms), and subtracting the torque required to motor the engine at a constant velocity. This torque to accelerate was assumed to be the torque measured during the ramp minus the torque at the constant velocity given by equation 4.1. With the torque required to accelerate the engine, the inertia was assumed to be the calculated by equation 4.2.

$$Torque_{Accel} = Torque_{Ramp} - Torque_{Constant\ Velocity} \quad 4.1$$

$$Inertia_{eng} = \frac{Torque_{Accel}}{\alpha} \quad 4.2$$

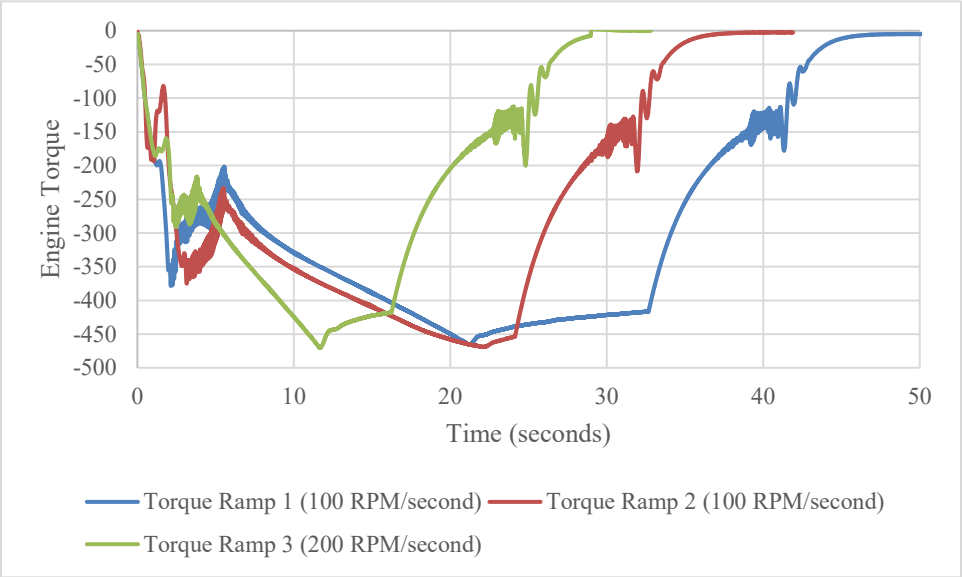

Figure 4.9: Measured Torque vs. Time (Ramp Tests)

With the calculations completed the results for the calculated inertias for each of the three ramps at both 1000 RPM and 1500 RPM are given in Table 4.5. The results show that for ramps one and two, inertias ranged from 8.3 to 11.8 kg-m^2 while ramping at 100 RPM/second. When the acceleration was increased to 200 RPM/second, you would expect the measured torque value to increase during the acceleration period due to inertia of the engine being a constant value. Figure 4.9 however shows the green line for ramp three (200RPM/second) torque values remained nearly the same during the ramp period compared to ramps one and two. Due to the torque remaining nearly the same during the

measurement period of acceleration, the inertia is decreased to 6.1 and 4.8 kg-m^2 at the engine speeds of 1000 and 1500 RPM respectively shown in Table 4.4. This method of calculating the engine inertia was deemed to be unsuccessful because of the torque measurements remaining the same for different ramp rates (angular accelerations) of the engine. You would expect the torque values to increase by the same factor of acceleration increase using equation 4.3 which was not the case. The hypothesis on the measured torque not increasing with an increased angular acceleration is most likely due to the acceleration rates not being large enough to determine the effect of inertia from the torque values measured. Possibly a 400 or 500 RPM/second ramp rate would have increased the measured torque values.

Table 4.4: Method 1 Calculating Inertia

	Ramp 1			Ramp 2			Ramp 3		
Engine Speed (RPM)	$Torque_{Accel}$ (Nm)	α (rad/s^2)	$Inertia_{eng}$ (kg-m^2)	$Torque_{Accel}$ (Nm)	α (rad/s^2)	$Inertia_{eng}$ (kg-m^2)	$Torque_{Accel}$ (Nm)	α (rad/s^2)	$Inertia_{eng}$ (kg-m^2)
1000 RPM	-104.7	10.4	10.0	-121.5	10.3	11.8	-122.7	20.2	6.1
1500 RPM	-86.8	10.4	8.3	-109.0	10.3	10.6	-96.0	20.2	4.8

The second method of calculating engine inertia was by creating a spectrogram plot of the torque vs. time. Figure 4.10 and Figure 4.11 show the spectrogram of the torque measurements and the linear frequency that appears throughout the ramp up and down of engine speed. The natural frequency of the solid driveshaft between the engine and dynamometer was observed to be between 20 and 22 Hz for both 100 and 200 RPM/second ramp rates in Figure 4.10 and Figure 4.11 respectively. The linear line shown on the spectrogram indicates the first order natural frequency of the system. With the solid driveshaft the natural frequency occurred between 20 and 22 Hz. for both 100 and 200 RPM/second ramp tests.

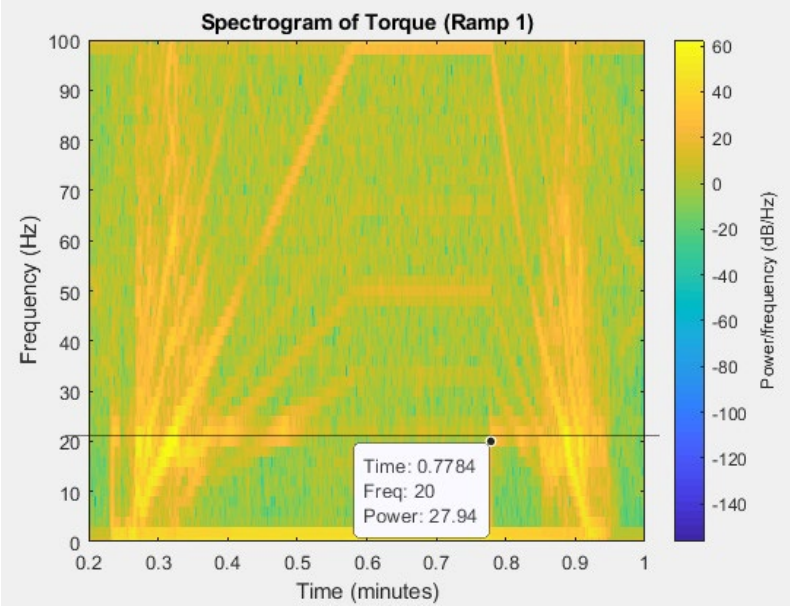

Figure 4.10: Ramp 1 (100RPM/Second)

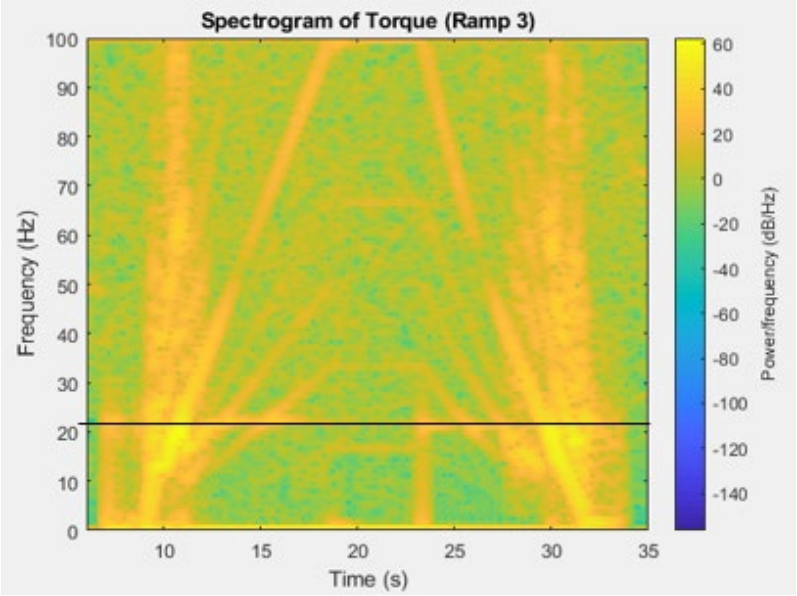

Figure 4.11: Ramp 3 (200RPM/Second)

With the solid drive shaft tested and a natural frequency of the entire engine, driveshaft, and dynamometer system was determined to be at 21 Hz. The two-piece drive shaft was then substituted. Ramp 4 with the two-piece driveshaft was predicted to decrease the natural frequency of the system with a less stiff shaft coupling the engine and the dyno. Equation 4.3 shows the natural frequency equation calculated from the dyno inertia (J_{dyn}),

engine inertia (J_{eng}), and torsional stiffness (C_T) of the coupler [45]. With a decrease in torsional stiffness (C_T), the natural frequency F_R will also decrease.

$$F_R = \frac{1}{2\pi}\sqrt{\left(\frac{1}{J_{dyn}} + \frac{1}{Jeng}\right) * C_T} \qquad 4.3$$

Figure 4.12 shows the spectrogram of the measured torque for the two-piece (i.e., less-stiff) driveshaft. As expected, the natural frequency of the engine dyno system had decreased from 21 Hz. down to 8 Hz. The engine operating range according to the OEM (Cummins) is 800-2100 RPM. The importance of the driveshaft selection was to keep the first-order natural frequency of the system out of the operating range of the engine. The 21 Hz. first-order natural frequency correlates to 1260 RPM which lies within the engine operating range. The two-piece driveshaft first-order natural frequency of 8 Hz. correlates to 480RPM, which lies below the engines operating range. The engine inertia was found online to be either 4.5 or 8.1 kg-m^2 dependent on the flywheel the ISX or QSX is supplied with [46]. The spectrogram plots confirm the engine inertia is 8.1 kg-m^2.

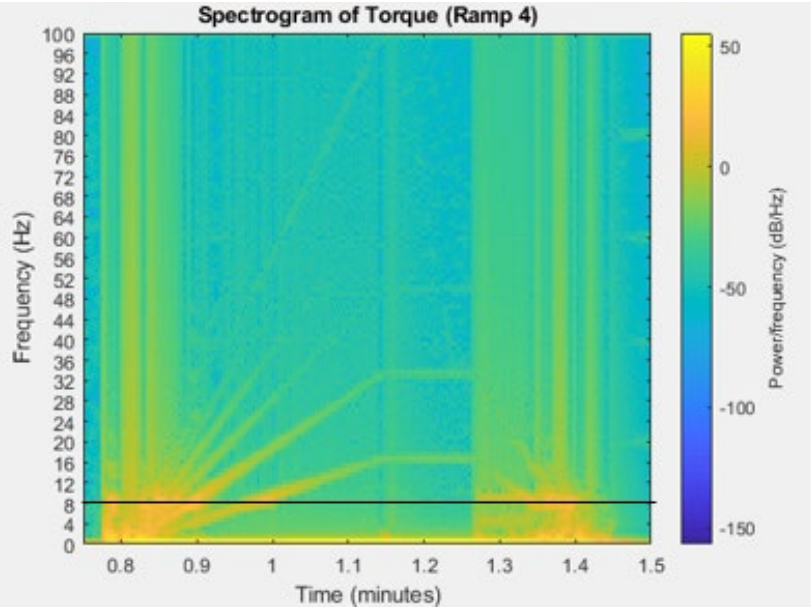

Figure 4.12: Ramp 4 (100RPM/Second Two-Piece Drive Shaft)

The schneider electric power drive dynamometer within the MTU APS heavy-duty test cell has an inertia of 6.47 kg-m^2. The parameters for the engine inertia, dyno inertia, driveshaft

torsional stiffnesses, and the natural frequencies for each system are given in Table 4.5. The two-piece driveshaft will be used for initial testing due to the decreased natural frequency of the system from the lower torsional stiffness. This driveshaft will allow for the engine to pass through the first-order natural frequency only when ramping the engine to its operating range (800-2100 RPM).

Table 4.5: Natural Frequency of SCRE and Dynamometer Parameters

Engine Inertia kg-m^2	8.1
Dyno Inertia kg-m^2	6.7
Two-Piece Driveshaft Stiffness (Nm/rad)	64736
Solid Driveshaft Stiffness (Nm/rad)	8631
Two-Piece Driveshaft Natural Frequency (Hz.)	8
Solid Driveshaft Natural Frequency (Hz.)	21
Two-Piece Driveshaft Natural Frequency First Order (RPM)	480
Solid Driveshaft Natural Frequency First Order (RPM)	1260

The less stiff two-piece driveshaft was also tested to ensure the torsional stiffness values given by the supplier measured were as expected. A linear displacement of one of the flywheel bolts measured to calculate a rotational movement of the driveshaft as the engine was torqued from the front side of the engine. The flywheel adapter bolt was used to calculate the rotational displacement in radians because the bolt circle diameter of the adapter plate is a known value of 16.625 inches. Figure 4.13 shows a photo of the linear displacement measurement setup used to calculate rotational displacement of the flywheel during the testing.

Figure 4.13: Linear Displacement of Flywheel Bolt

With the dynamometer locked down, a constant torque was applied to the engine, while measuring the linear displacement of a flywheel bolt. The various torques were applied and measured with the in-line torque meter. The test was repeated 8 times for a total of 9 tests. Figure 4.14 shows the results from the torsional stiffness testing completed for the two-piece driveshaft as well as the manufacturers specification. It was determined that the value reported by the manufacturer was slightly higher than the measured values, possibly due to wear within the damper during prior engine testing.

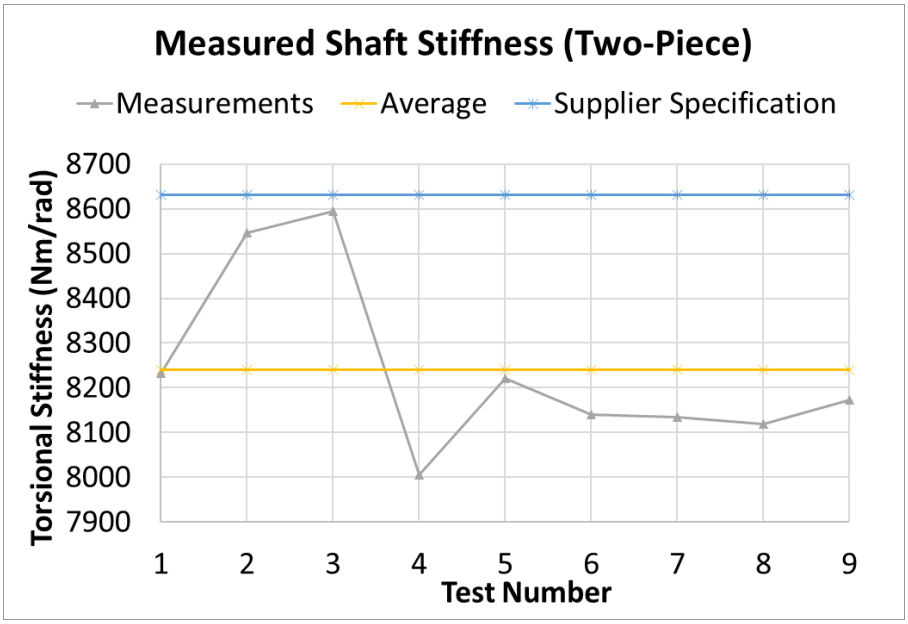

Figure 4.14: Measured Torsional Stiffness

4.7 Design and Fabricate Intake, Exhaust, and EGR system

With deleting five of the six cylinders, the SCRE displacement was reduced from 15 to 2.5L. The stock intake and cooled EGR system were removed from the ISX engine. The SCRE intake, exhaust, and EGR system were designed with a few requirements in mind, temperature, pressure, corrosion, and flow. It was also important to protect the system in the occurrence of a backfire within the engine. Figure 4.15 shows the intake, exhaust, and EGR schematic for the SCRE. The figure also shows placements of specific measurements to be sampled.

The intake air will flow through the intake heater, through the surge tank, and into the cast intake manifold located within the OEM ISX cylinder head. The air will only enter cylinder six closest to the dynamometer. Cylinder six was chosen to reduce the effect of crankshaft twist during operation. Pressure and temperature will be monitored in the intake surge tank. MAP, IAT, and CO_2 measurements will be sampled post intake surge tank prior to the cylinder head intake manifold.

Within the combustion chamber crank angle resolved pressure and heat flux will be measured. The exhaust manifold pressure and temperature will be monitored directly from the cylinder six exhaust port. The pressure and temperature within the exhaust surge tank will also be measured. Pressure, temperature, and CO_2 will be measured within the EGR loop prior to the EGR valve where exhaust gasses can re-enter the intake stream. Exhaust gas emissions will be monitored directly after the exhaust back pressure valve including an O_2 sensor, NO_x sensor, and a bung for the Horiba 5-gas analyzer.

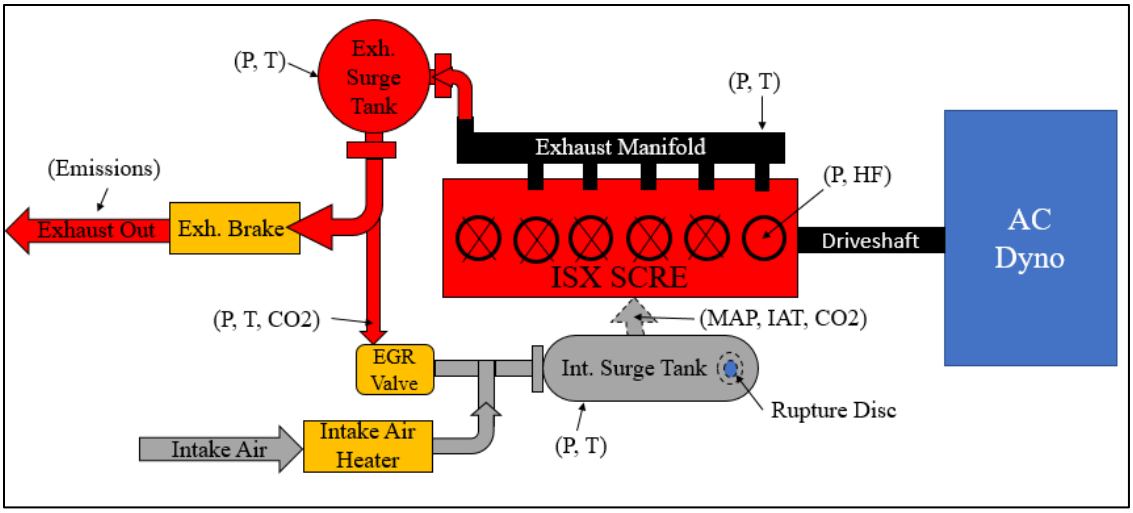

Figure 4.15: SCRE Intake, Exhaust, EGR Schematic

4.7.1 Intake System Design and Fabrication

The intake system shown in Figure 4.15 is colored grey. The pipe used for designing the intake system is 2" schedule (sch.) 40 304L stainless steel (SS). The ratings for 2" schedule 40 304L SS at 300°C are 4.8 MPa [48]. This working pressure is well above what the boost pressure will be, and greater than the pressure expected if a backfire were to occur in the intake stream. The intake air will either be boosted or (NA) dependent on the boost pressure applied upstream of the check valve above the test cell. The intake air will pass through the intake air heater which is then directed into a seamless 304L SS T-fitting. The T-fitting allows for the flow of both heated intake air and uncooled exhaust gas. The intake air or air/EGR mixture then flows into the surge tank and out of the bottom of the surge tank. Below the surge tank is another T-fitting used to incorporate a rupture disc. The intake air then flows from the T-fitting below the surge tank into the SCRE intake manifold casted into the head.

Figure 4.14 shows the SCRE intake flow path assembled on the engine. Also noted in Figure 4.14 is the 600# RFWN ANSI flanges. The size of the flanges for the intake system were all either 304L or 316L 600# flanges. The pressure ratings for 316L SS 600# ANSI flanges at 350°C are 5000 kPa [49]. Between each ANSI flange assembly is a high

temperature 304 SS gasket rated to 4137 kPa (600 PSI) at a maximum temperature of 449°C (840°F).

The intake surge sizing was based upon the observed sweeps in GT-power. As the intake surge tank size was increased, the mass flow measurement fluctuations upstream of the surge tank decreased as shown in Figure 3.8. Also, referring to Figure 3.7, the EGR pressure drop fluctuation decreases as both surge tanks are increased. The smallest fluctuation coming from intake and exhaust surge tanks being 212L. Figure 3.7 shows that while there is a difference when adding volume to both tanks, there was minimal difference between 48 and 125L. With the optimal tank regarding steady state engine testing being the largest tanks, other factors including cost and packaging on the engine cart had to be considered. The final decisions on SCRE tank sizing included that 212L for each tank was too large to mount to the engine cart. Minimal gains were observed from 48L to 125L tank size increase, but noticeable differences were observed when increasing from 24L to 48L. The size chosen after the GT-power sweep was near 48L.

The procurement of the intake surge tank was dictated by the sizing, and material specifications, and predicted pressure and flow performance. Like the other intake components, SS was chosen as the material for its corrosion resistance and strength properties. The surge tank strength was set at a pressure of 48 bar (700 PSI) with at a temperature of 482C (900 F). 48 bar allows for a peak of pressure ratio of 16:1 from the expected boost pressures if a backfire were to occur.

The surge tank size chosen was limited by manufacturability was sized at 41L (10.8 gal) 7L shy of the 48L surge tank Gt-power model. Figure 4.16 shows the isometric view of the intake surge tank with the 600# ANSI flanges with each of the parts located in the bill of materials (BOM) for the surge tank. The BOM for the intake surge tank is shown in Table 4.6. The shell of the surge tank was made from Sch. 40 316SS and connected to the two ends of the tank by a 3/16-inch weld backing ring as shown in Figure 4.16. The surge tank was also designed with a 1/4-inch-thick bracket to allow for a flat face mounting

surface. The surge tank was hydrotested to 1180PSI at atmospheric temperature to test the welded surge tank strength.

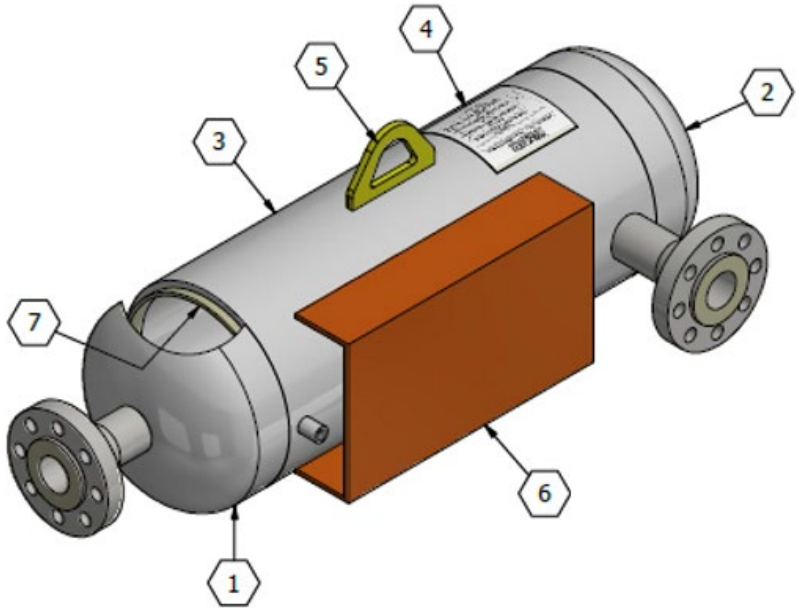

Figure 4.16: Intake Surge Tank Isometric View

Table 4.6: Intake Surge Tank BOM

BILL OF MATERIAL			
ITEM	QTY	DESCRIPTION	MATERIAL
1	1	LEFT HEAD: ø10 3/4" OD x 3/8" NOM. (0.328" MIN) x 2:1 ELLIPS.	SA-240-316
2	1	RIGHT HEAD: ø10 3/4" OD x 3/8" NOM. (0.328" MIN) x 2:1 ELLIPS.	SA-240-316
3	1	HORIZONTAL SHELL: 10" SCH.40 PIPE (0.365" NOM, 0.319" MIN WALL) x 24" LONG	SA-312-316
4	1	ASME DATA LABEL: ROLLED TO FIT HORIZONTAL SHELL	SA-240-304
5	1	LIFT LUG: SMALL 3/8" THK.	SA-240-316
6	1	BRACKET: 1/4" THK. x 9" WIDE x 16" LONG	SA-240-316
7	2	WELD BACKING RING: 3/16" THK x 1" WIDE, FOR ø10" SCH.40 PIPE	SA-240-316

The rupture disc location in Figure 4.17 was placed strategically to insure if a backfire took place in the intake surge tank the high pressure would be directed downwards. The rupture disc specifications were to ensure the disc ruptured at 1034 kPa (150 PSI) at a maximum temperature of 204°C (400F). The max temperature requirement for intake air at the lowest CR (17:1) was approximately 450K (177°C) to achieve an ignition delay of

approximately 1ms. 204°C was set as the approximate maximum temperature in the intake manifold required to achieve auto-ignition with the lowest CR. The rupture disc pressure rating was based upon the maximum boost pressure required at the lowest CR for the highest load which was only 400 kPa. This is under half of what the rupture disc is rated for. The rupture disc should only open under a backfire, not under any steady state conditions. The rupture discs (PCR02-137), and rupture disc holder (P3AA11-F00-19000100) were purchased from Oseco based upon the temperature and pressure specifications given.

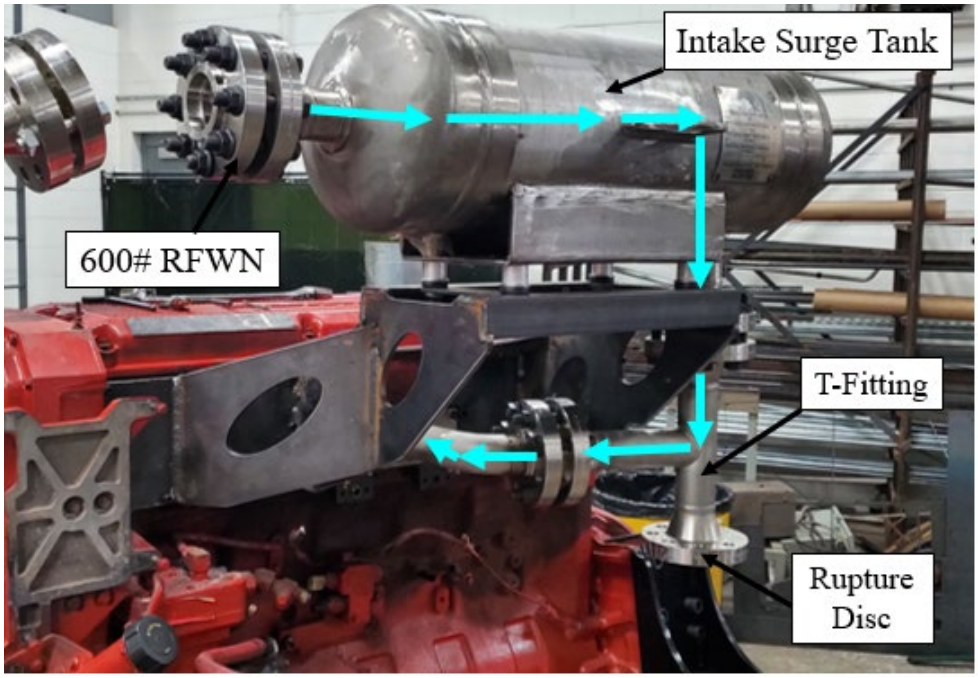

Figure 4.17: SCRE Intake Flow Path

4.7.2 Design and Fabricate Exhaust System

Figure 4.18 shows the exhaust manifold and exhaust flow path into the exhaust surge tank. The exhaust system design first incorporates the OEM 15L exhaust manifold. The flow enters the exhaust manifold from the sixth cylinder flowing through the entire manifold before entering two 90° turns into the exhaust surge tank. The use of the exhaust manifold utilized to increase the volume in the exhaust stream before entering the EGR valve. The first cylinder exhaust flange was rotated 180° to allow for a flange

surface to be coupled to 90° 2-inch Sch. 80 SS pipe heading into the exhaust surge tank. The ANSI flanges used to couple to the exhaust surge tank were 900# flanges to handle the required pressures of a backfire at the expected exhaust gas temperatures flowing through the exhaust system. The turbo outlet on the exhaust manifold will be blocked off with a plate and the OEM turbo gasket.

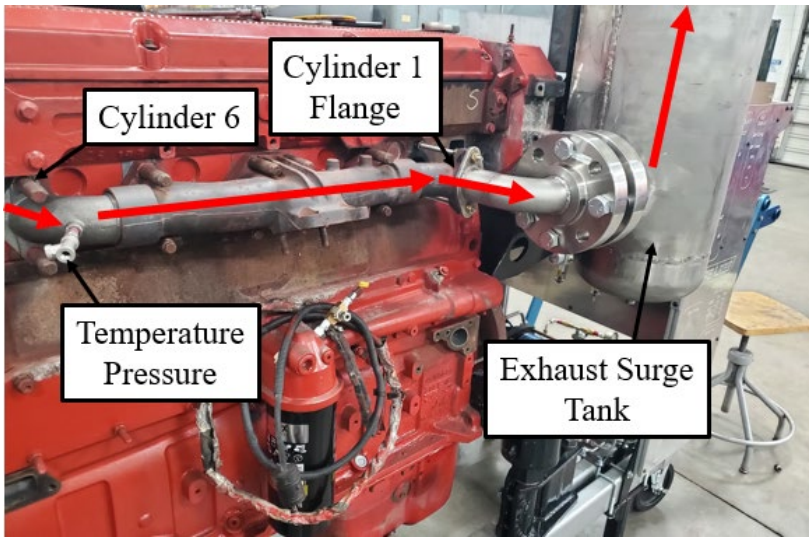

Figure 4.18: Exhaust Manifold Setup

The exhaust surge tank size was chosen to be 41L to maintain the same volume as the intake surge tank but was designed to handle the higher temperatures. Due to much higher temperatures being present from EGT's, the surge tank was manufactured with heavier ANSI flanges and Sch 80 SS material. The exhaust surge tank isometric view along with the BOM are in Figure 4.19 and Table 4.7 respectively.

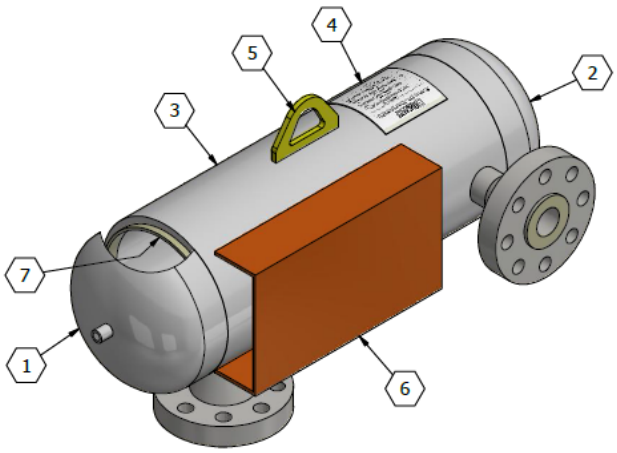

Figure 4.19: Exhaust Surge Tank Isometric View

Table 4.7: Exhaust Surge Tank BOM

BILL OF MATERIAL			
ITEM	QTY	DESCRIPTION	MATERIAL
1	1	LEFT HEAD: ø10 3/4" OD x 1/2" NOM. (0.340" MIN) x 2:1 ELLIPS.	SA-240-316H
2	1	RIGHT HEAD: ø10 3/4" OD x 1/2" NOM. (0.340" MIN) x 2:1 ELLIPS.	SA-240-316H
3	1	HORIZONTAL SHELL: 10" SCH.80S PIPE (0.500" NOM, 0.438" MIN WALL) x 24" LONG	SA-312-316H
4	1	ASME DATA LABEL: ROLLED TO FIT HORIZONTAL SHELL	SA-240-304
5	1	LIFT LUG: SMALL 3/8" THK.	SA-240-316
6	1	BRACKET: 1/4" THK. x 9" WIDE x 16" LONG	SA-240-316
7	2	WELD BACKING RING: 3/16" THK x 1" WIDE, FOR ø10" SCH.80S PIPE	SA-240-316H

After the 41L exhaust surge tank, the exhaust stream is feeds into a 2” T-fitting coupled by 900# ANSI flanges. The exhaust T-fitting allows flow either through the brake valve and out of the test cell, or into the EGR loop and into the intake stream. The butterfly type brake valve is put in the exhaust stream for the controlling the back pressure of the exhaust system. The back pressure within the exhaust system is required when testing the engine with external EGR. The pressure of the exhaust system must be kept higher than the intake system to drive flow through the EGR valve. The brake valve implemented was a 2” exhaust flap used in Volkswagen Turbocharged Direct-Injection vehicles. The VW exhaust flap will be controlled using an H-bridge controller from the ECM. The exhaust back pressure valve and flange adapted to ANSI are shown in Figure 4.20.

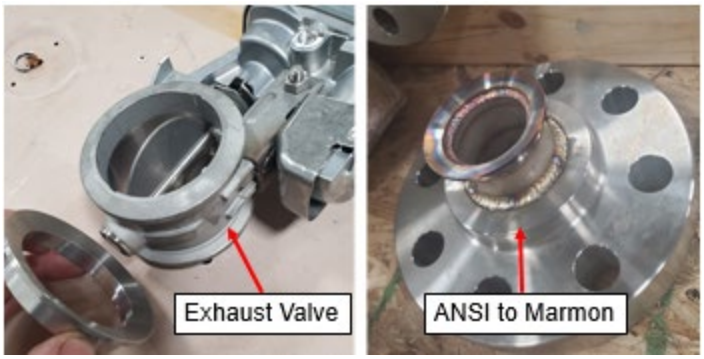

Figure 4.20: Exhaust Back Pressure Valve and ANSI to Marmon Flange

4.7.3 EGR System Design and Fabrication

The EGR system was designed to allow for hot exhaust gas to re-enter the intake stream. The conventional EGR cooler on the ISX procured was removed. The EGR loop shown in Figure 4.15 shows the exhaust gasses will flow through the exhaust surge tank, and then an EGR valve and back into the intake stream with no cooler in the loop. The pipe used up to the EGR valve is either 304 or 316 Sch. 80 SS pipe. The EGR pipe which splits off from the exhaust gas outlet is 1.5-inch SS pipe coupled to a 1.5-inch marmon flange which allows for the proper connection to the EGR valve used. The marmon flange is welded on and shown in Figure 4.20 at the EGR inlet. Figure 4.21 also shows the exhaust surge tank, exhaust t-fitting, exhaust outlet, and the EGR valve.

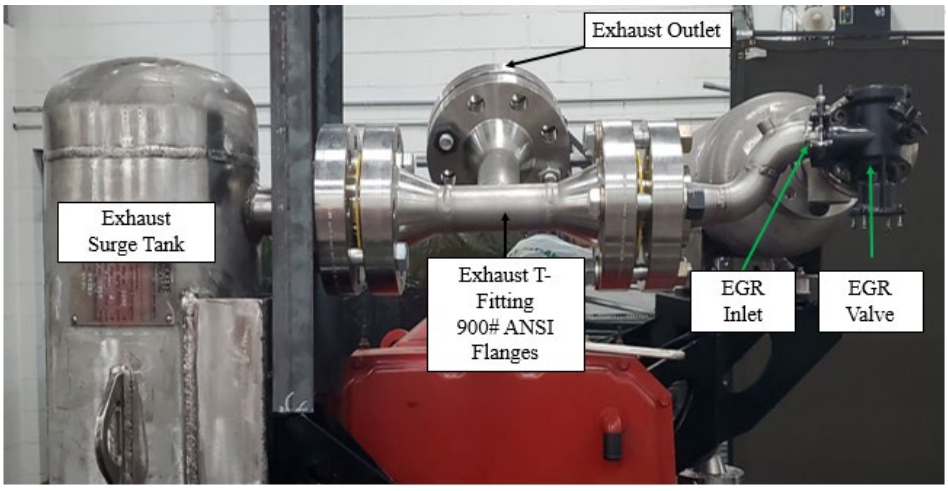

Figure 4.21: Fabricated EGR System

The EGR valve implemented was procured from a 6.7L Cummins ISB engine. The valve used has two ports and allows for a linear actuator setup to control the overall orifice size on for the valve. The linear actuator used for the actuation was a 12V Glideforce linear actuator with a 2-inch stroke with 490N of actuating force. The actuator can accelerate the actuator with 490N and hold static loads up to 2500N.

4.8 Implement Stand-alone ECM

The 5554-112 -ECM (Engine Control Module) chosen to control the engine procured from Woodward. The MotoHawk ECM allows for many user inputs and outputs while also allowing for rapid development of control strategies for the engine. The ECM allows for you to flash the controller with data if changes to PID values or control strategies is required. The ECM allows for many inputs/outputs to allow for proper control of the engine shown in Table 4.8. The portions of the ECM that will be utilized for controlling the engine are shown highlighted in green.

Table 4.8: MotoHawk ECM Capabilities

MotoHawk ECM	I/O/Communication Type	Amount Available
Inputs	Engine Position Sensors	2
	Knock Sensors	2
	O2 Sensors (Narrowband)	4
	Digital Inputs	3
	Analog Inputs (0-5V)	33
Outputs	Main Power Relay	1
	H-Bridge Output	2
	Injector	8
	Spark Trigger	8
	Tachometer	8
	Low-side Drivers	1
Communication	Communication CAN	3
	RS-485	1

4.9 Increased Compression Ratio Plan

4.9.1 Stock Compression Ratio Measurement

The stock CR of the engine according to the OEM is 17:1 [47]. With a compression ratio of 17:1, IAT would have to be raised substantially to reach EOC temperatures near 1200K. As the CR is increased, the required IAT decreases as shown by Figure 3.1. The head was removed from the ISX engine block. With the head removed and the piston was cleaned to allow for an accurate measurement of the volume within the piston bowl and crevice volume.

The measurement process for measuring the stock compression ratio included the measurement of multiple volumes. The volumes measured included the titrated volume below each of the valves within the cylinder head. An image of each of the valves within the head and their correlated numbers is shown Figure 4.22. Each of the valves were measured three times and averaged to a single value. The average volumes below each valve are given in Table 4.9 and added to a total volume of valves within the head to 11.85 mL.

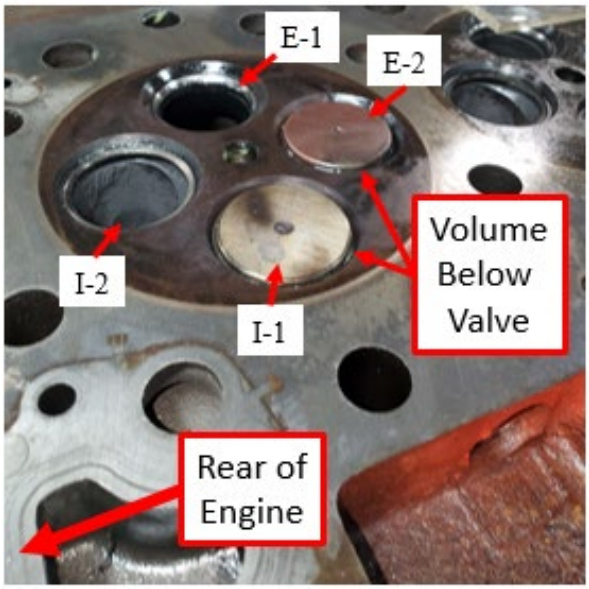

Figure 4.22: Valve Number and Location ISX Volume Measurements

Table 4.9: Valve Volumes Measured

Valve Name - Number	Average Volume (mL)
Intake Valve I-1	3.1
Intake Valve I-2	3.2
Exhaust Valve E-1	2.5
Exhaust Valve E-2	3.05
Total Volume of Valves (head)	11.85

The second volume measured was the head gasket volume taken by measuring the crushed thickness of the head gasket, specifically the fire ring, and the diameter of the fire ring. The four measurements taken with micrometers per each cylinder, the average of each cylinder, and the entire head gasket average is given in Table 4.10. The head gasket thickness was determined to be 1.963 mm thick. The diameter of the fire ring bore measured with calipers was measured three times per cylinder and averaged to determine the total volume within the head gasket. The measurements for the head gasket calculation are shown in Table 4.11. The average of each cylinder bore was determined to be 146.197 mm. The average volume within the head gasket is by itself is 32.952 mL, but the way the piston volume is measured, if the value of 32.952mL was used, the CR would be underestimated for double counting a volume.

Table 4.10: Head Gasket Thickness Measurements

Head Gasket Thickness (mm)						
	Cylinder 1	Cylinder 2	Cylinder 3	Cylinder 4	Cylinder 5	Cylinder 6
Measurement 1	1.98	1.95	1.97	1.98	1.98	1.94
Measurement 2	1.98	1.99	1.97	1.98	1.99	1.97
Measurement 3	1.94	1.93	1.94	1.98	1.95	1.97
Measurement 4	1.96	1.918	1.956	1.986	1.96	1.94
Average of 1-4	1.97	1.95	1.96	1.98	1.97	1.95
Average of All	1.96					

Table 4.11: Head Gasket Bore Measurements

Head Gasket Bore (mm)						
	Cylinder 1	Cylinder 2	Cylinder 3	Cylinder 4	Cylinder 5	Cylinder 6
Measurement 1	146.43	146.33	146.13	146.13	146.10	146.12
Measurement 2	146.23	146.34	146.20	146.15	146.38	146.10
Measurement 3	146.15	146.08	146.30	146.08	146.08	146.15
Average of 1-3	146.27	146.25	146.21	146.12	146.1+	146.14
Average of All	146.20					

Figure 4.23 shows a cross-section CAD model of the piston, head gasket, and cylinder liner. The head gasket fire ring thickness is 1.963mm, and the cylinder liner surface is 0.229 mm above the block deck. The fire ring rests upon the cylinder liner surface, but the cylinder liner also has a ring that protrudes further upwards toward the cylinder head shown in Figure 4.21. The cylinder liner ring is 1.956 mm above the cylinder block deck, and the piston surface was measured at 0.838 mm above the cylinder block deck at TDC. The first volume of the head gasket can be measured as the volume outside of the cylinder liner outer diameter (OD) which is 144.3mm and inside the inner diameter (ID) 146.2 of the head gasket. This is depicted by section A in Figure 4.21. The height of this volume is the difference between the liner ring above deck and the liner above deck which is 1.727 mm. The volume of this region is 0.78 mL. The second volume depicted by section B is the entire diameter of the head gasket and the height of the head gasket minus the liner ring height which is 1.963 mm minus 1.727 mm totaling to 0.236 mm height with a diameter of 146.197 mm. The volume of section B is calculated to 3.96 mL.

The total volume of the head gasket adding sections A and B together is then added up to 4.74 mL.

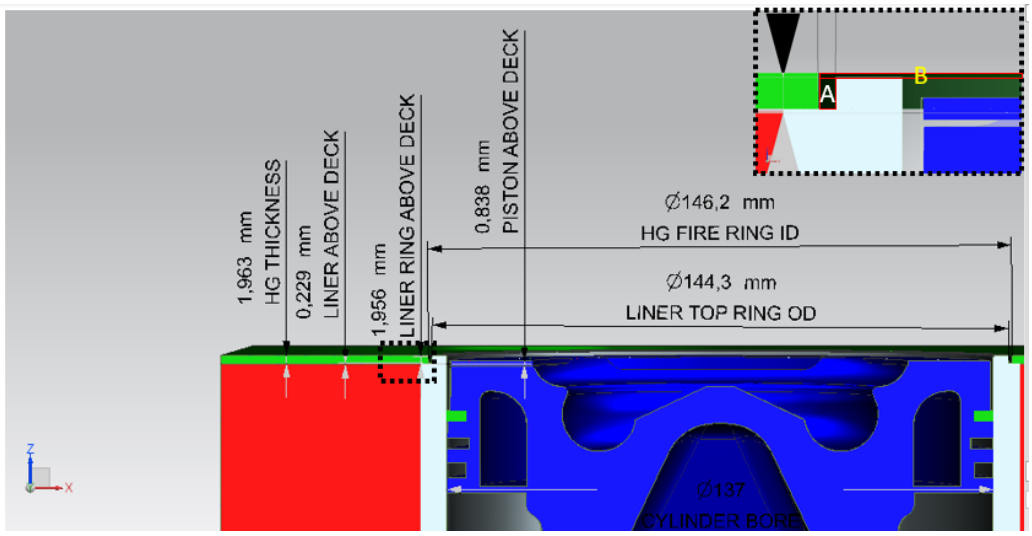

Figure 4.23: Piston, Head Gasket, and Cylinder Liner Measurements Section View

For method 1, the volume below the top ring of the cylinder liner was then measured using a burette filling in the volume three times and taking an average. It should be noted that the crevice volume was filled in with grease and was calculated after the titration was completed. The crevice volume was calculated by taking the distance from the piston top surface to the first ring which was 12.5 mm and the difference between the piston diameter above the top ring land 134.92 mm and the bore of the engine 137 mm. The crevice volume was calculated at 5.55 mL.

A second method was also used to calculate the compression ratio by placing the compressed head gasket on the cylinder block and measuring the entire volume of the combustion chamber decreasing the error in calculation of the head gasket volume calculations. The second method was repeated two times while also calculating the crevice volume for these calculations. A summary of the CR calculations can be found in Table 4.11. The average of method 1 shows a compression ratio of 18.43 while the average of method 2 gives a compression ratio lower at 17.48 which is closer to the OEM specification. After the calculations were carried out and an average of all measurements

was taken, it seems the compression ratio with a crushed head gasket is approximately 18.05, one point higher than the OEM specification of 17:1.

Table 4.12: Stock Compression Ratio Measurement

Portion of CR Calculation	Volume Measurement	Method 1			Method 2	
		Measurement 1	Measurement 2	Measurement 3	Measurement 4	Measurement 5
Clearance Volume (V_C)	Crevice Volume (mL)	5.55	5.55	5.55	5.55	5.55
	Head Gasket Volume (mL)	4.74	4.74	4.74	0	0
	Valves in Head Volume (mL)	11.85	11.85	11.85	11.85	11.85
	Piston Chamber Volume (mL)	119.3	122.8	120.2	134.3	133.2
Swept Volume (V_D)	Displaced Volume (mL)	2491.25	2491.25	2491.25	2491.25	2491.25
$(V_C+V_D)/(V_C)$	Compression Ratio	18.61	18.19	18.50	17.42	17.54
Average by Method		18.43			17.48	
Average of All		18.05				

4.9.2 Higher Compression Ratio Pistons

A range of piston compression ratios were simulated using GT-power as well as with CFD chemical kinetic combustion modeling completed by Westport Fuel Systems. The plan to increase the CR in order to achieve higher EOC temperatures and decrease required IAT was studied using GT-power as discussed in 3.1. The range of CR's studied included baseline 17:1 up to 27:1. It was determined from mode B100 that a 27:1 CR may be too high to maintain reasonable peak pressures within the engine. CR's below 25:1 show that peak pressures were maintained below 250 bar at the high load case of B100.

Multiple piston designs were developed between MTU and Westport. The final piston compression ratios chosen for manufacturing included CR's of 17:1, 23:1, and 27:1 piston, and using a billet aluminum piston design manufactured by Diamond Racing Pistons. The choice of 17:1 piston was chosen to compare heat transfer between the stock (steel) piston within year 2 and year 3 of the project if chosen to do so. The 23:1 piston was chosen to provide a mid-range CR between the maximum design limit of 27:1 and

stock CR of 17:1. The 27:1 piston was chosen to ensure that we could reach the high limits of CR if chosen to do so during engine testing within year 2 and 3 of the project. The 27:1 piston also allows for shimming of the head gasket to decrease the CR as well by moving the head away from the block.

The first initial step of getting the aftermarket pistons made was running a thermal analysis on the piston, which was completed by Westport. With the thermal analysis to be completed on both the stock, and aftermarket pistons, a base CAD model for the stock as well as the aftermarket pistons was created. The OEM piston CAD model was developed by measuring various key parameters from the OEM piston purchased early in the project. The model was developed using Unigraphics NX. Figure 4.24 shows various views compared from the OEM piston to the OEM CAD model.

Figure 4.24: Isometric, Wrist Pin, Skirt, and Bottom View Comparison

For the aftermarket pistons there are a few differences due to using aluminum pistons rather than a steel material. The first difference is the skirt of the piston, which are thicker providing more structural integrity to the skirts due to aluminums lower yield stress. The second difference is not using the conventional oil gallery that is in the stock OEM pistons. The oil gallery manufactured in the stock pistons was not offered from the supplier chosen and is less of a concern with aluminums higher rate of heat conductivity

240 (W/m-K) at 127°C compared to steel heat conductivity 33 (W/m-K) at 122°C [47]. While this means that more heat will be transferred through the aluminum pistons decreasing the efficiency compared to steel pistons, it also means that aluminum can reject the heat faster as well which allows the oil gallery to be removed from the aluminum pistons. The last difference is the distance between the combustion bowl and the back side of the piston which was increased to 12.7 mm compared to the OEM being measured at 9.04 mm. An approximate cross section comparison of the OEM piston and custom SCRE piston is shown in Figure 4.25.

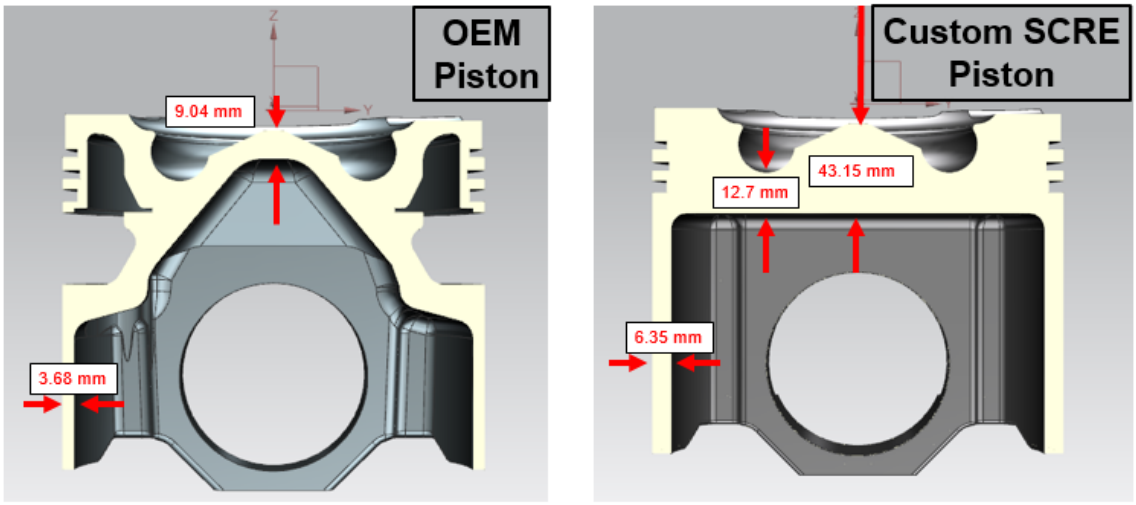

Figure 4.25: Cross Section of Piston Design Differences (OEM vs. Aftermarket)

Data from the GT-power 1D simulation was provided to Westport for engine speed/load case A50 along with the CAD files to both the OEM and SCRE aftermarket pistons. The data was then used to run a thermal analysis on both the OEM piston and aftermarket piston to determine the impact of changing from steel to aluminum as well as when decreasing the bowl geometry to increase the compression ratio. The data from the 1-D GT-power model was coupled to Westport's CFD model. The piston surface temperature map was generated and simulated while patching temperature fields from EVO to IVC. The map surface temperatures were then applied to the solid piston model provided to generate a thermal simulation on the piston. A photo from the thermal analysis showing

wall heat flux at 0°, 3.6°, 7.2°, and 10.8° ATDC is shown in Figure 4.26 completed by Westport.

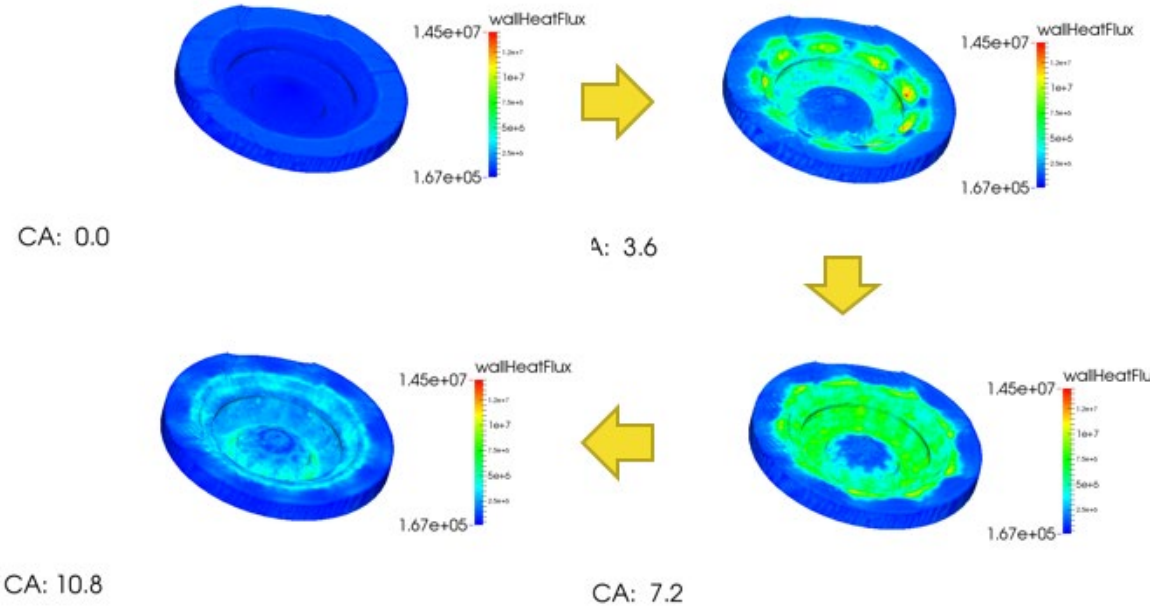

Figure 4.26: Piston Surface Temperature Mapping

Westport identified two hot spots in the thermal analysis to monitor throughout their testing including temperatures at the rim of the piston and the pip shown in Figure 4.27. The model was used to check various designs for both the OEM dimensions as well as various bowl geometries using a steel piston with an oil gallery and the OEM piston without an oil gallery using aluminum as the material.

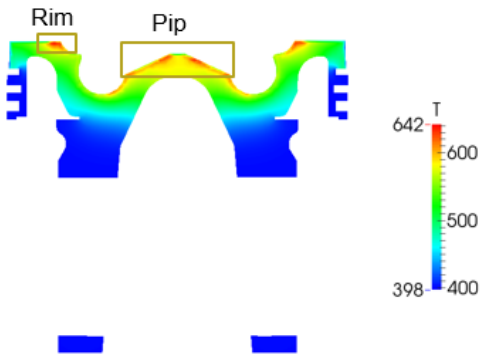

Figure 4.27: OEM Thermal Simulation Hot Spots

The data that was presented to Westport included crank angle resolved pressure and temperature data for multiple CR values at various IAT to achieve CNG autoignition. The data was provided from case A50 and the thermal analysis was conducted on assumed high temperature conditions depicted by Figure 4.28 for points A, D, and F. as well as the OEM 17:1 piston and a 27:1 piston as well. The IAT is shown on y-axis while the compression ratio is shown on the x-axis. The SOI used for these simulations is 5° BTDC.

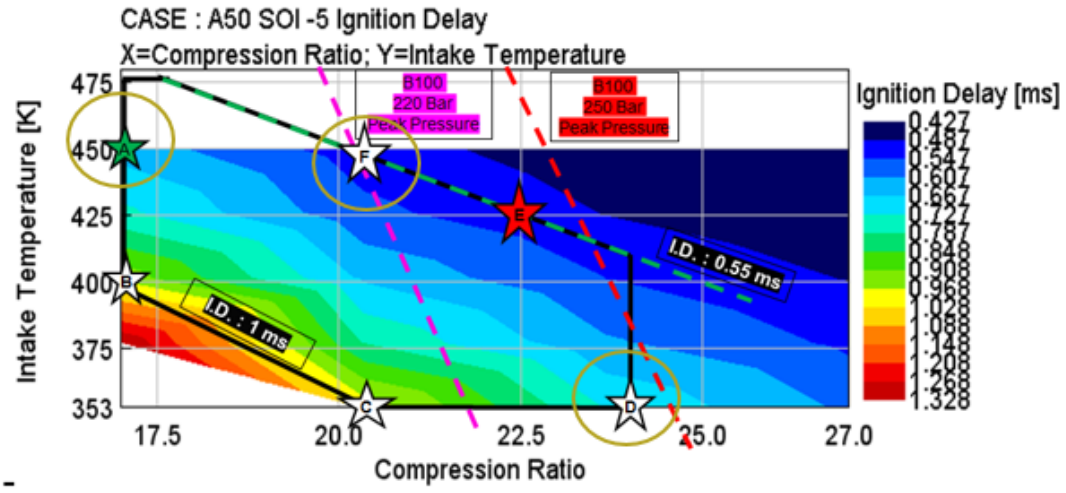

Figure 4.28: Data Points Analyzed by Westport for Thermal Analysis

With the data input into the model the simulations were conducted on both OEM (steel 17:1) and fabricated pistons (Aluminum). Figure 4.29 shows the various piston pip temperatures vs. time until the temperatures were stabilized for the various pistons and CR's. The first conclusion from this figure is that the steel OEM piston will exhibit higher temperatures due to the lower thermal conductivity compared to aluminum. The OEM piston stabilized temperature at the pip was above 700K (427°C) and took nearly 150 seconds to stabilize, while the fabricated pistons reach peak temperatures around 500K (226°C) in nearly 1/6th of the time (25 seconds) due to the thermal conductivity of aluminum being much higher.

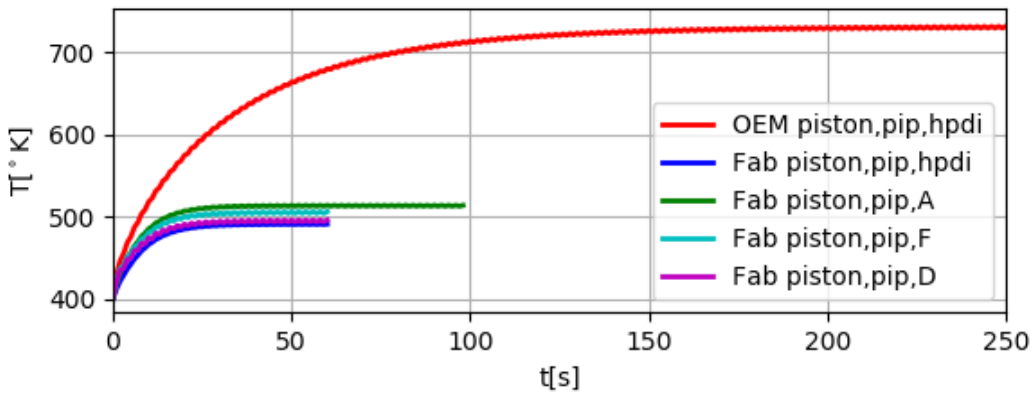

Figure 4.29: Pip temperature vs. Time Thermal Analysis

Figure 4.30 shows the heat loss through the piston for both the OEM piston with a 17:1 compression ratio vs. the fabricated piston also at 17:1. The results show the OEM piston heat loss is approximately 3.5 kW while the aluminum piston shows 70% higher heat loss at 6 kW. One way to possibly mitigate this is with a thermal barrier coating (TBC) to decrease the heat transfer through the piston.

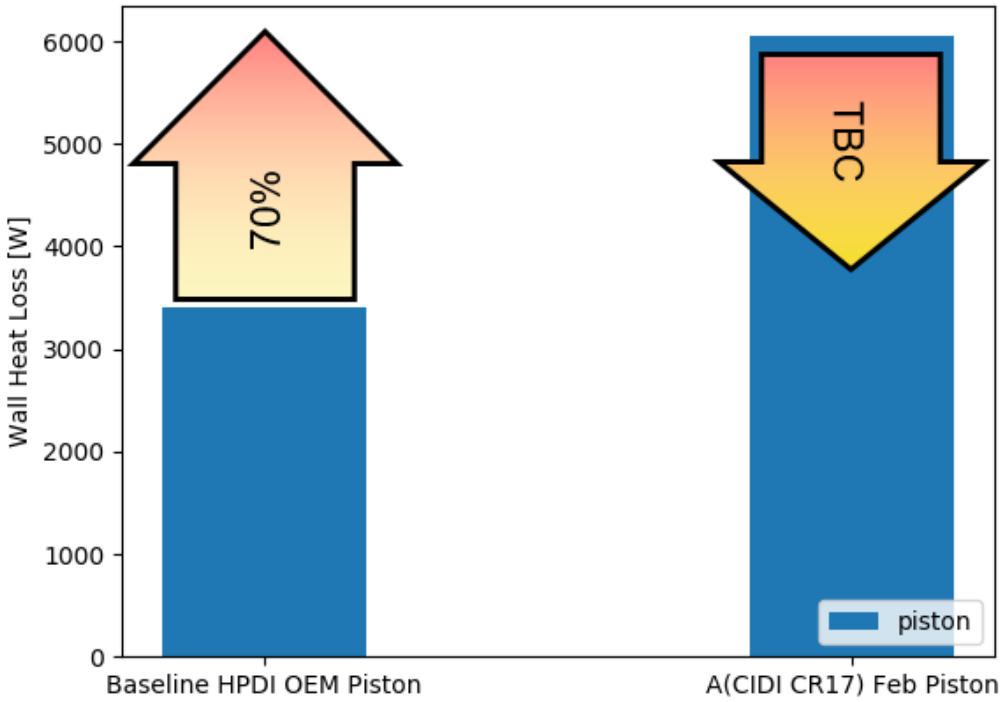

Figure 4.30: Baseline OEM vs. Fabricated Heat Loss

Figure 4.31 shows the peak rim and pip temperatures for both the OEM and fabricated piston at 17:1 CR. This shows that the temperatures on the piston in both indicated hot spots are reduced to below 500K (226°C) when using an aluminum piston. This was good reassurance that the aluminum pistons will not reach melting points during this operation of the engine as the melting point of aluminum is near 660°C.

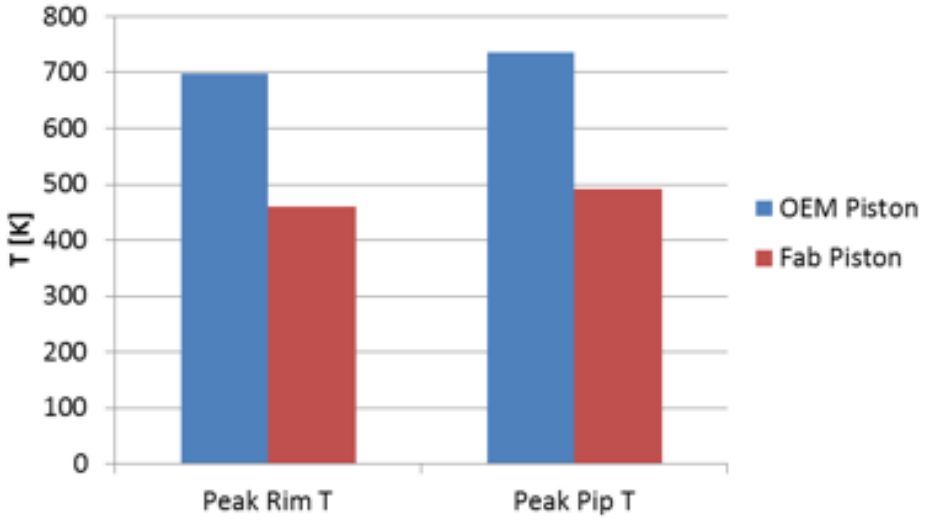

Figure 4.31: Peak Piston Temperature OEM vs. Fabricated

The last figure generated by Westport was the comparison of the peak rim and pip temperatures for the various CR's. The 17:1 (A) point at an IAT of 450K exhibits the highest pip temperature at 512K and the lowest rim temperature of 462K. When the CR was increased to 20:1 while maintaining the same IAT the pip temperature decreased to 506K while the rim temperature increased to 480K. The 23:1 (D) CR, decreasing the IAT to 353K while maintaining approximately the same ID as point A, the pip temperature was simulated at 496K and the rim at 488K.

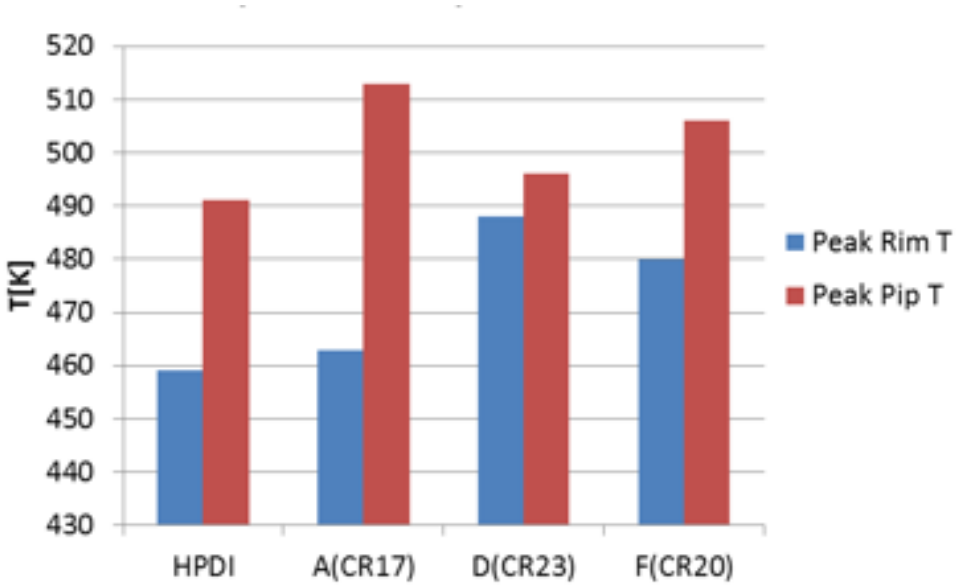

Figure 4.32: Peak Temperature Comparison for Fabricated Pistons vs OEM

In conclusion it was determined that the OEM pistons will observe higher temperatures, but lower heat loss due to the thermal conductivity of the material compared to the fabricated pistons. It was also determined that pip temperatures decreased as the CR is increased from 17 to 20 and 23, while the rim temperatures increase as CR was increased shown by Figure 4.23. The result was that each of the fabricated pistons will be sufficient in operation of the mono-fueled DI CI NG SCRE.

4.9.3 Bowl Designs for Manufacture

Once the thermal study was complete and the piston CR's were selected the bowl geometries were provided by Westport to be drafted and sent to the aftermarket supplier. The bowl designs for each of the compression ratio use the same compression height of the OEM piston that was measured on the stock piston. Each of the bowls have the same squish height. The bowl comparison is shown in Figure 4.33. The full drawing of each of the bowls can be found in appendices A.5.

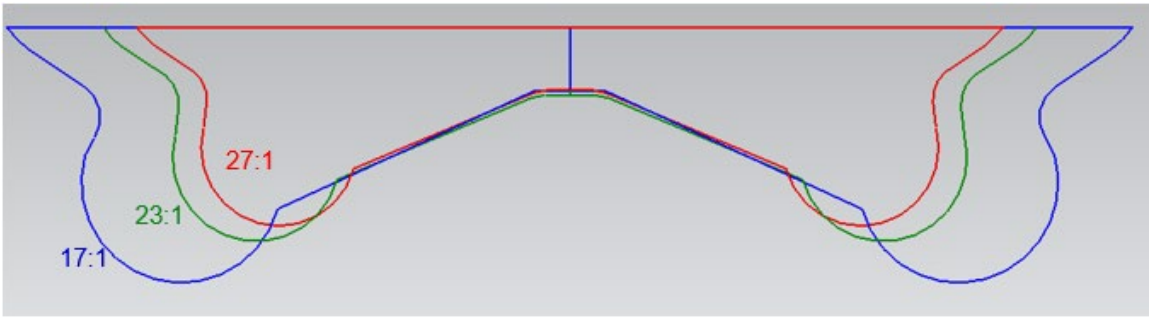

Figure 4.33: Fabricated Bowls Comparison

The piston bowls and drawings along with an OEM sample including the ring pack and wrist pin were sent to Diamond Racing Pistons for manufacturing. Other dimensions given to the manufacturer included the position of the oil squirting nozzle, bore diameter at various depths from TDC and dimensions of the small end of the connecting rod for the wrist pin.

The final pistons compared to the OEM piston bowls are compared in Figure 4.34. From left to right, the CR's are 27, 23, and 17:1 respectively with the OEM CR being given on the far right. The valve reliefs on the pistons remained consistent circles while the diameter as the diameter of the rim increases from left to right.

Figure 4.34: Aftermarket Piston to OEM Bowl Comparison (Manufactured)

Figure 4.35 shows the skirt and the wrist pin side views of the aftermarket aluminum pistons. The skirt length compared to the OEM piston is increased, while the compression height of the piston remained the same (i.e. distance from top of piston to center of the

wrist pin bore). The wrist pin bores for all six aftermarket pistons were finished with a boring process by North Central Engine Repair to 0.0025” clearance.

Figure 4.35: Skirt and Wrist Pin Side Views

Figure 4.36 shows a bottom view of the aftermarket pistons and some important features. First, the ring land oil passages drilled through the piston to allow for the oil nozzle spray to reach the bottom ring for lubrication of the piston skirts. The second important feature is the relief cuts that were manufactured for clearance purposes of the oil nozzle located at the bottom of the cylinder. While there is only one nozzle located at the bottom, reliefs were manufactured on both sides of the pistons. This relief is also visible on the skirt and wrist pin side views shown in Figure 4.35.

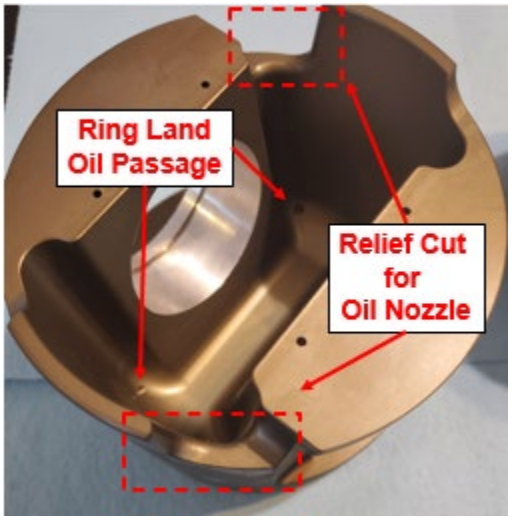

Figure 4.36: Bottom View of Aftermarket Piston

The 23:1 compression ratio bowl was selected as the first piston for initial testing per Westport's recommendation. This piston was also measured for CR and was measured at 23.5:1. This piston will allow for decreased IAT to reach CNG auto-ignition temperatures as well as decreasing the heat load on the piston according to Westport's thermal studies.

Another important factor of the aftermarket higher CR pistons is the surface area which impacts the heat transfer. GT-Power's Woschni heat transfer model uses a ratio of the piston surface area compared to the area of the bore (137mm). The area of the cylinder bore is calculated at 14741 mm^2. Using the CAD models created for manufacturing by Diamond Racing, the surface areas and multiplier ratios were calculated for each of the CR's both with and without the crevice surface area added. Table 4.13 shows both excluding and including the crevice are the piston surface area and its respective piston/bore ratio to be used within the GT-Power model. The OEM model that was initially supplied by Westport had a value of 1.2 for the ratio of piston surface area to bore area, indicating the crevice area is most likely not included for the heat transfer. Further research should be conducted when modifying this area ratio within the model to determine whether to include or exclude the crevice area.

One result from Table 4.13 is the decreasing surface area as the CR is increased. From the calculations the ratio decreases from 1.30 to 1.2 and 1.7 for CR's 17, 23, and 17, respectively. While running the design of experiments in section 3.6, the area ratio was not varied. This design of experiments could be re-tested with the various surface area ratio's as the CR is varied to predict heat transfer more accurately within the model.

Table 4.13: Piston Surface Area and Ratio Multiplier

Compression Ratio	Excluding Crevice		Including Crevice Area	
	Piston Surface Area (mm^2)	Piston/Bore Surface Area Ratio	Piston Surface Area (mm^2)	Piston/Bore Surface Area Ratio
CR 27	17280.00	1.17	22595.00	1.53
CR 23	17726.00	1.20	23041.00	1.56
CR 17	19175.00	1.30	24490.00	1.66

4.10 Intake Air Heater Plan

As a method of assisting in achieving EOC temperatures near 1100K an intake air heater (IAH) was procured. The selected IAH had multiple requirements including maximum flow rate, and maximum temperature at a maximum required flow rate. To determine flow rate requirements, the lowest CR piston was selected to determine the required IAT. As Figure 3.20 shows, the lowest CR (17:1) requires the highest IAT heating to achieve 1100K EOC temperature. The required IAT to reach 1100K at 17:1 CR for engine mode A50 in Figure 3.20 is 406K (133°C). For mode A25, a leaner case, the required IAT for auto-ignition showed to be 425K (177°C). For insurance purposes, the requirement was set to ensure the heater was able to provide 200°C IAT throughout all loads if the stock CR was to be used.

The required loads dictate how much mass of air is required to flow through the heater. Case B100 i.e. 100 percent load at 1500 RPM required 271 kg/hr of air flow rate through the intake and 48 kg/hr of EGR flow rate to simulate the required load with 15% external EGR. The total flowrate into the cylinder was 320 kg/hr (Air + EGR). In the SCRE setup only the air will be heated by the IAH. The external EGR will be hot and will not require re-heating. While the EGR does not have to be re-heated, the total air flow of 270 kg/hr or 134 standard cubic feet per minute (SCFM) was used as the maximum flowrate required to be heated by the IAH using the lowest CR piston to achieve combustion. Figure 4.37 shows the rate temperature output of the 18kW heater procured from Tutco. The 2.5-inch NPT inline heater is rated up to a maximum temperature of 750°C at 10 SCFM, and 260°C at 133 SCFM. As a safety factor a 25% heat loss was added to the rated temperature shown in Figure 4.37 as the grey line. The peak temperatures achievable engine load cases A25, A50, and B100 are shown as the red, green, and purple stars. Case B100 shows that with the 25% heat loss safety factor the heater can still achieve 200°C IAT. It should also be mentioned that if the engine CR is increased the required temperature at the given flow rate will become less as mentioned in previous sections. The lowest CR requires the highest IAT, and all loads are shown to be

achievable, even with a 25% heat loss from the rated temperature vs. flow rate shown in Figure 4.37.

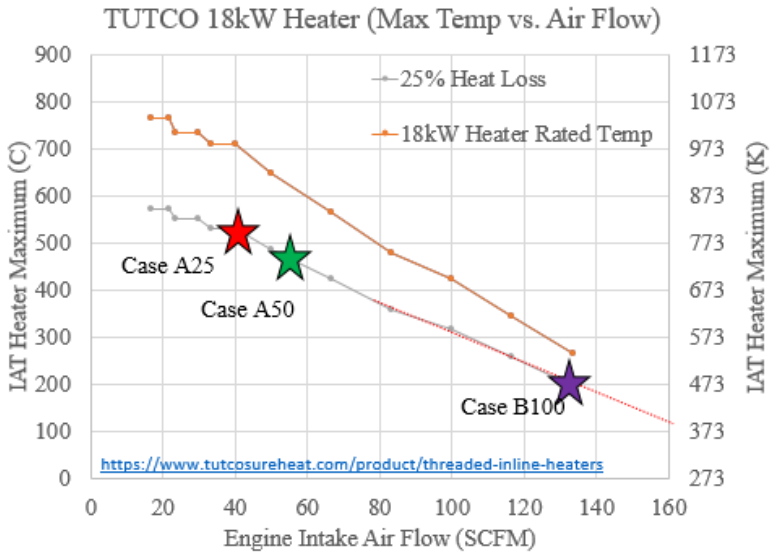

Figure 4.37: Tutco Sureheat 18kW Heater Temperature vs. Flow Rate

The 18kW heater shown in Figure 4.38 is powered by 480V 3-phase electrical power. The heater will be controlled with a silicon-controlled rectifier (SCR), specifically a DIN-A-MITE C controller from Watlow. The intake air flow and control schematic are shown in Figure 4.39.

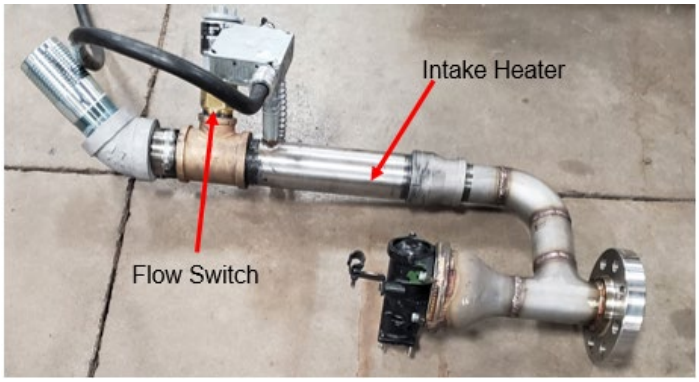

Figure 4.38: 2.5-Inch NPT Inline 18kW 480V Intake Air Heater

Figure 4.39 shows the flow and control schematic for intake air control and heating. If no boost is supplied the flow will come through as NA filter. If compressed air is supplied, it

will first flow through a compressed air filter procured from Industrial Air Power. The compressed air filter is rated to 710 SCFM with a 5-micron filter rating. Additional filters are available down to 0.01 microns provided by Industrial Air Power.

The compressed air will then flow past a flow switch. The vane-operated flow switch procured from Dwyer Instruments is plumbed inline prior to the intake air heater. With the vane operated switch plumbed perpendicularly into the 2-inch intake air stream, actuation of the switch will occur between 13 and 23 SCFM. The flow switch will be used to ensure the heater does not turn un unless air is flowing through the heater i.e. engine is motoring. With idle speed being 800 RPM, and displacement being 2.5L density of air at atmospheric conditions assumed to be 1.225 kg/m^3 and an approximate volumetric efficiency of 0.8, the flow rate is 0.98 kg/min or 59 kg/hour which converts to 29 SCFM. This means at the lowest engine RPM of 800 RPM, the engine will produce enough flow when motoring to allow the heater to turn on when running NA.

Once the flow switch is turned on when a 13 SCFM intake air flow rate is reached, the engine control signal ranging from 4-20 mA is then passed through to the DIN-A-MITE C. The controlled signal changes the power output supplied to the 18kW heater. The control type selected for procurement was single-cycle variable time based where the output to the heater is directly proportional to the input signal (4-20 mA). The accuracy of the controller output power kW is within 5% of the input signal mA during ambient conditions in the controller enclosure (25°C). The 40-amp rated DIN-A-MITE C is fed the 480V 3-phase power, and the 4-20mA signal controls the output to the Tutco 18kW heater. The DIN-A-MITE C will be fed a signal from the engine or test cell controller with an integrated PID control. The input to the PID controller in NI-Veristand or the ECU controller will be temperature at the intake manifold, and the output will be a 4-20mA signal to the SCR.

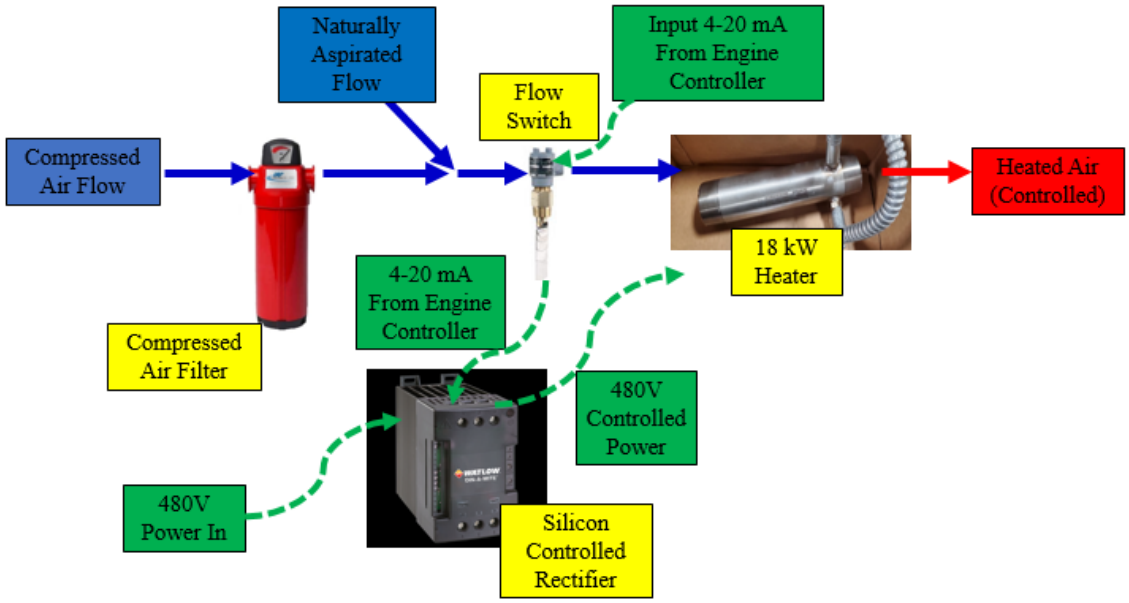

Figure 4.39: Intake Air Flow and Control Schematic

The intake air heater control box and the required components are shown in Figure 4.40, The 480V power comes in through the top of the box, and feeds into the fuse block with 50A fuses. The 480V then feeds into the Watlow DIN-A-MITE C SCR and then out of the bottom of the box. The grounding bar shown to the right of Figure 4.40 is used to ensure the 480V and controller are grounded. The current clamps shown are for feedback to the DIN-A-MITE C to alert the controller of a short-circuit or an open heater. The heater control box shown in Figure 4.40 was mounted on the engine cart behind the control panel area and above the CNG booster. The DIN-A-MITE C is controlled by a 1 to 5-volt signal which correlates to a 3.9 to 19.6 mA current for the control of the heater.

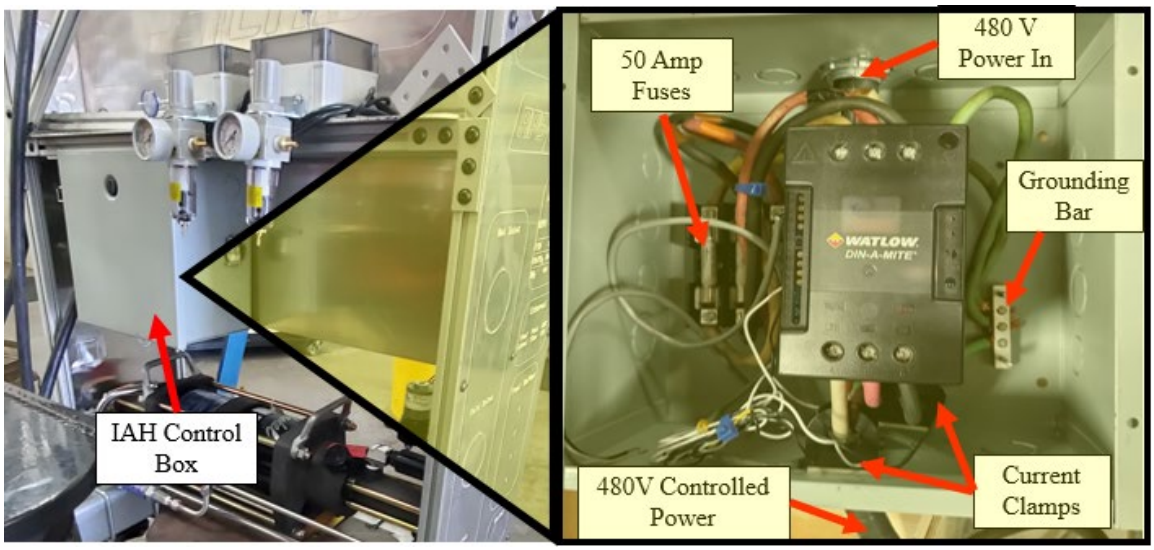

Figure 4.40: IAH Control Box

4.11 Machine Cylinder Head

Two holes were machined in the ISX SCRE cylinder head. Both holes are in cylinder six combustion chamber. The holes were drilled to insert transducers/sensors monitor the heat flux as well as the cylinder pressure throughout the engine cycle on a crank angle basis. Figure 4.41 shows an image of both the top and bottom view of the cylinder head machining completed for measuring cylinder pressure and heat flux through the cylinder head. Figure 4.42 shows the cross section of the heat flux transducer and cylinder pressure transducer assemblies including the sensors, the sleeves, clamping nuts, and copper crush washers. The transducer sleeves seal at the base with a copper crush washer, while the top seals the coolant jacket at the threads with Loctite thread sealant. The dimensions for the drilling of the two holes were based upon the injector bore center shown in Figure 4.43. The sleeves internal boring is dimensioned based upon the required bore sizing for the 6125C Kistler transducer. Both the cylinder pressure sensor and heat flux transducer contain the same base outer dimensions allowing the sleeves to be designed the same.

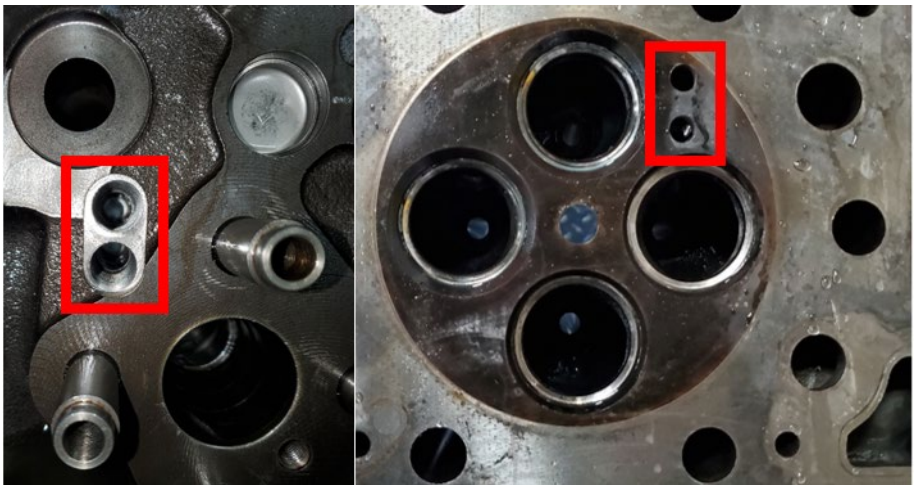

Figure 4.41: Top and Bottom View of Cylinder 6 Combustion Chamber Head Machining

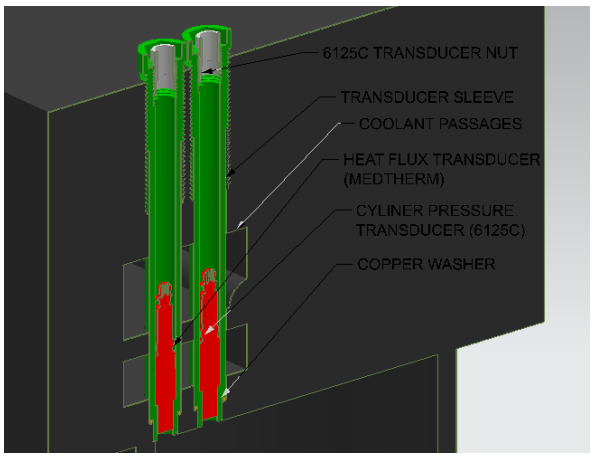

Figure 4.42: CAD Model of Heat Flux and Cylinder Pressure Transducer Assembly

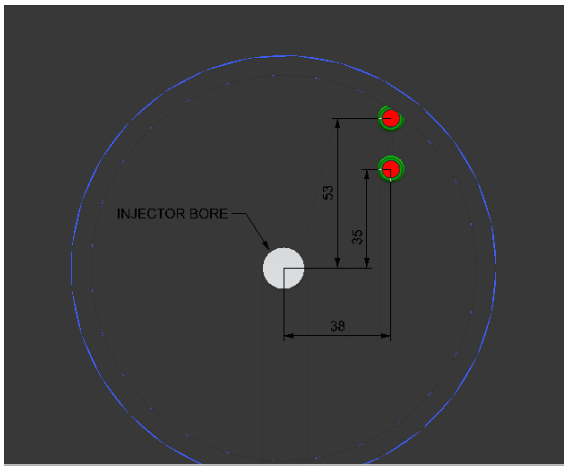

Figure 4.43: Cylinder Pressure and Heat Flux Transducer Dimensions

4.12 Design and Manufacture System for Cylinder Deactivation

Cylinders one through five were deactivated by removing the rocker levers for both the valvetrain and the injectors. The purpose for removing flow through five of the six cylinders was to decrease fuel consumption from the facility as well as allowing for a SCRE operation. The SCRE allows for monitoring only one cylinder decreasing the cost to instrument all six cylinders. Cylinder six rocker lever for the mechanical injector was also removed shown in Figure 4.44. The rocker levers that were removed were replaced with rocker shaft oil covers to maintain the proper oil pressure. The dimensions for the internal diameters were turned down on the lathe to the dimensions of the rocker levers specified by Cummins Quickserve. Dimensions for the valve and brake rocker shaft covers between 35.037-35.138mm while the dimensions for the injector rocker shaft covers were machined to an internal diameter between 45.037 and 45.138 mm. The removal of the rocker levers enables the deactivation of cylinders one through five by not flowing the air to flow in or out of the cylinders. The trapped air within each of the cylinders will act as a spring mass damper system.

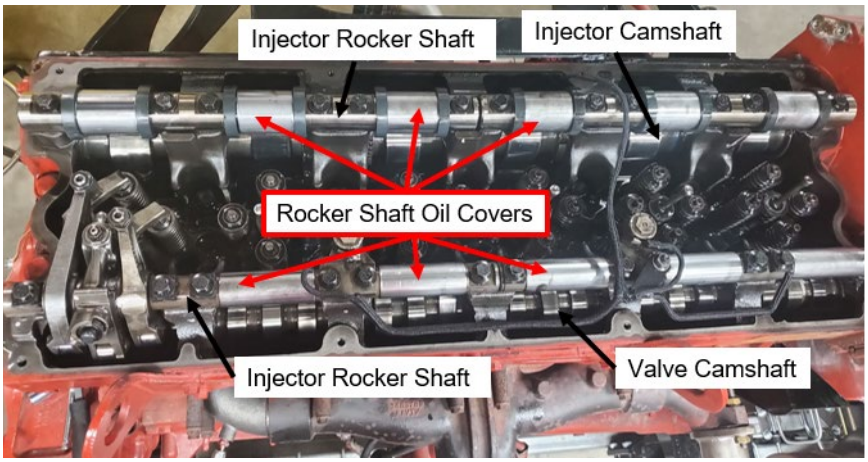

Figure 4.44: Injector and Valvetrain Rocker Shaft Oil Covers

4.13 Cam Timing Development Plan

While no cam timing adjustments were made to the engine, measurements were obtained to further proceed in this development plan for future work. The measurements take included valve lift, and piston to valve clearance shown in Figure 4.45 and Figure 4.46

respectively. The lift was measured by measuring with a dial indicator on both the intake and exhaust valve rocker arm valve bridge and rotating the engine measuring crank angle with a timing wheel. Within Figure 4.40 the measured valve lifts were also compared to the GT-power valve lift profiles initially provided by Westport and show good comparison.

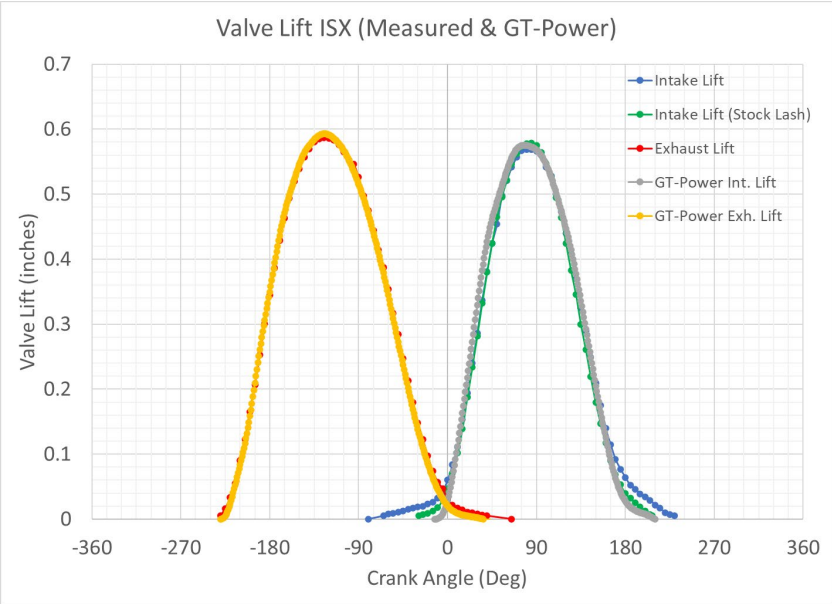

Figure 4.45: Measured and GT-Power Valve Lift Profiles

The piston to valve clearance was measured using a dial indicator on each of the four valves within cylinder six and rotating the engine using and monitoring crank angle using a timing wheel. During this operation, the normal valve springs were removed from the engine due to their high spring rate and replaced with lighter valve springs to allow for easy displacement of the valve. The piston was rotated 20 degrees before and after TDC in 2° increments while measuring the distance the valve travels before contact with the piston shown in Figure 4.46. Figure 4.47 shows the valve reference for position as well as the relief depth measured from the top of the piston for each valve relief in the piston. The arrow on the engine points toward the front of the engine, with intake valve one

being closest to the intake manifold and exhaust valve one being closest to the exhaust manifold.

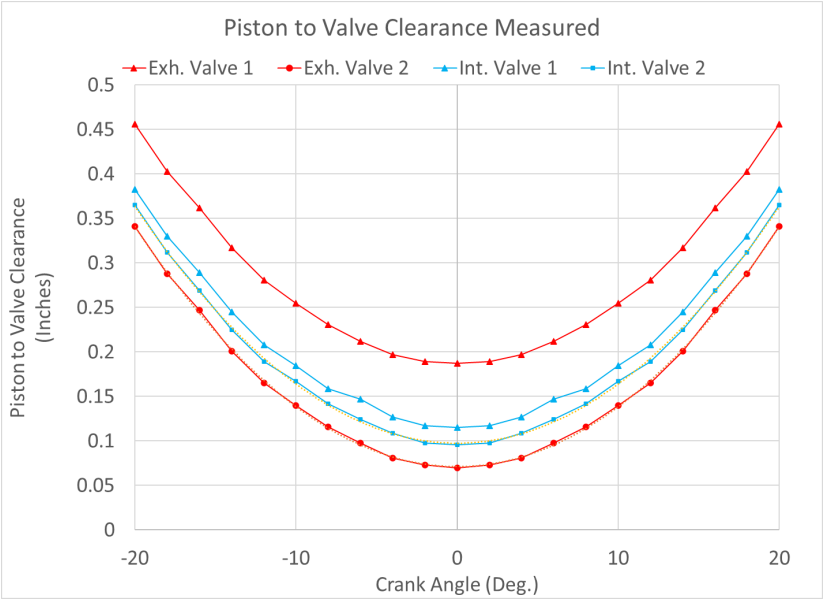

Figure 4.46: Piston to Valve Clearance Measured

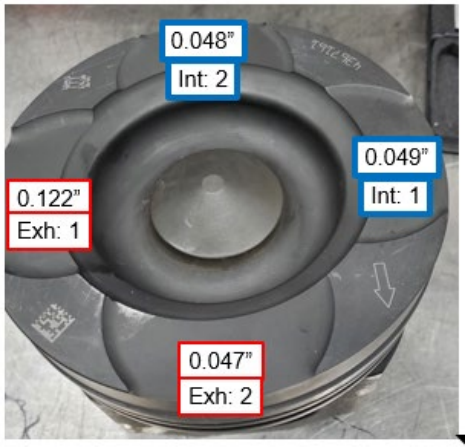

Figure 4.47: Piston Valve Reference and Relief Depth

With both measured valve lift timing and piston to valve clearance, it was possible to determine the approximate max phasing of each of the valve lift profiles. Equation 4.4 gives the calculation method for determining valve clearance during engine operation. The valve clearance is measured by taking the piston to valve clearance and subtracting the valve lift. With this approach, you can phase the valve lift events while maintaining piston to valve clearance measurements to determine the change in valve clearance if the

valve lift was phased. Figure 4.48 and Figure 4.49 show the valve clearance for the intake and exhaust for swept valve timing, respectively. The intake system shows that it can only be advanced approximately 5° before piston to valve contact occurs, where the exhaust plot shows the timing could be retarded approximately 12° prior to contact. These measurements and calculations were important in determining the possible valve phasing achieved with the recessions in the OEM pistons and first set of aftermarket pistons manufactured. Further advance and intake phasing are possible if deeper recessions are manufactured in future aftermarket pistons. As mentioned within the simulation portion, the purpose of phasing the valves would be to increase valve overlap to trap more residuals with the goal of increasing temperatures at IVC which in turn increases temperatures at EOC and decreases ID.

$$Valve\ Clearance = Piston\ to\ Valve\ Clearance - Valve\ Lift \qquad 4.4$$

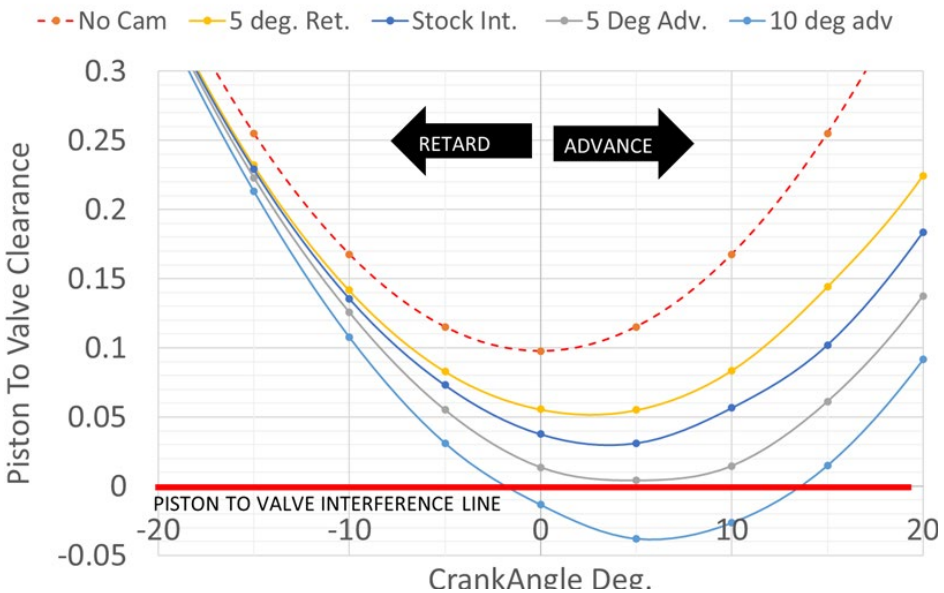

Figure 4.48: Intake Valve Lift Clearance (Timing Swept)

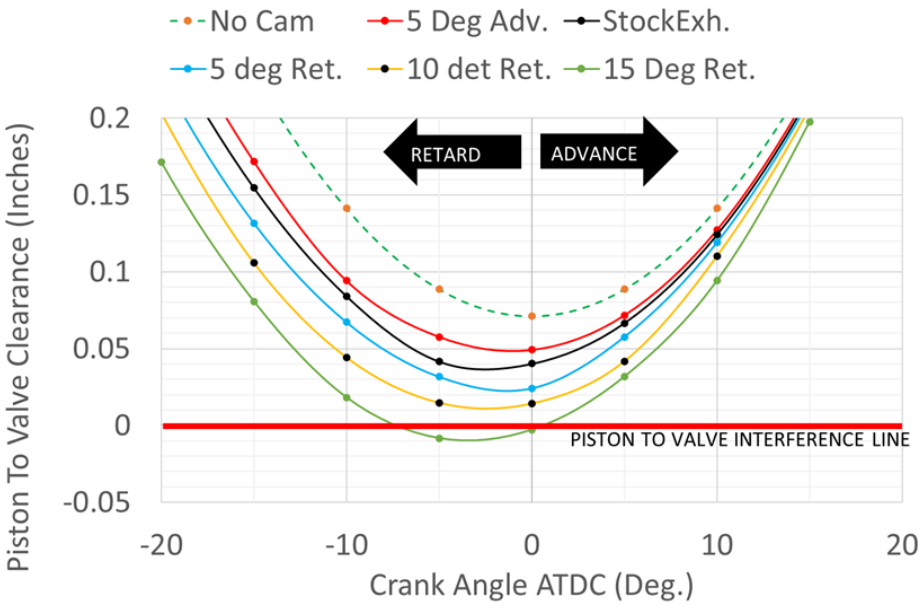

Figure 4.49: Exhaust Valve Lift Clearance (Timing Swept)

4.14 Install Sensors and Actuators

With the engine being research based and very custom for the application, many sensors and actuators were added for proper control of the SCRE. The sensor and actuator sub-systems that will be reviewed include the base engine, coolant, diesel, natural gas, exhaust, intake, and oil sub-system. Each of the sub-systems have sensors and actuators required to control temperatures, pressures, flow, and other functions of the DI CI NG SCRE.

Table 4.14 gives the base engine sensors and actuators. The first sensor within the list is the crank position sensor which was attached to the base engine when purchased. This sensor is measured with moto-tune and is used for the timing of injection evens during engine operation. The Cam position sensor which is measuring 4 teeth on the injector camshaft will be used to determine whether the engine is in the pumping loop or whether compression stroke for injection event timing. The cylinder pressure sensor used is a Kistler 6125C piezoresistive pressure transducer. This sensor will be used to measure in cylinder pressure for obtaining engine combustion metrics. The cylinder pressure sensor will be fed into the CAS Redline combustion system where it will be monitored real-time

and logged as well. The heat flux transducer is also placed in the cylinder six combustion chamber through the cylinder head and will measure the heat flux from the combustion chamber into the head. This sensor will be measured with CAS. The crank angle encoder used is a BEI 360 pulses per revolution encoder. This sensor will also be fed into the CAS system to measure the cylinder pressure against a referenced CA°.

Table 4.14: Base Engine Sensors and Actuators

Sensor or Actuator Name	Brand	Power	Control	Controller	Measured With	Actuator or Sensor	Sub-System
Crank Position Sensor	Cummins	5V	N/A	N/A	Moto-tune	Sensor	Base Engine
Cam Position Sensor (Inj.)	Cummins	5V	N/A	N/A	Mototron	Sensor	
Cylinder Pressure Sensor	Kistler	N/A	N/A	N/A	CAS	Sensor	
Heat Flux Transducer	Medtherm	N/A	N/A	N/A	Veristand	Sensor	
Crank Angle Encoder	BEI	5-28V	N/A	N/A	CAS	Sensor	

The next sub-system that was implemented is the coolant sub-system. The sub-system is used to control the coolant temperature within the engine. The coolant system plan was to add a NG powered coolant/water heater above the test cell to heat the coolant prior to motoring. The additional energy required for the coolant is required to heat the engine up quicker. With only one of the six cylinders firing, but still a very large engine mass, the engine will take much longer to heat up with this system not yet implemented.

Table 4.15 shows the sensors and actuators used for the coolant sub-system. First, the coolant pump from the OEM engine was removed to allow for coolant circulation prior to engine motoring/firing. The pump used to circulate coolant is a Taco 0012 cartridge circulating pump capable of flowing 10 m^3/hr. A coolant valve was also implemented to allow for the engine out coolant to be circulated back into the engine with a modulating

3-Way Belimo valve. This Belimo valve will be used as a mixing valve where either engine out coolant will re-enter the taco pump, or cold coolant from the heat exchanger will enter the taco-pump, or a proportion of both will enter the taco pump to head back into the engine as shown in Figure 4.50. The coolant temperature will be measured both out of the engine, as well as above the test cell from the heat exchanger using Temprel K-type thermocouple for proper control of the coolant ball-valve actuation.

Table 4.15: Coolant Sub-System Sensors and Actuators

Sensor or Actuator Name	Brand	Control	Controller	Measured With	Actuator or Sensor	System
Coolant Pump	TACO	12V (on/off)	Veristand	N/A	Actuator	Coolant
Coolant Valve	Belimo	2-10V Input	Veristand	N/A	Actuator	
Coolant Temperature (Out)	Temprel	N/A	N/A	Veristand	Sensor	
Coolant Supply Temperature	Temprel	N/A	N/A	Veristand	Sensor	

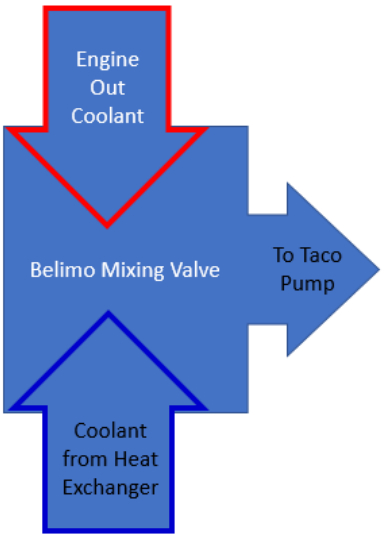

Figure 4.50: Belimo Mixing Valve Schematic

The next sub-system to be discussed is the diesel sub-system with the sensors and actuators shown in Table 4.16. The Diesel temperature will be monitored using a Temprel K-Type thermocouple. The pressure is monitored on the engine cart using a PXM309 350 bar Omega pressure transducer. This pressure will be monitored with both Veristand and Moto-tune. The pressure will be controlled by the Bosch CP3 pump fuel control actuator using a transistor-transistor logic (ttl) signal from moto-tune ranging from 75 to 90% duty cycle using a frequency of 185 hz. The motor is driven by a 2hp 120V electric motor spinning at 3450 RPM.

Table 4.16: Diesel Sub-System Sensors and Actuators

Sensor or Actuator Name	Brand	Control	Controller	Measured With	Actuator or Sensor	System
Diesel Temperature	Temprel	N/A	N/A	Veristand	Sensor	Diesel
Diesel Pressure PXM309-350G10V	Omega	N/A	N/A	Veristand and Moto-tune	Sensor	
CP3 Pump	Bosch	75-90% (185Hz.)	Mototron	Moto-tune	Actuator	
CP3 Pump 2 hp Motor	Better Electric	120V On/Off	Plug-in	N/A	Actuator	

The exhaust sub-system sensors and actuators are given in Table 4.17. The exhaust manifold pressure will be measured with a 3-bar Bosch MAP sensor typically found in intake systems on turbo applications. The back pressure within the exhaust system will be driven by a H-bridge control from the moto-tune using the moto-hawk ECM. This back-pressure valve is a throttle plate exhaust flap found in some Volkswagen vehicles capable of withstanding exhaust pressures and temperatures. The exhaust CO_2 will be measured with a 10% CO_2 meter procured from CO_2 meter.com. The O_2 sensor used to measure equivalence ratio or lambda, will be located post exhaust back pressure valve, and is measured in Veristand and moto-tune using an innovate motorsports LC2. EGT values will be measured in the exhaust manifold and exhaust surge tank using K-type thermocouples.

Table 4.17: Exhaust Sub-System Sensors and Actuators

Sensor or Actuator Name	Brand	Control	Controller	Measured With	Actuator or Sensor	System
Exhaust MAP Sensor	Bosch 3-bar MAP	N/A	N/A	Veristand & Moto-tune	Sensor	Exhaust
Exhaust Back Pressure Valve	VW	H-Bridge	Moto-tune	N/A	Actuator	
CO2 Meter (10%) Exhaust	CO2 Meter .com	N/A	N/A	CO2meter	Sensor	
O2 Sensor	innovate motorsports	N/A	N/A	Veristand & Mototron	Sensor	
Exhaust Gas Temperature (Surge Tank)	Temprel	N/A	N/A	Veristand	Sensor	
Exhaust Gas Temperature (Manifold)	Temprel	N/A	N/A	Veristand	Sensor	

The intake sub-system sensors and actuators are found in Table 4.18. The intake heater used is an 18-kW heater capable of the 450K at 140SCFM. This heater will be controlled with a 1-5V signal from Veristand. The intake air regulator used for boost control is a manually controlled Wilkerson regulator capable of regulating pressures from 5 to 150 PSI (gauge). This is in the intake stream above the test cell and has been procured and installed. Along with the intake regulator, a throttle actuator is located after the manually controlled regulator to control the boost pressure to finer increments during SCRE operation. This throttle valve is air actuated and controlled by a 4-20 mA signal from Veristand. The MAP sensor is an Omega product measuring 0-100 psi absolute with a 0-5V signal measured by CAS and Veristand. This has been procured and will be measured post intake surge-tank in the intake runner. The intake stream CO_2 meter was chosen to be a 5% by volume as the intake stream will never see over 5% CO_2 within the intake during normal operation. This will also be measured post-intake surge tank. IAT used for controlling the heater will be measured also in the intake runner using a K-type

thermocouple. The temperature within the intake surge tank will also be monitored using a K-type thermocouple. The intake stream pre-heater houses a Dwyer instruments flow switch which is actuated by 23-13 SCFM. The flow switch is used for protecting the heater from turning on without flow to prevent damage to the 18kW heater.

Table 4.18: Intake Sub-system Sensors and Actuators

Sensor or Actuator Name	Brand	Control	Controller	Measured With	Actuator or Sensor	System
Intake Air Heater	Tutco	1-5V Input	Veristand	N/A	Actuator	Intake
Intake Air Regulator (pressure control)	Wilkerson	Manual	N/A	Veristand	Actuator	
Intake Air Fine Control (Throttle)	Triad Controls	4-20 mA	Veristand	Veristand	Actuator	
MAP Sensor	Omega	N/A	N/A	Veristand & Mototron	Sensor	
CO2 Meter (5%) Intake	CO2 Meter .com	N/A	N/A	CO2meter .com	Sensor	
Intake Air Temperature (Surge Tank)	Temprel	N/A	N/A	Veristand	Sensor	
Intake Air Temperature (Runner)	Temprel	N/A	N/A	Veristand	Sensor	
Flow Switch	Dwyer Instruments	N/A	N/A	N/A	Sensor	

The CNG sub-system sensors and actuators are given in Table 4.19. The pressure will be measured with an Omega PXM 309 transducer, measured in both Veristand and Moto-tune. The sensor is located post dome-loaded regulator to provide the NG pressures sent to the injector. The CNG booster is used to increase the pressure from the supply pressure from 248 bar up to 340 bar using regulated compressed air. The NG fuel system also contains a solenoid used to shut off the system with a 12V on/off signal which will be controlled through Veristand. A Micro Motion CMFS010P323N2BAECZZ 4-Wire 800

Flow Sensor #4 VCO Swagelok MFD2012 capable of measuring the mass-flow of NG up to 414 bar working pressure.

Table 4.19: CNG Sub-system Sensors and Actuators

Sensor or Actuator Name	Brand	Control	Controller	Measured With	Actuator or Sensor	System
CNG Pressure PXM309-350G10V	Omega	N/A	N/A	Veristand/Moto-tune	Sensor	Natural Gas
CNG Booster	Haskel	(0-110 PSI)	Veristand & Moto-tune	Veristand	Actuator	
CNG Solenoid	Nash Fuel	12V on/off	Veristand & Moto-tune	N/A	Actuator	
Coriolis Flow Meter	Micro Motion	N/A	N/A	Veristand	Sensor	

The oil sub-system sensors and actuators is given in Table 4.20. The engine oil temperature is monitored post oil-filter with a K-type thermocouple. The oil-pressure is measured with a GP-50 omega 6.9 bar gauge pressure transducer. The engine oil will be heated with 2 Zerostart 1000-watt silicone pad heaters using 480 V test cell power.

Table 4.20: Oil Sub-system Sensors and Actuators

Sensor or Actuator Name	Brand	Control or Power	Controller	Measured With	Actuator or Sensor	System
Engine Oil Temperature	Temprel	N/A	N/A	Veristand	Sensor	Oil
Engine Oil Pressure	Omega	N/A	N/A	Veristand	Sensor	
Engine Oil Heater	Zerostart 1kW	480V	N/A	N/A	Actuator	

The purpose of each of these sub-systems is to properly control and monitor pressures, temperatures, flow, and combustion within the DI CI SCRE. Each of the sub-systems was specified to ensure the operation of the CI NG engine is achievable as well as being rated for the proper specifications required for safety of the staff operating the SCRE.

4.15 Design Boosted CNG Fuel System

The injector used for the testing of the mono-fuel DI CNG engine was supplied by Westport Fuel Systems. The injector used is modified from the HPDI 2.0 injector requiring two fuels to be sent to the injector. The fuel used for combustion, CNG, and the fluid for actuation, diesel (or Viscor). The pressures for the fuel system were specified to be between 100 and 340 bar. The APS facility has already setup a system to compress building supply natural gas up to 248 bar. The engine injector required pressures higher than the facilities could supply, so a booster was required to increase the pressures even higher. A fuel system was designed specifically for the mono-fuel DI CNG injector supplied by Westport.

The fuel system designed included many components depicted by the schematic shown in Figure 4.51. The schematic shows the fuel system being split into two portions. The top portion is the CNG fuel, while the bottom is the actuation fluid, diesel (or Viscor).

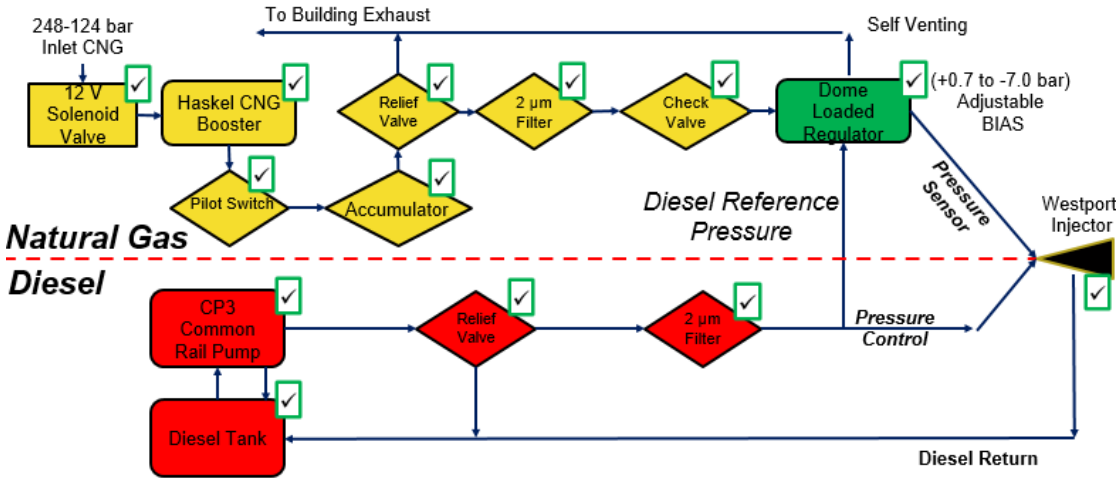

Figure 4.51: Mono-Fuel DI CNG Fuel System Schematic

The CNG system first consists of a normally closed (N.C.) solenoid valve supplied by Nash Fuel Systems. The solenoid valve allows the system to be shut-off in the case that a leak is detected. It is also designed to be normally closed, so no fuel will be sent to the injector unless 12V is applied to the solenoid. The second component in the CNG fuel system is the AGD-62 Haskel Booster. The booster can increase fuel pressures up to 620 bar (9000PSI). The Haskel Intensifier fuel pressure is controlled by compressed air. If no compressed air is present, the fuel pressure will only be as high as the CNG system supplied by the facility. The intensifier is capable of outputting well over 15 SCFM of CNG at 344 bar output with an input CNG pressure as low as 103 bar. 15 SCFM of CNG is approximately the max fuel flowrate required during operation of the single cylinder operation to reach 24 bar BMEP. The intensifier was oversized in the case that it would be used for operation on multiple cylinders in the future.

The next component for the fuel system is an air-operated pilot switch. The spring-adjusted pilot switch it was calibrated to allow the booster to shut-off at a peak sensed (CNG) pressure of 380 bar. The booster turns back on when the CNG pressure reaches 340-bar due to the hysteresis in the spring actuation of the pilot-switch. The switch was set with the minimum of the hysteresis of the system at the maximum pressure the injector is expected to be tested at. The air-pressure during the pilot-switch calibration was set at 7 bar.

The accumulator is the next component installed in the fuel system. The accumulator's purpose is to store a high pressure of CNG at 380 to 340bar to ensure the injector is always supplied with proper fuel pressure. The accumulator size was chosen to be 0.3L. Full load of the engine was expected to be 24 BMEP. The engine fuel flow rate of a single cylinder is expected to be approximately 6.5 gallons of gasoline equivalent (GGE) per hour at an engine speed of 1800 RPM at 21 bar BMEP assuming a thermal efficiency of 35%. 6.5 GGE/hr converts to 217 kW and 4.8 g/s of fuel flow with CNG having an LHV of 45 MJ/kg. Table 4.21 was created to determine at multiple load conditions, 100%, 50%, 25%, and 10% of full load the approximate time until the accumulator empties at various system pressures. At 380 bar full load, the accumulator on the engine

cart would empty in approximately 17 seconds, so the booster will be cycling almost continuously during high load applications to maintain required fuel pressures supplied to the injector. With the system pressure lowered to 120 bar, the accumulator would empty in only 7 seconds at full load conditions. As load decreases the time to empty increases as expected.

Table 4.21: Accumulator Empty Times vs. System Pressure and Engine Load

Fuel Pressure	bar	380	340	280	240	200	160	120
Density of CNG	kg/m^3	265	252	227	206.3	179.6	146.1	106.8
Mass in Tank	kg (fuel)	0.080	0.076	0.068	0.062	0.054	0.044	0.032
Seconds Until Empty	100% load	17	16	14	13	11	9	7
	50 % Load	33	31	28	26	22	18	13
	25% load	66	63	57	51	45	36	27
	10 % load	165	157	141	129	112	91	67

The next component in the natural gas system is the relief valve. The relief valve has the purpose of allowing excess pressure to escape from the system in the case that the booster overshoots the required pressure. Theoretically, the relief valve should never be reached as the pilot switch shuts the booster off at 380 bar, but it is installed as a safety in the case that the booster fails to stop while increasing pressure. The relief valve was set at 410 bar. The rating of the lines is higher than the relief valve set pressure, and the rating of the stainless-steel tubing was taken into consideration when setting the spring pressure for relief valve with a working pressure of 448 bar.

A 2-micron filter was then installed after the relief valve to ensure that no particles larger than 2-micron would make it to the injector as this could damage the injector. The filter supplied by Swagelok is equipped with 3/8 compression fittings for easy installation into the system. After the 2-micron filter is a check-valve also supplied by Swagelok with 3/8 compression fittings allowing flow in only one direction. The purpose of the check valve is to ensure no backflow if a leak occurs early in the system.

The final part of the CNG fuel system is the dome loaded regulator. The purpose of the dome loaded regulator is to regulate the outlet CNG pressure to the injector based upon the diesel reference pressure. The dome loaded regulator allows for an adjustable bias to be set to the CNG side output with respect to the diesel reference pressure from +0.7 bar

(above) the diesel pressure to -7.0 bar (below) diesel pressure. The dome loaded regulator was adjusted to the -7.0 bar bias during initial testing. The CNG should remain below diesel pressure to ensure no CNG flows into the diesel portion of the fuel system. When the diesel pressure is decreased, the dome loaded regulator vents the excess pressure on the CNG outlet side to atmosphere out of the APS facility. The dome loaded regulator was purchased through Smith/Galloup Instrument group and is a Tescom product. Figure 4.52 shows the installed Mono-Fuel CNG fuel system up to the dome loaded regulator. The fuel system is installed on the SCRE cart below the electrical heater control box.

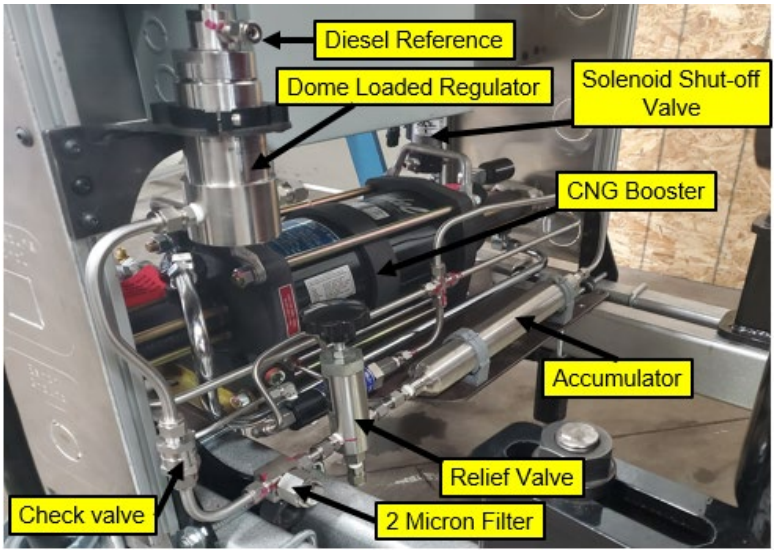

Figure 4.52: Mono-Fuel DI CNG Fuel System Installed

4.16 Diesel Support Fuel System

As shown in Figure 4.51, the CNG fuel system is supported by a diesel control system. The actuating fluid is used to actuate and drive the injector mechanical actuation to allow the CNG to flow into the combustion chamber while also aiding as a control (reference) pressure for the CNG. The diesel system was built as a stand-alone fuel system capable of supplying pressures up to 414 bar working pressure, limited by the hydraulic line connecting the stand-alone cart to the ISX SCRE cart. Figure 4.53 shows the stand-alone diesel fuel cart. The cart consists of a 5-gallon aluminum vented tank, a low-pressure diesel filter, a high-pressure 2-micron filter, relief valve, and a hydraulic hose to allow coupling to the SCRE cart. The Bosch CP3 pump typically found on MD diesel engines

was retrofitted with a 3 HP motor to drive the pump. The CP3 pump is capable of outputting 2000 bar but will be controlled to pressures between 50 to 340 bar with the use of a ttl signal from the Mototron ECM. The CP3 pump alters the pressure based upon the fuel control actuator (FCA) duty cycle ttl signal being sent to the diesel cart. The duty cycle used to drive the CP3 pump was tested at 185 Hz. with a range of duty cycles from 78 to 95 percent. As the duty cycle is increased the diesel pressure decreases due to the FCA allowing more fuel to by-pass the high-pressure system. While if the percent duty cycle is decreased the FCA closes off the by-pass portion of the pump and the pressure out increases.

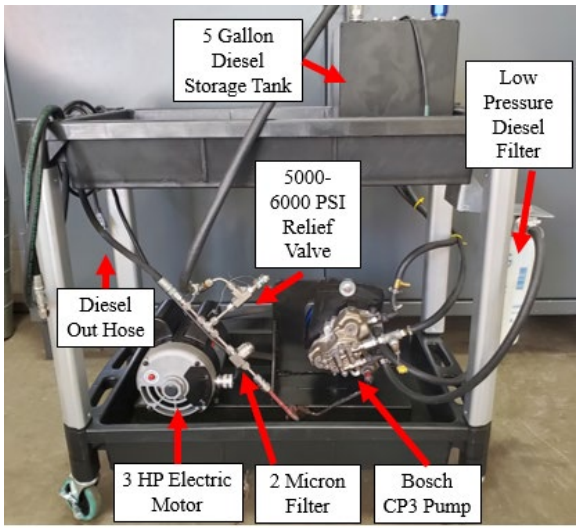

Figure 4.53: Diesel Stand-Alone Fuel Cart

In conclusion each of the systems were designed and developed to achieve CI of a mono-fueled NG SCRE. The engine cart and mounting system was developed for the 15L ISX base engine. The driveshaft and inertia coupling, testing, and calculations were completed to determine the best fit for engine operation to avoid first-order natural frequencies. The intake, exhaust, and EGR system were developed to maintain proper flow within the SCRE for safe operation while monitoring specific pressures and temperatures and CO_2 measurements for SCRE operation. A heater was selected and procured for all CR options to achieve CI of NG at all load cases. The cylinder deactivation was also completed to realize SCRE operation. The sensors and actuators to control each system

were selected and procured along with an ECM to control the system. Finally, the fuel system, both CNG and diesel sub-systems were also developed to control the NG pressures and flow for DI of the mono-fueled injector supplied by Westport. While the engine is not yet operational, the final build is in progress as each of the sub-systems are being reassembled and this is shown in Figure 4.54.

Figure 4.54: Final Build Current Status

5 Final Chapter

5.1 Summary and Conclusions

First, a literature review was completed for the background of the project including information on basic compression ignition engines, benefits of NG, prior work on CI of NG within CVCC's and internal combustion engines, and current DI NG injector technology. Each of the portions of literature review were aimed at understanding the benefits of and prior work applicable to the DI CI CNG SCRE project.

Secondly, modeling was conducted using 0D thermodynamic analysis to understand the required IAT's at various CR to achieve required EOC temperatures for auto-ignition of NG within reasonable ID limits based upon the literature review conducted. A TPA model was created using GT-Power 1-D simulation software and calibrated to data from a 3D CFD model that incorporates a chemical kinetic combustion provided by Westport. This model was used to calibrate heat transfer coefficients and aid in the selection of intake and exhaust surge tank sizing. A third model was created and calibrated using GT-powers DI-Pulse predictive combustion model. The predictive combustion model was used to first calibrate the AT multiplier specifically for the auto-ignition of NG, secondly calibrate all other DI-Pulse multipliers, and finally sweep the CR, IAT for three engine modes. This model was used to understand the impacts of various CR's at various IAT's on combustion metrics and engine performance. The calibrated model was also used to determine the benefits of increasing valve overlap on the SCRE. The modeling completed was crucial in the design of the SCRE, specifically, the surge tanks, intake air heater, and piston CR's chosen for the CI of NG.

Third, the experimental work completed was required to achieve the objective of an operational SCRE using DI CI with NG. The work started with the initial purchase of the SCRE base ISX 15L. The engine was then carted for operation at the APS labs facility under typical procedure with the assistance of the APS faculty. An engine driveshaft adapter was created for connection to the MSI driveshafts and AC dyno used for engine testing. A test of driveshaft choices was completed to determine the engine inertia and the

proper driveshaft choice for engine operation. An interface panel was created and assembled to connect to the various APS labs facility controls, air supply, electrical power, coolant, diesel, and NG systems. Intake, exhaust, and EGR plumbing was completed for the SCRE including the design and procurement of surge tanks to aid in several factors when operating the SCRE. A moto-hawk stand-alone ECM was chosen, procured, and wired for the control of the SCRE based upon prior knowledge and functionality of the controller. An increased CR plan was completed including piston bowl design, thermal studies completed by Westport based on the initial CAD modeling for aftermarket aluminum pistons. Multiple pistons were designed, analyzed, and procured for a wide variety of CR selections when operating the SCRE. An intake air heater was selected procured and implemented based upon the flow and temperature requirements for the lowest CR required to achieve auto-ignition of NG within the SCRE. The cylinder head was machined, and transducer sleeves were designed and implemented to measure both cylinder pressure and heat flux within the SCRE. The engine components including valve and injector rockers were removed and replaced with rocker shaft covers to achieve cylinder deactivation on the first five cylinders within the base 15L engine. The engine cam-timing and piston to valve clearance was measured to understand the limits currently on the engine with regards to piston to valve interference. With a better understanding of the range of valve lift prior to contact with the piston during operation, a cam timing sweep was conducted to determine possible benefits from increased valve overlap. A high-pressure NG fuel system was designed and implemented to meet the requirements for the Westport fuel injector including pressure range, and controlled bias on the SCRE cart, with the ability to connect to the APS facility fuel supply. A diesel stand-alone cart was also designed and implemented to control the NG pressure fed to the injector.

While the engine is currently in the final stages of the build including the install of the aftermarket pistons, and installing the head onto the engine, the project is a success from the design aspect. Multiple software packages (i.e. 0D, 1D, 3D CAD) were used in the design and procurement of multiple parts required for operation of the DI CI SCRE.

Many parts for various systems were designed, modeled, procured, modified, individually tested, and installed, that were necessary for proper operation, control, and analysis of the HD DI CI NG SCRE.

5.2 Future Work

Future work required on this project includes finalizing the build and shakedown of the SCRE. While many of the components have been tested individually, the engine is not yet operational. There are a few various sensors and actuators that are yet to be installed including the actuator for the EGR valve. All the parts have been procured, but the mounting for the linear actuator has not been finished. Secondly, the plumbing for the various pressure measurements within the intake, and exhaust system needs to be finalized. The exhaust system, post-back-pressure valve needs to be manufactured and welded together including a step up from 2-inch to 4-inch exhaust pipe. The final routing of the CNG and diesel through the head needs to be completed. All the high-pressure stainless-steel tubing is procured and the holes through the head where the plumbing will pass through is completed, but the routing is currently still in progress. The wiring into the ECM for the O_2 sensor is in progress as well as the wiring for the NO_x sensor into Veristand. The wiring for the MAP sensor into the ECM and Veristand is also still yet to be completed. The transducer sleeves have been installed, but the transducers themselves still need to be installed into the sleeves prior to operation. Lastly, the fuel injector needs to be installed and tested to ensure the seals within the injector bore are adequate while motoring the engine and monitoring cylinder pressure vs. crank angle.

The initial testing will be conducted over the next several weeks as the aftermarket pistons have arrived, and pin-bores have been finished. The final build is currently underway and will be achieved by the end of the year 2020. While it is unfortunate that the testing will not be included in my thesis, all the systems required to achieve CI of NG within the SCRE are procured and in place.

Future work for the next several years once initial shakedown is completed will entail using the different pistons that have been designed and procured. I would urge to ensure

that proper precaution is taken when operating this HD SCRE using DI CI of NG due to the auto-ignition characteristics. Make sure that the low limit levels are well understood for each of the CR's used during operation and monitor IAT and coefficient of variance of IMEP consistently while testing. My recommendation is to also install the proper flow measurement devices in the intake air stream for both the boosted and N/A operation of the engine as these have currently been overlooked during the project. While the initial research into the background of piston/head coatings has been completed, getting a piston and valves coated to determine the actual benefits (i.e. heat transfer) is yet to be completed. One of the pistons should be sent out for coating and tested vs. a non-coated piston to measure both changes in heat transfer from the Medtherm transducer, and the difference in measured cylinder pressure at various control points for the engine.

Another portion of work to be completed is the calculation of the compression work required to achieve NG pressures required for operation. Typically, NG can be held within storage tanks on vehicles up to 248 bar, but the operating system of the injector used within the project requires pressures up to 340 bar. The work required to compress this fuel within a vehicle is important to understand the impacts on the BSFC. Calculating the required work being completed by the compressed air from the facility to compress the NG from pressures from 100-248 bar up to the peak pressures of 340 bar is important in understanding what would be required for a mechanical compressor system on the vehicle and its effect on BSFC.

As for the cam development, multiple simulations have been completed, but further optimization should be conducted at several speed load operating points to determine the benefit of either increased or decreased valve overlap on temperatures at TDC and its effect on internal trapped residuals and the effects on NG auto-ignition. The cam development mechanically also must be completed either by getting a new camshaft ground, allowing for insertable cam lobes for various lobe profiles, or designing a VVT system which would be difficult considering both lobes are on the same camshaft.

As for the 3-year engine specific goals of BTE and emissions objectives, my suggestion is to conduct the baseline testing and determine indicated thermal efficiency of the current engine with 23.5:1 CR. From there, determine which routes are required to increase these values to meet the 48% BTE including the TBC, higher CR, and valve overlap strategies. The current GT-power model developed should be re-calibrated to measured engine data and then the model parameters can be optimized to determine the maximum potential of the DI CI mono-fueled NG SCRE at various CR's to increase the efficiency from the initial data obtained.

6 Reference List

1. U.S. Department of Energy's Office of Energy Efficiency and Renewable Energy's Vehicle Technologies Office, 2020, "U.S. Department of Energy Energy Efficiency & Renewable Energy Alternative Fuels Data Center" from https://afdc.energy.gov/fuels/prices.html.
2. Kang, J., Thomson, A. "Gas Technology and Innovation for a Sustainable Future" International Gas Union. from https://igu.org/resources/
3. Nieman, D.E., Morris, A.P., Miwa, J.T., and Denton, B.D., "Methods of Improving Combustion Efficiency in a High-Efficiency, Lean Burn Dual-Fuel Heavy-Duty Engine," SAE Technical Paper 2019-01-0032, 2019, doi:10.4271/2019-01-0032.
4. Neely, G., Florea, R., Miwa, J., and Abidin, Z., "Efficiency and Emissions Characteristics of Partially Premixed Dual-Fuel Combustion by Co-Direct Injection of NG and Diesel Fuel (DI2) - Part 2," SAE Technical Paper 2017-01-0766, 2017, doi:10.4271/2017-01-0766.
5. Mumford, David, and Sandeep Munshi. "Fuel Injection Valve and Method for Co-Injecting a Liquid and a Gaseous Fuel into the Combustion Chamber of an Internal Combustion Engine". 29 Dec. 2009.
6. Faghani, E., Kheirkhah, P., Mabson, C., McTaggart-Cowan, G. et al., "Effect of Injection Strategies on Emissions from a Pilot-Ignited Direct-Injection Natural-Gas Engine- Part I: Late Post Injection," SAE Technical Paper 2017-01-0774, 2017, doi:10.4271/2017-01-0774.
7. Faghani, E., Kheirkhah, P., Mabson, C., McTaggart-Cowan, G. et al., "Effect of Injection Strategies on Emissions from a Pilot-Ignited Direct-Injection Natural-Gas Engine- Part II: Slightly Premixed Combustion," SAE Technical Paper 2017-01-0763, 2017, doi:10.4271/2017-01-0763.
8. Weichai Westport Secures Chinese Certification for WP12 Natural Gas Engine Powered by HPDI 2.0. (2020, September 18). Retrieved November 16, 2020, from https://wfsinc.com/news-releases/2020/weichai-westport-secures-chinese-certification-for-wp12-natural-gas-engine-powered-by-hpdi-2.0
9. Mohr H, Baufeld T (2013) Improvement of dual—fuel engine technology for current and future applications. CIMAC paper no. 412, CIMAC congress, Shanghai, China
10. Genchi, G. and Pipitone, E., "Octane Rating of Natural Gas-Gasoline Mixtures on CFR Engine," SAE Int. J. Fuels Lubr. 7(3):1041-1049, 2014, https://doi.org/10.4271/2014-01-9081.
11. Naber, J., Siebers, D., Caton, J., Westbrook, C. et al., "Natural Gas Autoignition Under Diesel Conditions: Experiments and Chemical Kinetic Modeling," SAE Technical Paper 942034, 1994, https://doi.org/10.4271/942034.
12. USPTO, 2000. "National Inventors Hall of Fame: Rudolf Diesel", US Patent and Trademark Office, Inventure Place, https://www.invent.org/inductees/rudolf-diesel

13. Stanton, D.W., “Systematic Development of Highly Efficient and Clean Engines to Meet Future Commercial Vehicle Greenhouse Gas Regulations,” SAE Int. J. Engines 6(3):1395-1480, 2013, doi:10.4271/2013-01-2421.
14. Mohr, D., Shipp, T., and Lu, X., “The Thermodynamic Design, Analysis and Test of Cummins’ Supertruck 2 50% Brake Thermal Efficiency Engine System,” SAE Technical Paper 2019-01-0247, 2019, doi:10.4271/2019-01-0247.
15. Heywood, J.B., Internal Combustion Engine Fundamentals, McGraw-Hill, 1988.
16. Tuner, M., "Review and Benchmarking of Alternative Fuels in Conventional and Advanced Engine Concepts with Emphasis on Efficiency, CO2, and Regulated Emissions," SAE Technical Paper 2016-01-0882, 2016, doi:10.4271/2016-01-0882.
17. Yanowitz, J., Ratcliff, M., McCormick, R., Taylor, J., & Murphy, M. (2017). Compendium of Experimental Cetane Numbers (pp. 1-71, Rep. No. NREL/TP-5400-67585). Golden, Colorado: National Renewable Energy Laboratory. doi: https://www.nrel.gov/docs/fy17osti/67585.pdf
18. United States: Diesel Fuel: Certification Diesel Fuel. (n.d.). Retrieved July 18, 2019, from https://dieselnet.com/standards//us/fuel_certification.php
19. Frequently Asked Questions (FAQs) - U.S. Energy Information Administration (EIA). (2020, June 17). Retrieved November 16, 2020, from https://www.eia.gov/tools/faqs/faq.php?id=73
20. Pischingcr, R., and Canellicri, W.: "Combustion System Parameters and Their Effect upon Diesel Engine Exhaust Emissions," SAE paper 720756, SAE Trans., vol. 81, 1972.
21. Ferguson, C. R., & Kirkpatrick, A. (2016). 7.4 Combustion in Compression Ignition Engines. In Internal combustion engines: Applied thermosciences (p. 220). Chichester, West Sussex, United Kingdom: John Wiley & Sons.Liss, W.E., Thrasher, W.H., Steinmetz, G.F., Chowdiah, P., and Attari, A., "Variability of Natural Gas Composition in Select Major Metropolitan Areas of the United States," GRI Report GRI-9210123, March 1992.
22. Frequently Asked Questions (FAQs) - U.S. Energy Information Administration (EIA). (2020, June 17). Retrieved November 16, 2020, from https://www.eia.gov/tools/faqs/faq.php?id=73
23. Liss, W.E. and Thrasher, W.H., "Natural Gas as a Stationary Engine and Vehicular Fuel," SAE Paper 912364, International Fuel and Lubricants Meeting, Oct. 1991.
24. Liss, W.E., Thrasher, W.H., Steinmetz, G.F., Chowdiah, P., and Attari, A., "Variability of Natural Gas Composition in Select Major Metropolitan Areas of the United States," GRI report GRI-9210123, March 1992.
25. Oliver, N. and Edwards, C., "Realizing Stoichiometric, Natural Gas-Fueled Combustion in Diesel Engines," SAE Technical Paper 2018-01-1148, 2018, https://doi.org/10.4271/2018-01-1148.
26. Agarwal, A. and Assanis, D., "Multi-Dimensional Modeling of Natural Gas Ignition under Compression Ignition Conditions Using Detailed Chemistry," SAE Technical Paper 980136, 1998, https://doi.org/10.4271/980136.

27. Diesel Fuels Technical Review. (2007). Retrieved November 16, 2020, from https://www.chevron.com/-/media/chevron/operations/documents/diesel-fuel-tech-review.pdf
28. THE CALIFORNIA DIESEL FUEL REGULATIONS, https://ww2.arb.ca.gov/sites/default/files/2020-05/unofficial_diesel_regs_3-11-19.pdf (2014)
29. Fraser, R., Siebers, D., and Edwards, C., "Autoignition of Methane and Natural Gas in a Simulated Diesel Environment," SAE Technical Paper 910227, 1991, https://doi.org/10.4271/910227.
30. Araki, M., Dong, H., Obokata, T., Shiga, S. et al., "Characteristics of CNG Direct Injection with Auto-Ignition," SAE Technical Paper 2005-26-358, 2005, https://doi.org/10.4271/2005-26-358.
31. McTaggart-Cowan, G, Huang, J, Turcios, M, Singh, A, & Munshi, S. "Evaluation of a Hot-Surface Ignition System for a Direct-Injection of Natural Gas Engine." Proceedings of the ASME 2018 Internal Combustion Engine Division Fall Technical Conference. Volume 1: Large Bore Engines; Fuels; Advanced Combustion. San Diego, California, USA. November 4–7, 2018. V001T03A027. ASME. https://doi.org/10.1115/ICEF2018-9734
32. Goto, S., Lee, D., Wakao, Y., Honma, H., Mori, M., Akasaka, Y., . . . Konno, M. (1999). Development of an LPG DI Diesel Engine Using Cetane Number Enhancing Additives. SAE Technical Paper Series. doi:10.4271/1999-01-3602
33. Ouellette, P.; Goudie, D.; McTaggart-Cowan, G., "Progress in the Development of Natural Gas High Pressure Direct Injection for EuroVI Heavy Duty Trucks", Proceedings of ATZ Live Internationaler Motorenkongress 2016
34. Mumford, D., Goudie, D., and Saunders, J., "Potential and Challenges of HPDI," SAE Technical Paper 2017-01-1928, 2017, https://doi.org/10.4271/2017-01-1928
35. Chala, G., Aziz, A. A., & Hagos, F. (2018). Natural Gas Engine Technologies: Challenges and Energy Sustainability Issue. Energies, 11(11), 2934. doi:10.3390/en11112934
36. Landi Renzo. EPA Approval of Dual Fuel CNG System for Detroit Diesel 12.7l s60 Engine; Landi Renzo USA: Torrance, CA, USA, 2013.
37. Nylund, N., Karvonen, V., Kuutti, H., and Laurikko, J., "Comparison of Diesel and Natural Gas Bus Performance," SAE Technical Paper 2014-01-2432, 2014, doi:10.4271/2014-01-2432.
38. Naber, J., Munshi, S., "A Compression Ignition Mono-Fueled NG High-Efficiency, High-Output Engine for Medium and Heavy-Duty Applications", National Renewable Energy Laboratory Managed and Operated by the Alliance for Sustainable Energy, LLC Request for Proposals (RFP) Number RHQ-8-82305 "Natural Gas Engine and Vehicles Research and Development – Category B", Retrieved April 15, 2019, from: Email Naber, J.
39. Kumar, P., Pei, Y., Traver, M., and Watson, J., "System Level 1-D Analysis of an Air-System for a Heavy-Duty Gasoline Compression Ignition Engine," SAE Technical Paper 2019-01-0240, 2019, doi:10.4271/2019-01-0240.

40. Air Compressor Tanks. (n.d.). Retrieved November 18, 2020, from https://www.globalindustrial.com/g/pneumatics/air-compressors/air-compressor-tanks-parts-acc/small-air-receivers-surge-tanks-101673
41. McTaggart-Cowan, G., Mann, K., Huang, J., Singh, A. et al., "Direct Injection of Natural Gas at up to 600 Bar in a Pilot-Ignited Heavy-Duty Engine," SAE Int. J. Engines 8(3):2015, doi:10.4271/2015-01-0865.
42. Douville, B., Ouellette, P., Touchette, A., Ursu, B., Performance and Emissions of a Two-Stroke Engine Fueled Using High-Pressure Direct Injection of Natural Gas, SAE Paper 981160, 1998, https://doi.org/10.4271/981160.
43. Senachin, A.p., et al. "Simulation of Fuel Ignition Delay in Diesel Engines with Various Fuel Feeding Systems." *Procedia Engineering*, vol. 150, 2016, pp. 190–203., doi:10.1016/j.proeng.2016.06.746.
44. United States Environmental Protection Agency. 2017. "Vehicle Weight Classifications for the Emission Standards Reference Guide" from https://www.epa.gov/emission-standards-reference-guide/vehicle-weight-classifications-emission-standards-reference-guide
45. Cummins Inc. 2007. "ISX for Heavy-Duty Truck (EPA 07)" from https://www.cummins.com/engines/isx-epa-07?v=581&application=Heavy-Duty%20Truck?v=581&application=Heavy-Duty%20Truck
46. Huco Altra Industrial Motion. 2019. "Selecting for Torsional Stiffness" from https://www.huco.com/design-guide/selecting-for-torsional-stiffness
47. Cummins Inc. 2007. "Engine Data Sheet" from http://www.martinenergygroup.com/inventory/wp-content/uploads/2017/01/QSX15-G9-Engine-Data-Sheet-FR1034900.pdf
48. Atlas Steels. 2017. "Pressure Rating Tables for Stainless Steel Pipe" from http://www.atlassteels.com.au/documents/St_St_Pipe_Pressure_Rating_Charts_rev_Jan_2017.pdf
49. ASME. 2013. "Pipe Flanges and Flanged Fittings"
50. from https://www.unitrove.com/engineering/tools/gas/natural-gas-density

7 Appendices

A.1 EES 0-D Analysis code

MW_{air} [kg/kmol] = **MolarMass** (Air)

$MW_{methane}$ [kg/kmol] = **MolarMass** (Methane)

$$moles_{air}\ [kmol/cycle] = \frac{ma\ [kg/cycle]}{MW_{air}\ [kg/kmol]}$$

$$moles_{methane}\ [kmol/cycle] = \frac{mf\ [kg/cycle]}{MW_{methane}\ [kg/kmol]}$$

T_{1f} [F] = (T_1 [K] – 273) · 9 / 5 + 32

v_4 [mm3] = $2.5 \cdot 10^6$ [mm³]

v_1 [mm³] = v_4 [mm3]

$$CR = \frac{v_1\ [mm^3]}{v_2\ [mm^3]}$$

v_{3a} [mm³] = v_2 [mm³]

V_{disp} [mm³] = v_4 [mm3]

T_{amb} [K] = 293 [K]

ρ [kg/m³] = ρ(Air, T = T_1 [K], P = P_1 [kPa])

ρ_{std} [kg/m³] = ρ(Air, T = T_{amb} [K], P = 100)

$$\rho_{used}\ [kg/mm^3] = \frac{\rho\ [kg/m^3]}{1 \cdot 10^9}$$

$$ma\ [kg/cycle] = V_{disp}\ [mm^3] \cdot \rho_{used}\ [kg/mm^3]$$

$$n = 2$$

$$rpm\ [rpm] = 2200$$

$$cpm = \frac{rpm\ [rpm]}{n}$$

$$mdota\ [kg/min] = ma\ [kg/cycle] \cdot cpm$$

$$mdotas\ [kg/s] = \frac{mdota\ [kg/min]}{60}$$

$$mdotf\ [kg/min] = \frac{mdota\ [kg/min]}{afr\ [\%]}$$

$$mdota6\ [kg/min] = mdota\ [kg/min] \cdot 6$$

$$airvolumeflow\ [m3/min] = \frac{mdota\ [kg/min]}{\rho\ [kg/m^3]}$$

$$volairflow_{sec}\ [m3/sec] = \frac{airvolumeflow\ [m3/min]}{60\ [m^3/sec]}$$

$$DT = T_1\ [K] - T_{amb}\ [K]$$

$$cpair\ [kj/kg \cdot C] = 1.006\ [kj/kg \cdot C]$$

$$hs\ [kW] = cpair\ [kj/kg \cdot C] \cdot mdotas\ [kg/s] \cdot \frac{DT}{0.8}$$

$$afr_{stoich} = 17.23$$

$$afr\ [\%] = afr_{stoich} \cdot \lambda\ [\%]$$

$$Q_{LHV}\ [kJ/kg] = 50000\ [kJ/kg]$$

$$mf\ [kg/cycle] = \frac{ma\ [kg/cycle]}{afr\ [\%]}$$

$$m_{mix}\ [kg] = ma\ [kg/cycle] + mf\ [kg/cycle]$$

$$Q_{star}\ [kJ] = Q_{LHV}\ [kJ/kg] \cdot \frac{ma\ [kg/cycle]}{m_{mix}\ [kg]}$$

$$\gamma = \frac{cp_{mix}}{cv_{mix}\ [kJ/kg]}$$

$$t_{mid} = T_1\ [K] + 315$$

$$cp_{mix} = \mathbf{Cp}\ (Air\ ,\ T = t_{mid}\ )$$

$$t_{mid} = T_1\ [K] + 315$$

$$cp_{mix} = \mathbf{Cp}\ (\text{Air}, T = t_{mid})$$

$$cv_{mix}\ [kJ/kg] = \mathbf{Cv}\ (\text{Air}, T = t_{mid})$$

$$cp_{cv,ratio} = \frac{cp_{mix}}{cv_{mix}\ [kJ/kg]}$$

$$R = cp_{mix} - cv_{mix}\ [kJ/kg]$$

$$cp_{mix} \cdot \mathbf{ln}\left[\frac{T_2\ [K]}{T_1\ [K]}\right] = R \cdot \mathbf{ln}\left[\frac{P_2\ [kPa]}{P_1\ [kPa]}\right]$$

$$\frac{P_2\ [kPa]}{P_1\ [kPa]} = \left[\frac{v_1\ [mm^3]}{v_2\ [mm^3]}\right]^{\gamma}$$

$$W_{12}\ [kJ] = (ma\ [kg/cycle] + mf\ [kg/cycle]) \cdot cv_{mix}\ [kJ/kg] \cdot (T_1\ [K] - T_2\ [K])$$

$$mf\ [kg/cycle] \cdot f\ [\%] \cdot Q_{LHV}\ [kJ/kg] = m_{mix}\ [kg] \cdot cv_{mix}\ [kJ/kg] \cdot (T_{3a}\ [K] - T_2\ [K])$$

$$\frac{P_2\ [kPa]}{T_2\ [K]} = \frac{P_{3a}\ [kPa]}{T_{3a}\ [K]}$$

$$\alpha = \frac{P_{3a}\ [kPa]}{P_2\ [kPa]}$$

$$P_{3a}\ [kPa] = P_{3b}\ [kPa]$$

$$\beta = \frac{V_{3b}\ [mm^3]}{v_{3a}\ [mm^3]}$$

$$T_{3b}\ [K] = \beta \cdot T_{3a}\ [K]$$

$$mf\ [kg/cycle] \cdot (1 - f\ [\%]) \cdot Q_{LHV}\ [kJ/kg] = m_{mix}\ [kg] \cdot cp_{mix} \cdot (T_{3b}\ [K] - T_{3a}\ [K])$$

$$W_{3a3b}\ [kJ] = P_{3b}\ [kPa] \cdot (V_{3b}\ [mm^3] - v_{3a}\ [mm^3]) \cdot 10^{-9}$$

$$\frac{T_4\ [K]}{T_{3b}\ [K]} = \left[\frac{P_4\ [kPa]}{P_{3b}\ [kPa]}\right]^{\left[1 - \frac{1}{\gamma}\right]}$$

$$\frac{P_4\ [kPa]}{P_{3b}\ [kPa]} = \left[\frac{V_{3b}\ [mm^3]}{v_4\ [mm3]}\right]^{\gamma}$$

$$W_{34}\ [kJ] = m_{mix}\ [kg] \cdot cv_{mix}\ [kJ/kg] \cdot (T_{3b}\ [K] - T_4\ [K])$$

$$IMEP_{CV}\ [bar] = \frac{W_{12}\ [kJ] + W_{3a3b}\ [kJ] + W_{34}\ [kJ]}{V_{disp}\ [mm^3] \cdot 10^{-7}}$$

$$W_{total}\ [kJ] = IMEP_{CV}\ [bar] \cdot V_{disp}\ [mm^3] \cdot 10^{-7}$$

$$\eta_{cv}\ [\%] = \left[\frac{W_{12}\ [kJ] + W_{3a3b}\ [kJ] + W_{34}\ [kJ]}{mf\ [kg/cycle] \cdot Q_{LHV}\ [kJ/kg]}\right] \cdot 100$$

SOLUTION

Unit Settings: SI K kPa kJ mass deg

(Table 2, Run 35)

afr = 43.08 [%]

airvolumeflow = 2.75 [m3/min]

β = 1.614

cpm = 1100

cp_{mix} = 1.06

cv_{mix} = 0.7729 [kJ/kg]

η_{cv} = 67.7 [%]

γ = 1.371

$IMEP_{cv}$ = 147.5 [bar]

ma = 0.04692 [kg/cycle]

mdota6 = 309.7 [kg/min]

mdotf = 1.198 [kg/min]

$moles_{air}$ = 0.00162 [kmol/cycle]

MW_{air} = 28.97 [kg/kmol] {28.97 [kg/kmol]}

m_{mix} = 0.04801 [kg]

P_1 = 1742 [kPa]

P_{3a} = 202699 [kPa]

P_4 = 4258 [kPa]

Q_{star} = 48866 [kJ]

ρ = 18.77 [kg/m^3]

ρ_{used} = 1.877E-08 [kg/mm^3]

T_1 = 323.4 [K]

T_2 = 1100 [K]

T_{3b} = 2250 [K]

T_{amb} = 293 [K]

$volairflow_{sec}$ = 0.04583 [m3/sec]

v_2 = 92593 [mm^3]

V_{3b} = 149483 [mm^3]

V_{disp} = 2.500E+06 [mm^3]

W_{34} = 54.15 [kJ]

W_{total} = 36.87 [kJ]

afr_{stoich} = 17.23

α = 1.267

cpair = 1.006 [kj/kg-C]

$cp_{cv,ratio}$ = 1.371

CR = 27

DT = 30.44

f = 0.2 [%]

hs = 32.93 [kW]

λ = 2.5 [%]

mdota = 51.61 [kg/min]

mdotas = 0.8602 [kg/s]

mf = 0.001089 [kg/cycle]

$moles_{methane}$ = 0.0000679 [kmol/cycle]

$MW_{methane}$ = 16.04 [kg/kmol]

n = 2

P_2 = 160000 [kPa]

P_{3b} = 202699 [kPa]

Q_{LHV} = 50000 [kJ/kg]

R = 0.287

ρ_{std} = 1.189 [kg/m^3]

rpm = 2200 [rpm]

T_{1f} = 122.8 [F]

T_{3a} = 1394 [K]

T_4 = 790.3 [K]

t_{mid} = 638.4

v_1 = 2.500E+06 [mm^3]

v_{3a} = 92593 [mm^3]

v_4 = 2.500E+06 [mm^3]

W_{12} = -28.81 [kJ]

W_{3a3b} = 11.53 [kJ]

No unit problems were detected. (29 disabled)

A.2 Surge Tank Sweep

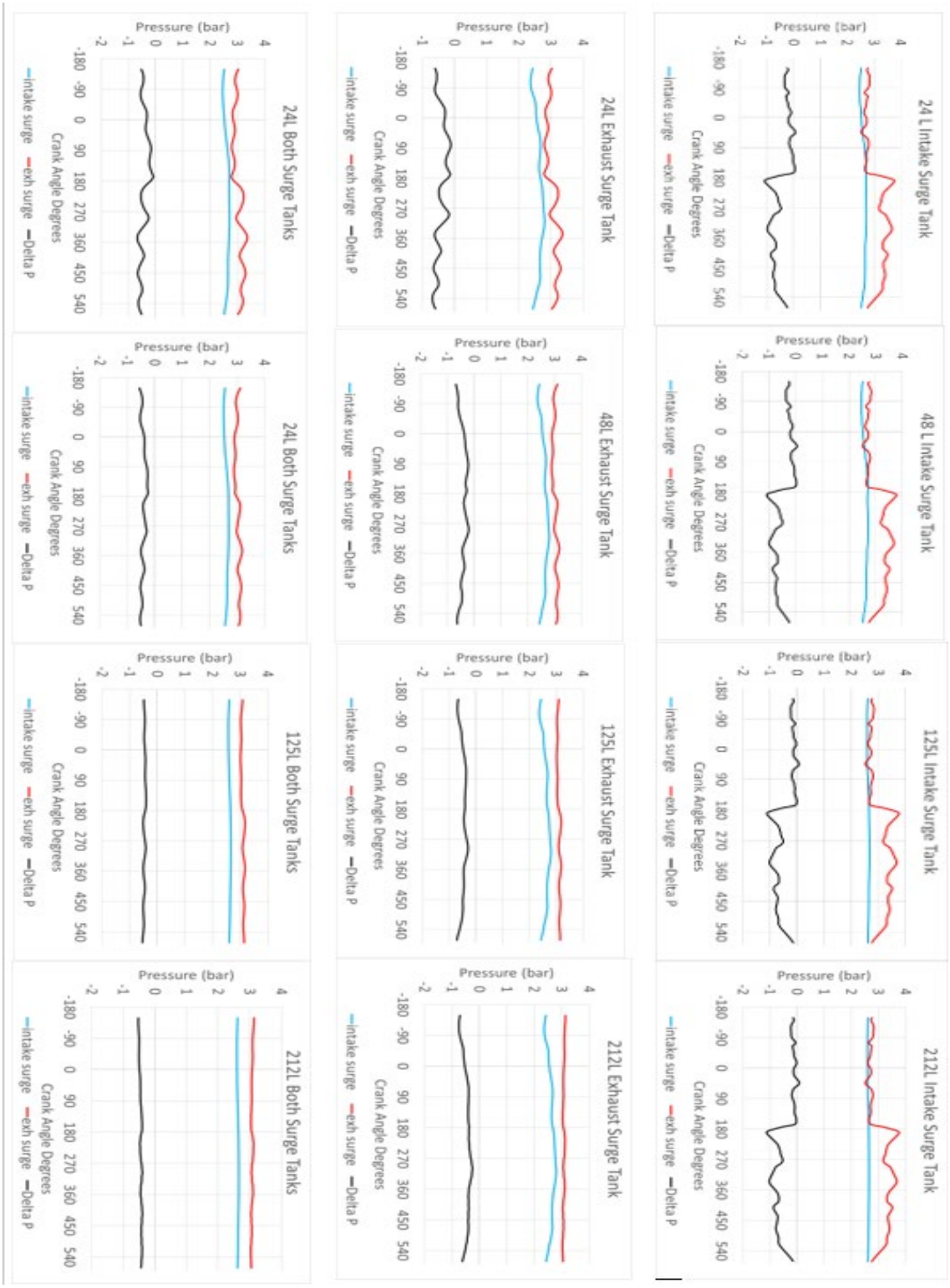

7.1: GT-Power Surge Tank Sweep (Delta Pressure Individual)

A.3 GT-Power Modeling

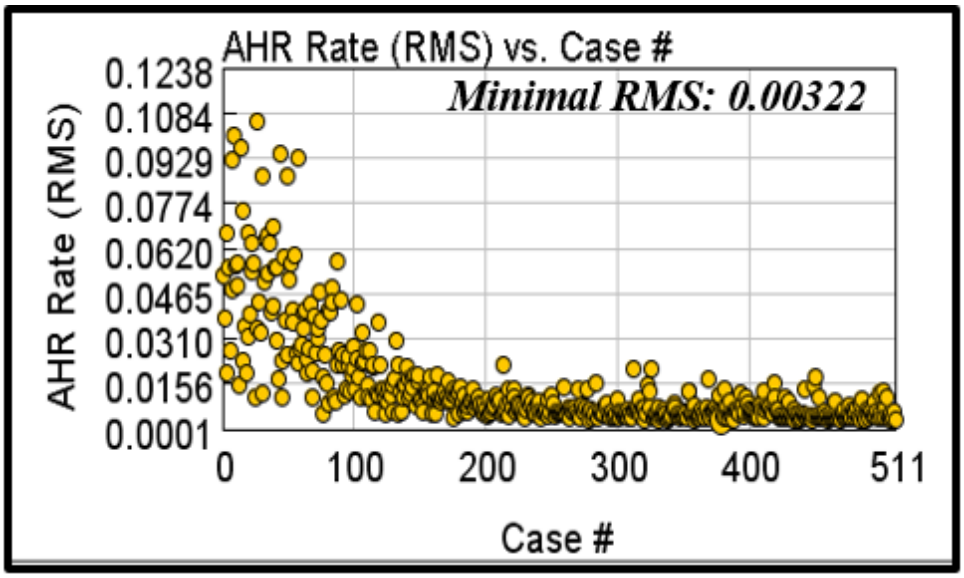

7.2: AHR Rate RMS vs. Case # Mode A50

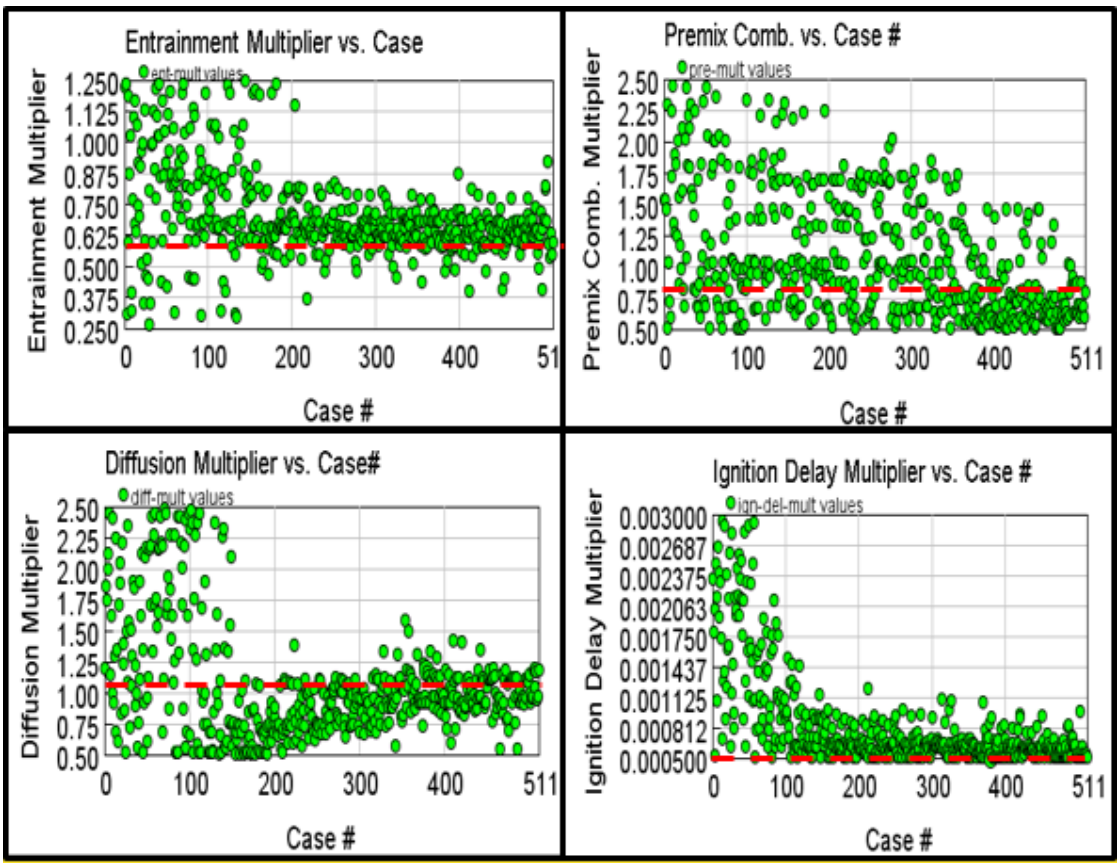

7.3: Individual Multiplier vs. Case Number Mode A50

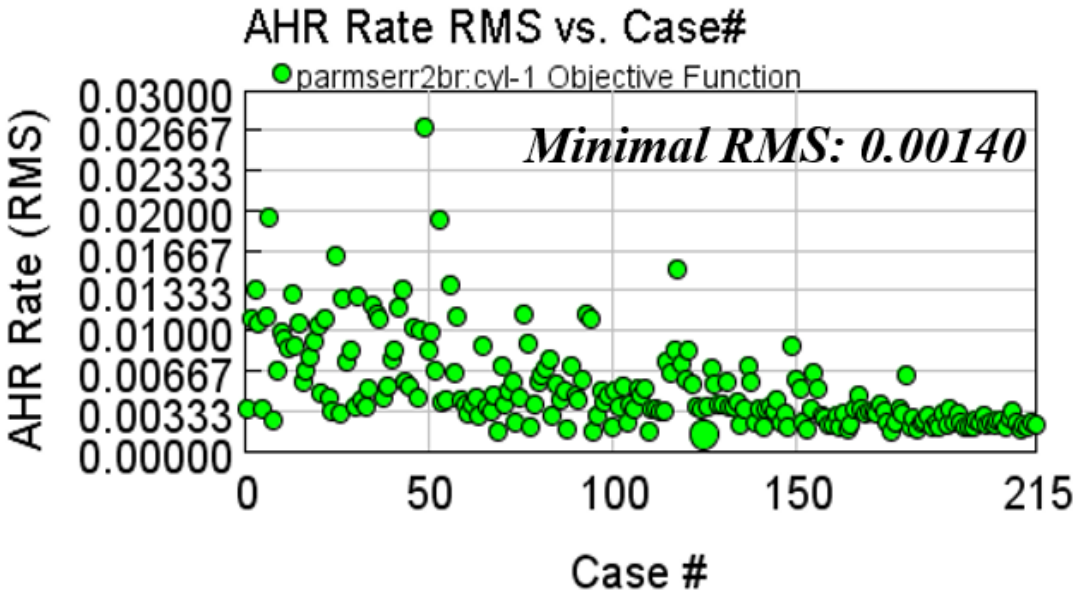

7.4: AHR Rate RMS vs. Case Number Mode B100

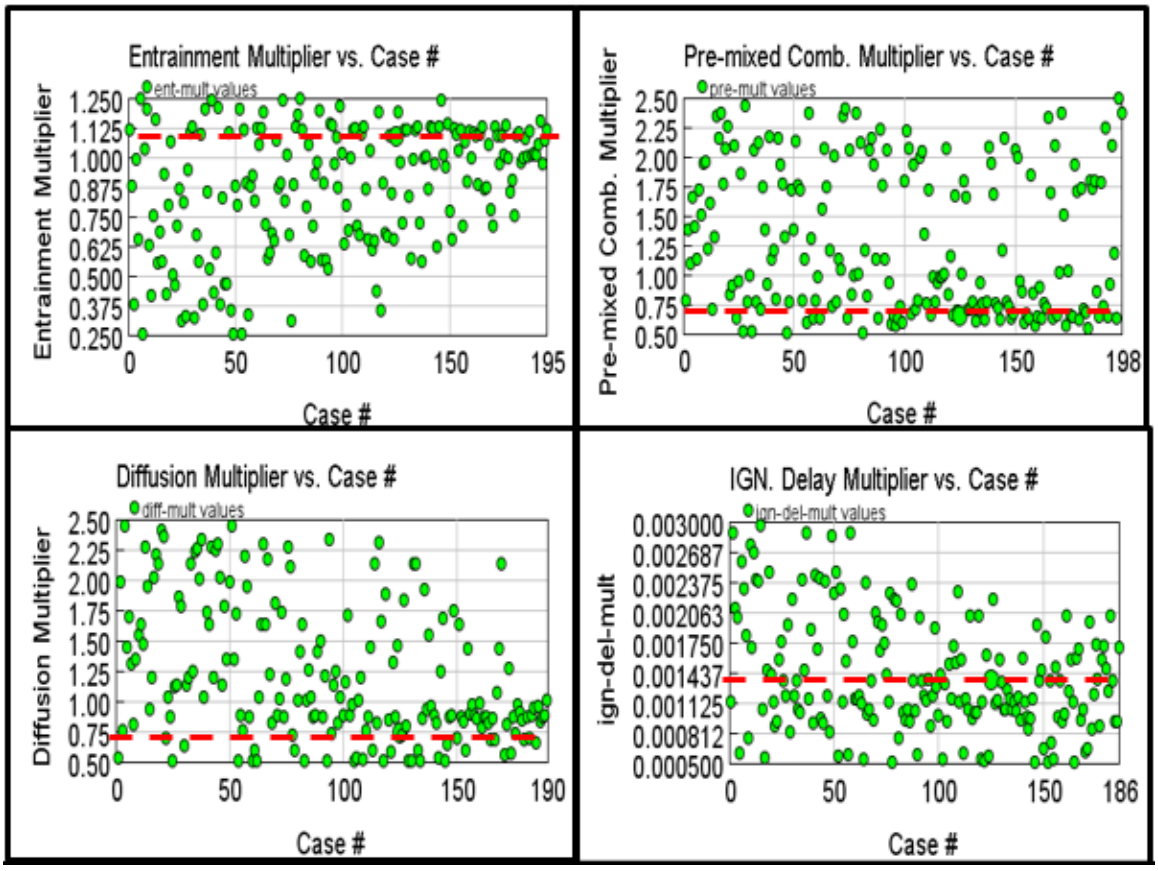

7.5: Individual Multiplier vs. Case Number Mode B100

A.4 DOE Sweep IAT vs. CR

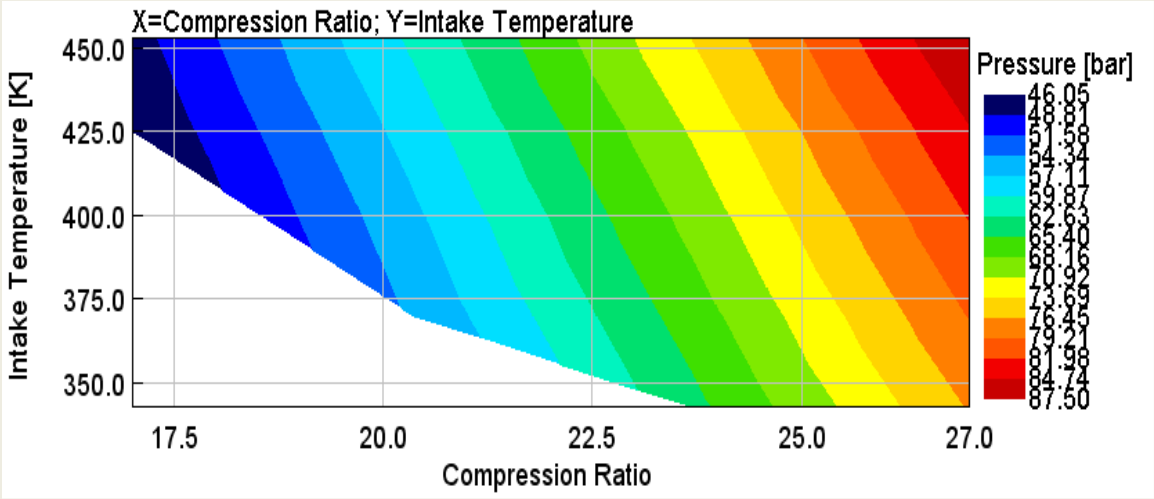

7.6: Peak Motoring Pressure IAT vs. CR Mode A25

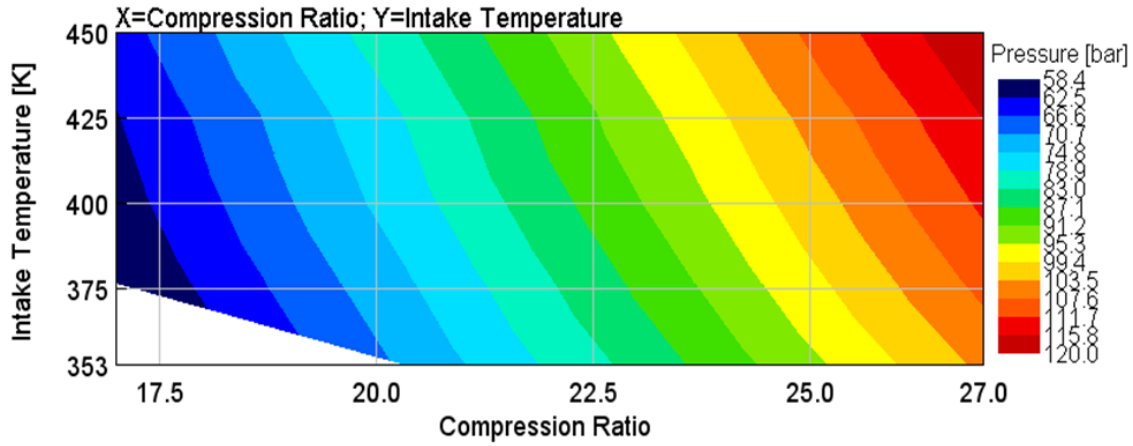

7.7 Peak Motoring Pressure IAT vs. CR Mode A50

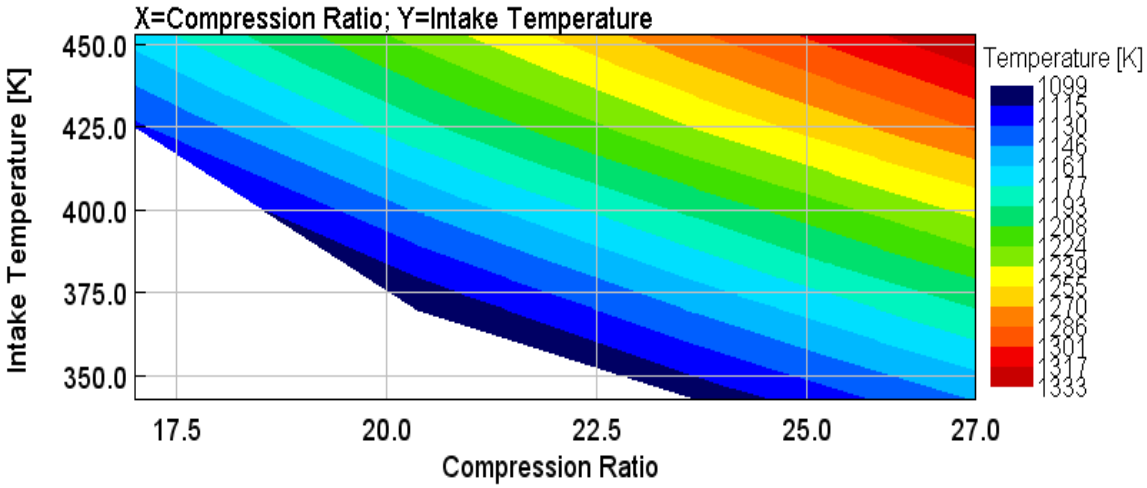

7.8: Peak Temperature Motoring CR vs. IAT Mode A25

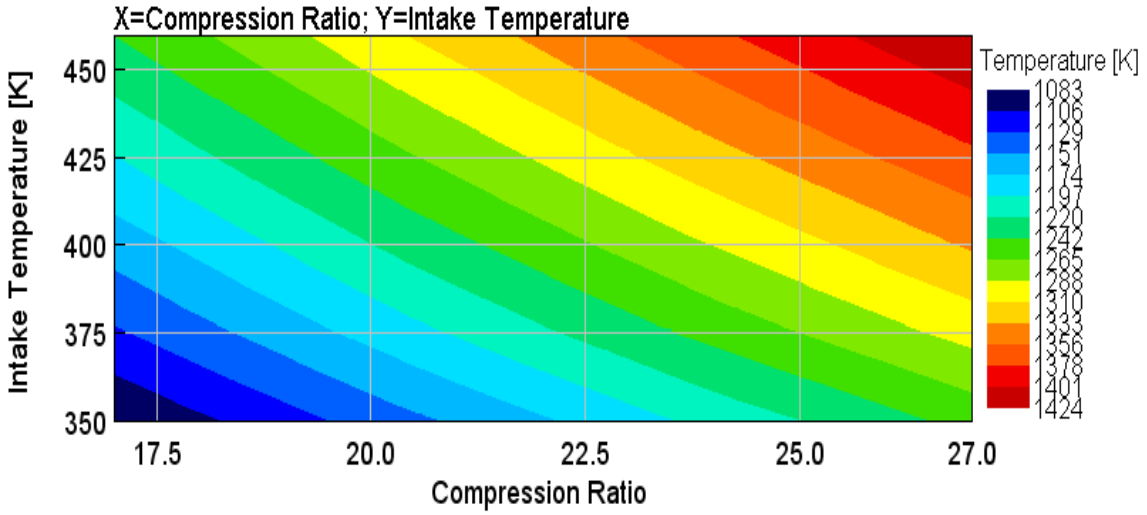

7.9: Peak Temperature Motoring CR vs. IAT Mode B100

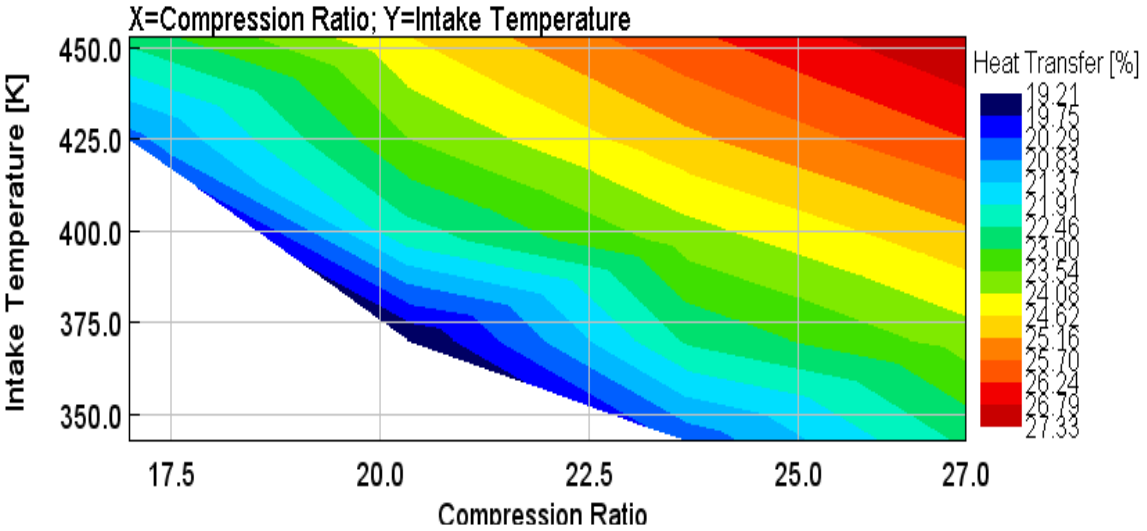

7.10: Heat Transfer Percent CR vs. IAT Mode A25

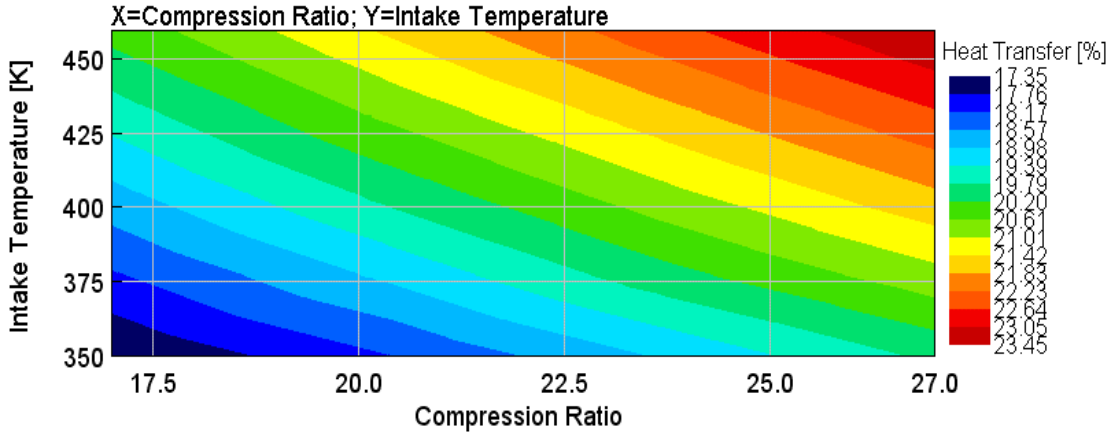

7.11: Case B100 Heat Transfer % vs. CR and IAT

A.5 Piston CAD Drawings

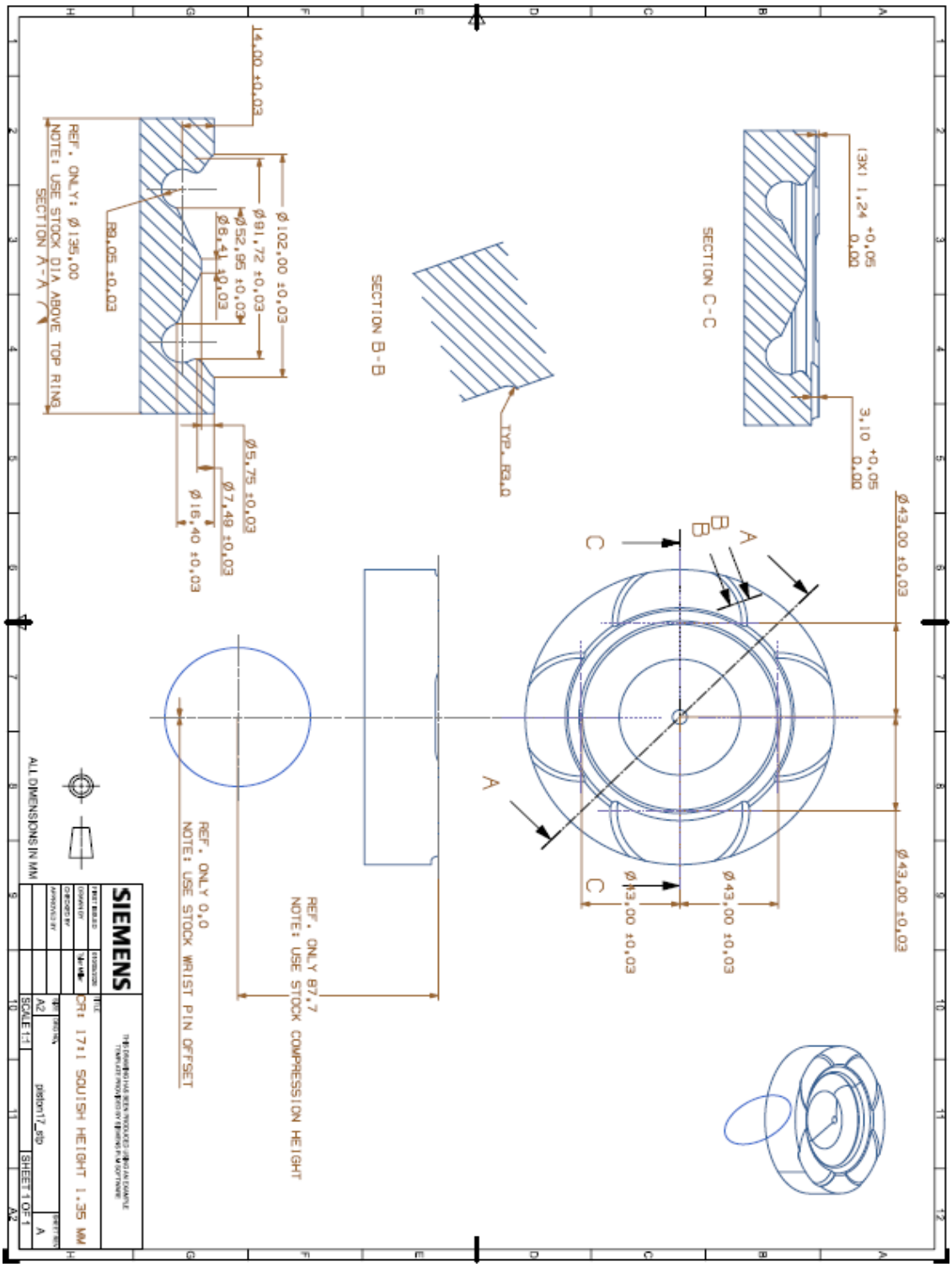

7.12: 17:1 CR Piston CAD Drawing

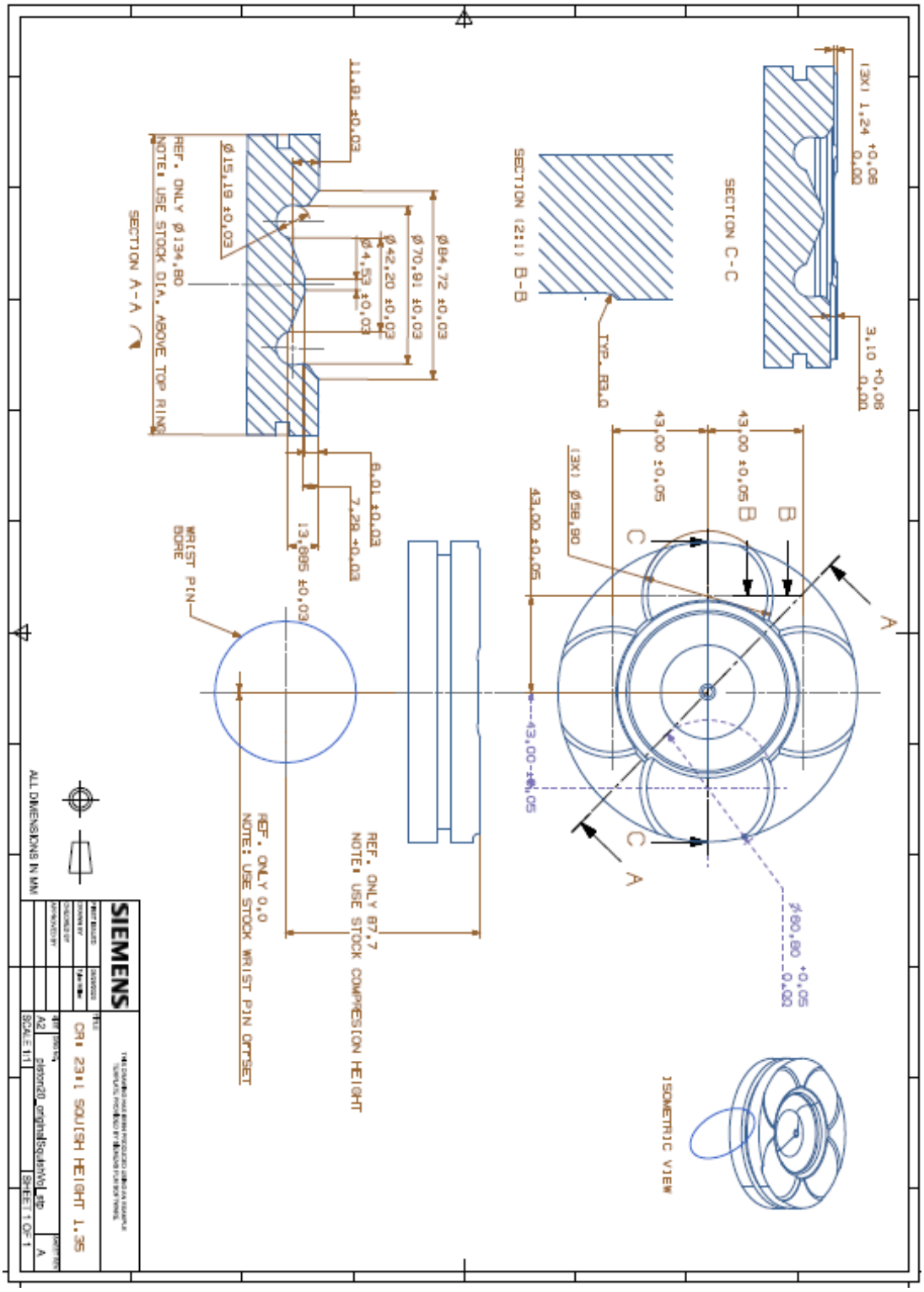

7.13: 23:1 Piston CAD Drawing

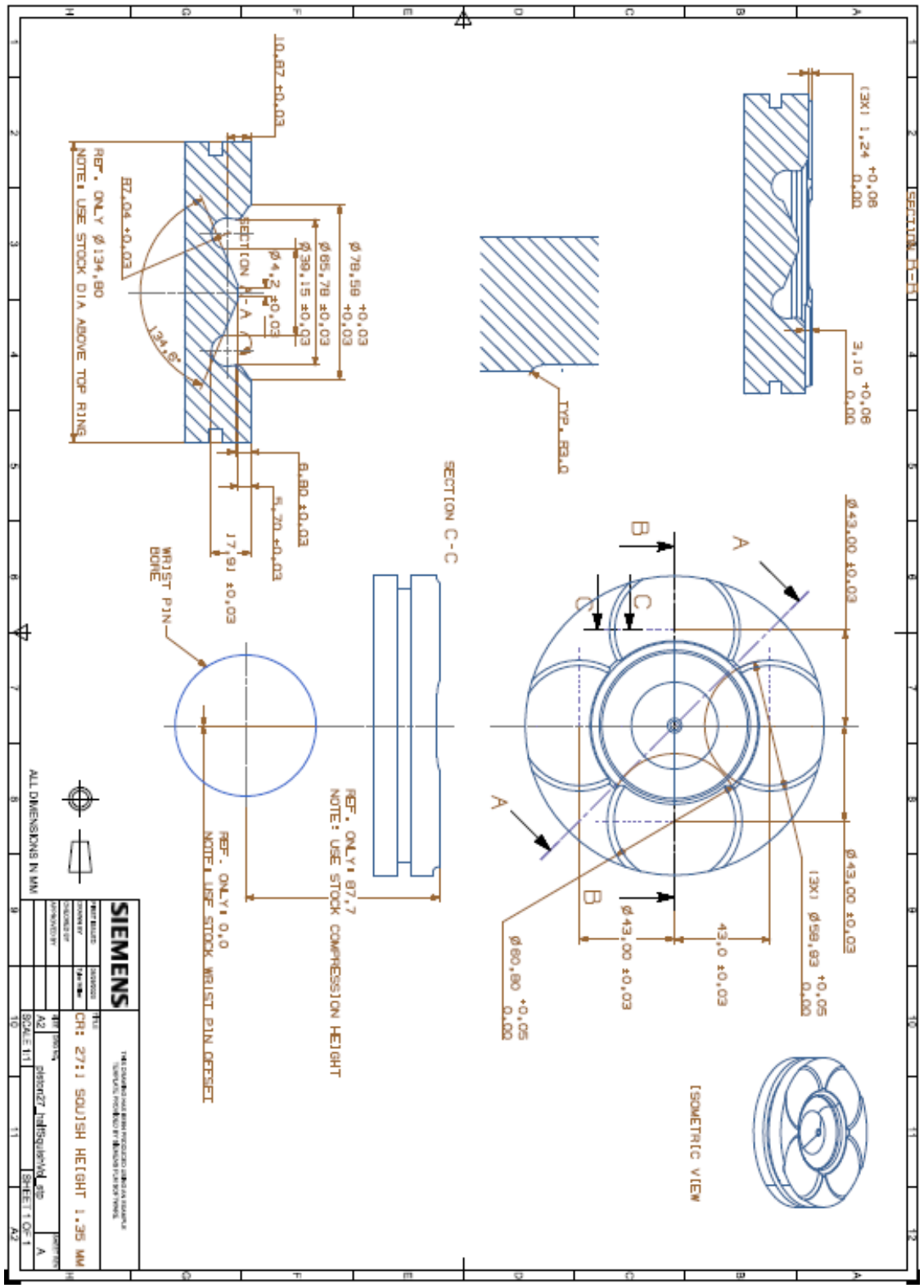

7.14: 27:1 Piston CAD Drawing

Copyright documentation

A.1 Documentation for Use of Figure 2.1: Cetane vs. Octane Correlation Obtained from Taylor

JOHN WILEY AND SONS LICENSE
TERMS AND CONDITIONS

Nov 30, 2020

This Agreement between Michigan Technological University -- Tyler Miller ("You") and John Wiley and Sons ("John Wiley and Sons") consists of your license details and the terms and conditions provided by John Wiley and Sons and Copyright Clearance Center.

License Number	4950791399021
License date	Nov 16, 2020
Licensed Content Publisher	John Wiley and Sons
Licensed Content Publication	Wiley Books
Licensed Content Title	Internal Combustion Engines: Applied Thermosciences, 3rd Edition
Licensed Content Author	Allan T. Kirkpatrick Colin R. Ferguson
Licensed Content Date	Jul 1, 2015
Licensed Content Pages	1
Type of use	Dissertation/Thesis

Requestor type	University/Academic
Format	Print and electronic
Portion	Figure/table
Number of figures/tables	1
Will you be translating?	No
Title	DESIGN, BUILD, AND ANALYSIS OF A COMPRESSED NATURAL GAS DIRECT INJECTION COMPRESSION IGNITION SINGLE CYLINDER RESEARCH ENGINE
Institution name	Michigan Technological University
Expected presentation date	Dec 2020
Portions	Figure 7.18 cetane and octane correlation for hydrocarbon fuels (adapted from Taylor 1985.)
Requestor Location	Michigan Technological University 1400 Townsend Dr. HOUGHTON, MI 49931 United States Attn: Michigan Technological University
Publisher Tax ID	EU826007151
Total	0.00 USD

Terms and Conditions

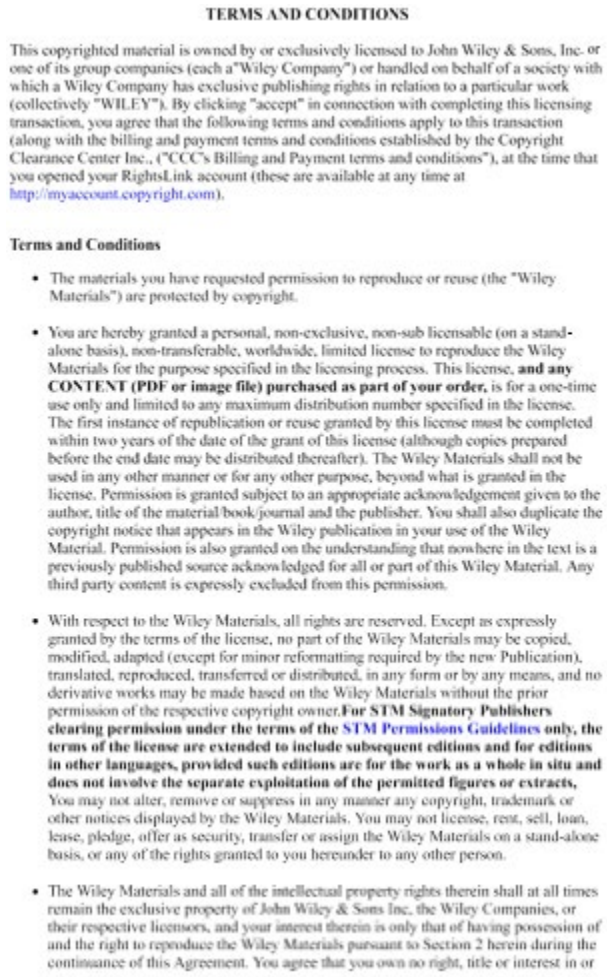

TERMS AND CONDITIONS

This copyrighted material is owned by or exclusively licensed to John Wiley & Sons, Inc. or one of its group companies (each a"Wiley Company") or handled on behalf of a society with which a Wiley Company has exclusive publishing rights in relation to a particular work (collectively "WILEY"). By clicking "accept" in connection with completing this licensing transaction, you agree that the following terms and conditions apply to this transaction (along with the billing and payment terms and conditions established by the Copyright Clearance Center Inc., ("CCC's Billing and Payment terms and conditions"), at the time that you opened your RightsLink account (these are available at any time at http://myaccount.copyright.com).

Terms and Conditions

- The materials you have requested permission to reproduce or reuse (the "Wiley Materials") are protected by copyright.
- You are hereby granted a personal, non-exclusive, non-sub licensable (on a stand-alone basis), non-transferable, worldwide, limited license to reproduce the Wiley Materials for the purpose specified in the licensing process. This license, **and any CONTENT (PDF or image file) purchased as part of your order,** is for a one-time use only and limited to any maximum distribution number specified in the license. The first instance of republication or reuse granted by this license must be completed within two years of the date of the grant of this license (although copies prepared before the end date may be distributed thereafter). The Wiley Materials shall not be used in any other manner or for any other purpose, beyond what is granted in the license. Permission is granted subject to an appropriate acknowledgement given to the author, title of the material/book/journal and the publisher. You shall also duplicate the copyright notice that appears in the Wiley publication in your use of the Wiley Material. Permission is also granted on the understanding that nowhere in the text is a previously published source acknowledged for all or part of this Wiley Material. Any third party content is expressly excluded from this permission.
- With respect to the Wiley Materials, all rights are reserved. Except as expressly granted by the terms of the license, no part of the Wiley Materials may be copied, modified, adapted (except for minor reformatting required by the new Publication), translated, reproduced, transferred or distributed, in any form or by any means, and no derivative works may be made based on the Wiley Materials without the prior permission of the respective copyright owner.**For STM Signatory Publishers clearing permission under the terms of the STM Permissions Guidelines only, the terms of the license are extended to include subsequent editions and for editions in other languages, provided such editions are for the work as a whole in situ and does not involve the separate exploitation of the permitted figures or extracts,** You may not alter, remove or suppress in any manner any copyright, trademark or other notices displayed by the Wiley Materials. You may not license, rent, sell, loan, lease, pledge, offer as security, transfer or assign the Wiley Materials on a stand-alone basis, or any of the rights granted to you hereunder to any other person.
- The Wiley Materials and all of the intellectual property rights therein shall at all times remain the exclusive property of John Wiley & Sons Inc, the Wiley Companies, or their respective licensors, and your interest therein is only that of having possession of and the right to reproduce the Wiley Materials pursuant to Section 2 herein during the continuance of this Agreement. You agree that you own no right, title or interest in or

A.2 Documentation for use of Westport CFD Thermal Analysis Simulation Data Results: Figure 4.26: Piston Surface Temperature Mapping) Figure 4.27: OEM Thermal Simulation Hot Spots, Figure 4.29: Pip temperature vs. Time Thermal Analysis, Figure 4.30: Baseline OEM vs. Fabricated Heat Loss, Figure 4.31: Peak Piston Temperature OEM vs. Fabricated, Figure 4.32: Peak Temperature Comparison for Fabricated Pistons vs OEM

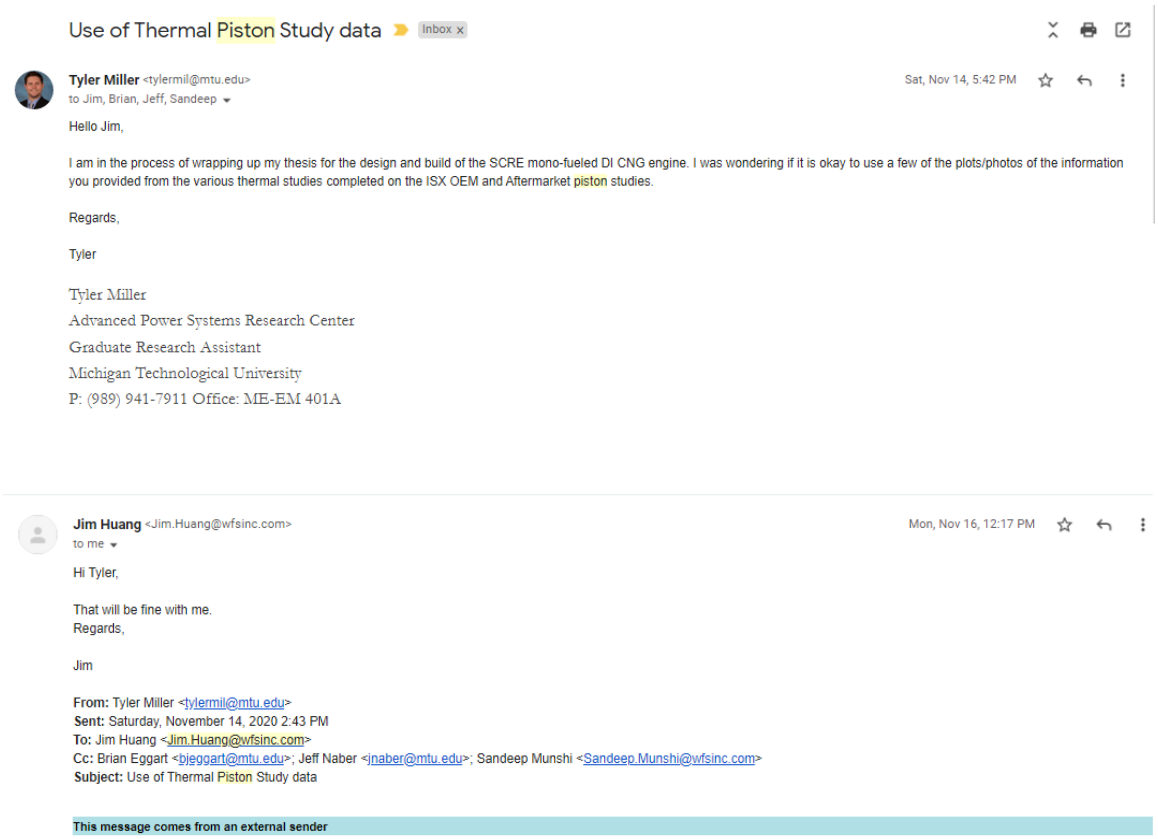

Use of Thermal Piston Study data Inbox ×

Tyler Miller <tylermil@mtu.edu> Sat, Nov 14, 5:42 PM
to Jim, Brian, Jeff, Sandeep

Hello Jim,

I am in the process of wrapping up my thesis for the design and build of the SCRE mono-fueled DI CNG engine. I was wondering if it is okay to use a few of the plots/photos of the information you provided from the various thermal studies completed on the ISX OEM and Aftermarket piston studies.

Regards,

Tyler

Tyler Miller
Advanced Power Systems Research Center
Graduate Research Assistant
Michigan Technological University
P: (989) 941-7911 Office: ME-EM 401A

Jim Huang <Jim.Huang@wfsinc.com> Mon, Nov 16, 12:17 PM
to me

Hi Tyler,

That will be fine with me.
Regards,

Jim

From: Tyler Miller <tylermil@mtu.edu>
Sent: Saturday, November 14, 2020 2:43 PM
To: Jim Huang <Jim.Huang@wfsinc.com>
Cc: Brian Eggart <bjeggart@mtu.edu>; Jeff Naber <jnaber@mtu.edu>; Sandeep Munshi <Sandeep.Munshi@wfsinc.com>
Subject: Use of Thermal Piston Study data

This message comes from an external sender

A.3 Copyright Information for use of Table 2.3: Efficiency and Power Comparison

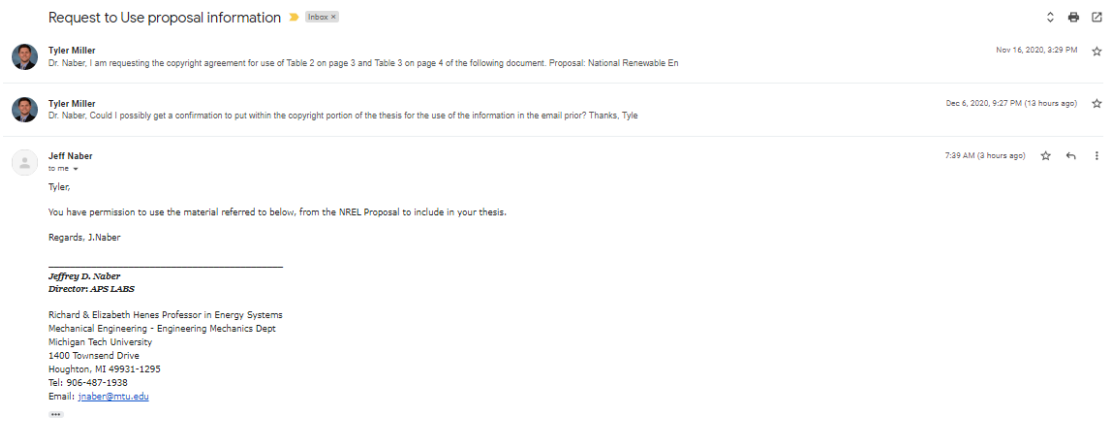

Request to Use proposal information Inbox ×

Tyler Miller Nov 16, 2020, 3:29 PM
Dr. Naber, I am requesting the copyright agreement for use of Table 2 on page 3 and Table 3 on page 4 of the following document. Proposal: National Renewable En

Tyler Miller Dec 6, 2020, 9:27 PM (13 hours ago)
Dr. Naber, Could I possibly get a confirmation to put within the copyright portion of the thesis for the use of the information in the email prior? Thanks, Tyle

Jeff Naber 7:39 AM (3 hours ago)
to me

Tyler,

You have permission to use the material referred to below, from the NREL Proposal to include in your thesis.

Regards, J.Naber

Jeffrey D. Naber
Director: APS LABS

Richard & Elizabeth Henes Professor in Energy Systems
Mechanical Engineering - Engineering Mechanics Dept
Michigan Tech University
1400 Townsend Drive
Houghton, MI 49931-1295
Tel: 906-487-1938
Email: jnaber@mtu.edu